

# Coated magnetic carrier particles for targeted drug delivery

Sibnath Kayal

2011

Sibnath Kayal. (2011). Coated magnetic carrier particles for targeted drug delivery. Doctoral thesis, Nanyang Technological University, Singapore.

<https://hdl.handle.net/10356/45161>

<https://doi.org/10.32657/10356/45161>



**NANYANG  
TECHNOLOGICAL  
UNIVERSITY**

COATED MAGNETIC CARRIER PARTICLES FOR  
TARGETED DRUG DELIVERY

**COATED MAGNETIC CARRIER PARTICLES FOR  
TARGETED DRUG DELIVERY**

SIBNATH KAYAL

**SIBNATH KAYAL**

**SCHOOL OF MATERIALS SCIENCE AND ENGINEERING**

**2011**

2011

---

# **COATED MAGNETIC CARRIER PARTICLES FOR TARGETED DRUG DELIVERY**

**SIBNATH KAYAL**

School of Materials Science and Engineering

A thesis submitted to the Nanyang Technological University  
in partial fulfillment of the requirement for the degree of  
Doctor of Philosophy

**2011**

---

## Acknowledgements

I express my sincere gratitude to my supervisor Prof. R. V. Ramanujan for his constant guidance throughout my PhD duration. He has enlightened me throughout the work by his rich experience in the area of Materials Science.

I am thankful to Prof. D. Bandyapadhaya, IIT, Guwahati, India who helped me in all possible ways during the modelling work. I had many interactive sessions with him, which was extremely useful in giving direction to my research work.

I am thankful to my group members, Sreekanth, Derrik, Vinh, Pratap, Shashwat and Jiayan for their prompt help.

I am thankful to Patrick Lai and Yeow Swee Kuan from Electromagnetic Materials Lab for their kind help during the experiments.

I am thankful to the technical staff of Electron Microscopy & X-Ray Diffraction Lab, Polymer Lab, Biomaterials Lab and Computer Facilities Lab for their help in equipment operation.

I am thankful to my family and friends for their support, encouragement and inspiration not only in my research, but in all aspects of my life.

---

## Abstract

Magnetic drug targeting, using coated magnetic carrier particles (MCP), is an efficient method to localize drugs at the tumor site. In magnetically targeted drug delivery, MCP loaded with anti-cancer drugs are injected into the patient and an external magnetic field is used to concentrate MCP at the tumor site. Advantages include reduction in the drug dose and minimization of systemic side effects. The objective of this work is the synthesis, characterization and property evaluation of coated MCP, and experimental and modelling studies of the efficacy with which such particles can be captured by an external magnetic field.

Gold coated iron (Fe@Au) and polyvinylalcohol coated iron oxide (PVA-IO) nanoparticles were synthesized and characterized by XRD, TEM, DLS, TGA, XPS, FTIR and VSM techniques. The particles were superparamagnetic, with saturation magnetization decreasing with increasing coating thickness. Fe@Au nanoparticles was found to bind with doxorubicin (DOX) drug by the interaction of the amine ( $-\text{NH}_2$ ) group of DOX with the gold (Au) shell, whereas the binding of DOX with PVA-IO occurred through hydrogen bonding by the interaction of the  $-\text{NH}_2$  and  $-\text{OH}$  groups of DOX with the  $-\text{OH}$  group of PVA. Up to 25% and 45% of adsorbed drug was released from Fe@Au and PVA-IO MCP, respectively. Up to 90% of PVA-IO and 86% of Fe@Au MCP were retained at a field gradient of  $25 \text{ T m}^{-1}$  and flow rate of  $1 \text{ mm s}^{-1}$ .

The transport and capture of MCP in the tumor vasculature by an external permanent magnet was modelled. The trajectories of various MCP showed that it is easier to capture larger MCP with superior magnetic properties. It was found that  $\text{Fe}_3\text{O}_4$ , Fe@Au, PVA-IO MCP (100 nm) can be targeted to breast tumors and other skin tumors located in the hand,

---

leg and neck by a typical permanent magnet. In order to target tumors situated deep inside the body, MCP with higher saturation magnetization, such as Fe and FeCo, or an external magnet with higher magnetic field gradient ( $100 \text{ T m}^{-1}$ ) must be chosen.

Trapping of MCP using nonlinear computational fluid dynamics (CFD) simulations showed that when a suspension of MCP (ferrofluid) is injected and subjected to an external magnetic field, ferrofluid creeps along the wall of the blood vessel. Therefore, drug injection should be as close as possible to the tumor to minimize the drug friction with the wall. The time of exposure to the magnetic field can be optimized and deposition of MCP can be maximized by suitable magnetic field, minimizing loss of MCP due to convection and diffusion. *Thus, Fe@Au and PVA-IO MCP exhibit high capture efficiency in magnetic drug targeting, the capture efficiency depends on the magnetic properties and size of MCP, blood flow rate, time of capture, convection and diffusion effects can significantly influence the capture efficiency of MCP.*

---

# Table of Contents

<b>ACKNOWLEDGEMENTS.....</b>	<b>i</b>
<b>ABSTRACT .....</b>	<b>ii</b>
<b>TABLE OF CONTENTS .....</b>	<b>iv</b>
<b>LIST OF FIGURES.....</b>	<b>ix</b>
<b>LIST OF TABLES.....</b>	<b>xvi</b>
<b>LIST OF ABBREVIATIONS.....</b>	<b>xvii</b>
<b>LIST OF SYMBOLS .....</b>	<b>xviii</b>
<b>CHAPTER 1 .....</b>	<b>1</b>
<b>INTRODUCTION .....</b>	<b>1</b>
<b>1.1 BIOMEDICAL APPLICATIONS OF MAGNETIC NANOPARTICLES .....</b>	<b>3</b>
<b>1.1.1 Therapeutic applications.....</b>	<b>3</b>
<b>1.1.2 Diagnostic applications.....</b>	<b>4</b>
<b>1.2 THE NEED FOR DRUG TARGETING: MOTIVATION.....</b>	<b>6</b>
<b>1.3 MAGNETIC DRUG TARGETING: THE SOLUTION.....</b>	<b>7</b>
<b>1.4 OBJECTIVE AND SCOPE OF THE WORK.....</b>	<b>8</b>
<b>1.5 NOVELTY OF WORK .....</b>	<b>12</b>

---

<b>1.6</b>	<b>METHODOLOGY .....</b>	<b>14</b>
<b>1.7</b>	<b>ORGANIZATION OF THE THESIS.....</b>	<b>15</b>
<b>CHAPTER 2 .....</b>		<b>16</b>
<b>LITERATURE REVIEW .....</b>		<b>16</b>
<b>2.1</b>	<b>CLASSES OF MAGNETIC MATERIALS.....</b>	<b>16</b>
<b>2.1.1</b>	<b>M–H curves.....</b>	<b>17</b>
<b>2.1.2</b>	<b>Action of forces on magnetic nanoparticles.....</b>	<b>21</b>
<b>2.2.</b>	<b>MAGNETICALLY TARGETED DRUG DELIVERY .....</b>	<b>22</b>
<b>2.2.1.</b>	<b>Prior efforts towards magnetically targeted drug delivery.....</b>	<b>23</b>
<b>2.2.2</b>	<b>Magnetic nanoparticles : property requirements.....</b>	<b>25</b>
<b>2.2.3</b>	<b>Magnetic core materials .....</b>	<b>26</b>
<b>2.2.4</b>	<b>Coating materials .....</b>	<b>26</b>
<b>2.3</b>	<b>SYNTHESIS OF MAGNETIC NANOPARTICLES .....</b>	<b>35</b>
<b>2.3.1</b>	<b>Precipitation from solution .....</b>	<b>35</b>
<b>2.3.2</b>	<b>Chemical vapour condensation (CVC) .....</b>	<b>40</b>
<b>2.4</b>	<b>MAGNETIC COMPOSITES.....</b>	<b>40</b>
<b>2.4.1</b>	<b>Magnetic nanoparticles encapsulated in polymer matrices .....</b>	<b>41</b>

---

---

2.4.2	Magnetic nanoparticles encapsulated in inorganic matrices .....	42
2.5	INNOVATIVE ASPECTS OF THE CURRENT WORK .....	42
CHAPTER 3 .....		45
EXPERIMENTAL PROCEDURES AND MODEL DEVELOPMENT .....		45
3.1	SYNTHESIS OF GOLD COATED IRON (Fe@Au) MCP .....	45
3.2	SYNTHESIS OF PVA COATED IRON OXIDE (PVA-IO) MCP .....	47
3.3	CHARACTERIZATION AND <i>IN-VITRO</i> TESTS .....	49
3.3.1	Transmission electron microscopy .....	49
3.3.2	X-ray diffraction .....	49
3.3.3	Magnetic measurements .....	50
3.3.4	Dynamic light scattering .....	50
3.3.5	X-ray photoelectron spectroscopy .....	50
3.3.6	Thermo gravimetric analysis .....	50
3.3.7	Fourier transform infrared spectra .....	51
3.3.8	Doxorubicin (DOX) drug loading and release .....	51
3.3.9	In-vitro targeting of MCP .....	52
3.4	MODEL DEVELOPMENT .....	53

---

---

<b>3.4.1 Magnetic field.....</b>	<b>55</b>
<b>3.4.2 Flow velocity.....</b>	<b>56</b>
<b>3.4.3 Equation of motion .....</b>	<b>57</b>
<b>3.5 CFD SIMULATIONS .....</b>	<b>60</b>
<b>3.5.1 Boundary conditions.....</b>	<b>61</b>
<b>3.5.2 Magnetic force field .....</b>	<b>62</b>
<b>3.5.3 Grid generation and solution methodology.....</b>	<b>62</b>
<b>CHAPTER 4 .....</b>	<b>64</b>
<b>RESULTS AND DISCUSSION.....</b>	<b>64</b>
<b>4.1 GOLD COATED IRON (Fe@Au) MCP SYSTEM.....</b>	<b>64</b>
<b>4.1.1 Physical properties.....</b>	<b>64</b>
<b>4.2 PVA COATED IRON OXIDE (PVA-IO) MCP SYSTEM.....</b>	<b>78</b>
<b>4.2.1 Physical properties.....</b>	<b>78</b>
<b>4.2.2 PVA adsorption onto iron oxide nanoparticles .....</b>	<b>83</b>
<b>4.2.3 Magnetic properties .....</b>	<b>88</b>
<b>4.3 DOXORUBICIN (DOX) DRUG LOADING AND RELEASE.....</b>	<b>90</b>
<b>4.3.1 Gold coated iron (Fe@Au) MCP system.....</b>	<b>91</b>

---

---

<b>4.3.2 PVA-IO MCP system.....</b>	<b>95</b>
<b>4.4 <i>IN-VITRO</i> EXPERIMENTAL TARGETING OF MCP .....</b>	<b>101</b>
<b>4.5 MODELLING OF TARGETING MCP.....</b>	<b>106</b>
<b>4.5.1 Model Parameters.....</b>	<b>107</b>
<b>4.5.2 Magnetic Field Components.....</b>	<b>108</b>
<b>4.5.3 MCP trajectories.....</b>	<b>110</b>
<b>4.5.4 Distance of Capture (d).....</b>	<b>112</b>
<b>4.5.5 Numerical Simulations.....</b>	<b>115</b>
<b>CHAPTER 5 .....</b>	<b>127</b>
<b>CONCLUSIONS AND FUTURE WORK .....</b>	<b>127</b>
<b>REFERENCES .....</b>	<b>133</b>
<b>APPENDIX-A .....</b>	<b>175</b>
<b>PUBLICATIONS AND CONFERENCES .....</b>	<b>177</b>

---

## List of Figures

<b>Figure 1.1</b> Global incidence and mortality rates for cancer .....	1
<b>Figure 1.2</b> Schematic representation of magnetic drug targeting to a specific region .....	8
<b>Figure 1.3</b> Overview of the thesis.....	9
<b>Figure 1.4</b> chemical structure of DOX.....	11
<b>Figure 2.1.</b> Magnetic responses associated with different classes of magnetic material..	17
<b>Figure 2.2</b> Particles stabilized by (a) the electrostatic layer, (b) steric repulsion .....	27
<b>Figure 2.3</b> Mechanism of formation of uniform particles in solution: curve I: single nucleation and uniform growth by diffusion (classical model of LaMer and Dinegar); curve II: nucleation, growth and aggregation of smaller subunits; curve III: multiple nucleation events and Ostwald ripening growth .....	36
<b>Figure 3.1</b> Schematic diagram showing a typical procedure for formation of Fe@Au MCP by the reverse micelle technique. FeSO <sub>4</sub> and HAuCl <sub>4</sub> are reduced by NaBH <sub>4</sub> , CTAB is surfactant, 1-butanol is co-surfactant and octane is oil phase. ....	46
<b>Figure 3.2</b> Schematic of an <i>in-vitro</i> experiment simulating the human circulatory system; A: intake beaker, B: vibrating plate, C: peristaltic pump, D: syringe, E: silicone tube, F: permanent magnet, H: outlet beaker, G: region of targeting. ....	52
<b>Figure 3.3</b> The 2-D rectangular channel mimicking a cylindrical tube and frame of reference for analysis.....	53

<b>Figure 4.1</b> X-ray diffraction pattern of (a) S-1 (uncoated), (b) S-2 (0.102 mmol gold coated iron nanoparticles) and (c) S-3 (0.204 mmol gold coated iron nanoparticles). The uncoated particles are oxidized to iron oxide whereas in gold coated particles, iron peaks overlap with gold peaks. ....	65
<b>Figure 4.2</b> Selected area electron diffraction (SAED) pattern of S-3 (0.204 mmol gold coated iron nanoparticles). Gold 200, 220, 222 diffraction peaks overlap with iron 110, 200, 211 peaks.....	66
<b>Figure 4.3</b> EDX spectrum of S-3 (0.204 mmol gold coated iron nanoparticles). The absence of oxygen peak indicates that iron is not oxidized when coated with gold. The peaks of carbon and copper arise from the sample holder.....	67
<b>Figure 4.4</b> XPS spectra and peak fit of the (a) Fe 2p and (b) Au 4f regions of (i) S-2 (0.102 mmol gold coated iron nanoparticles) and (ii) S-3 (0.204 mmol gold coated iron nanoparticles). The detection of Fe with the Au coating in XPS spectra suggests that Au coating is thin .....	68
<b>Figure 4.5</b> TEM micrographs of (a) S-1 (uncoated) and (b) S-3 (0.204 mmol gold coated iron nanoparticles). The corresponding size distribution of (c) S-1 (uncoated) and (d) S-3 (0.204 mmol gold coated iron nanoparticles). ....	69
<b>Figure 4.6</b> Average hydrodynamic diameter of S-1 (uncoated), S-2 (0.102 mmol gold coated iron nanoparticles) and S-3 (0.204 mmol gold coated iron nanoparticles) in PBS. Uncoated iron nanoparticles flocculate within 1 h, whereas Fe@Au nanoparticles are relatively stable up to 4 h. ....	70

<b>Figure 4.7</b> VSM plots of magnetization vs field of (a) S-1 (uncoated), (b) S-2 (0.102 mmol gold coated iron nanoparticles) and (c) S-3 (0.204 mmol gold coated iron nanoparticles). Particles are superparamagnetic, $M_s$ decreases with an increase in gold concentration. ....	71
<b>Figure 4.8</b> X-ray diffraction pattern of (a) S-8 (5 wt% PVA coated iron oxide), (b) S-6 (1 wt% PVA coated iron oxide) and (c) S-4 (Uncoated iron oxide). The phase is magnetite ( $Fe_3O_4$ ), peaks corresponding to reflection planes are indexed. ....	78
<b>Figure 4.9</b> Rietveld refinement of X-ray diffraction pattern of (a) S-4 (uncoated iron oxide) and (b) S-8 (5 wt% PVA coated iron oxide). Peak broadening occurs in PVA coated iron oxide nanoparticles due to decrease in crystallinity. ....	79
<b>Figure 4.10</b> TEM micrographs of (a) S-4, corresponding to the uncoated iron oxide nanoparticles and (b) S-8, coated with 5 wt% PVA. The corresponding size distribution of (c) S-4 (uncoated iron oxide) and (d) S-8 (5 wt% PVA coated iron oxide). ....	80
<b>Figure 4.11</b> Average hydrodynamic diameter of S-4 (uncoated iron oxide nanoparticles), S-6 (iron oxide nanoparticles coated with 1 wt% PVA) and S-8 (iron oxide nanoparticles coated with 5 wt% PVA) in PBS. ....	81
<b>Figure 4.12</b> Weight loss vs. temperature TGA curves of (a) S-4 (uncoated iron oxide), (b) S-5 (iron oxide coated with 0.5 wt% PVA), (c) S-6 (iron oxide coated with 1 wt% PVA), (d) S-7 (iron oxide coated with 2 wt% PVA) and (e) S-8 (iron oxide coated with 5 wt% PVA) heated up to 600°C in air. The inset shows the TGA curve of pure PVA indicating complete degradation of PVA when heated up to 600°C. ....	83

<b>Figure 4.13</b> FTIR spectra of (a) uncoated iron oxide and (b) PVA-IO nanoparticles. Bands at 2912, 1416, 1092 and 850 $\text{cm}^{-1}$ in PVA-IO confirm the attachment of PVA to iron oxide nanoparticles.....	85
<b>Figure 4.14</b> Magnetization vs. field curves measured at room temperature of (a) S-4, corresponding to uncoated iron oxide nanoparticles, (b) S-5, iron oxide coated with 0.5 wt% PVA, (c) S-6, iron oxide coated with 1 wt% PVA, (d) S-7, iron oxide coated with 2 wt% PVA and (e) S-8, iron oxide coated with 5 wt% PVA. Particles are superparamagnetic, $M_s$ decreases with increase in PVA concentration. ....	88
<b>Figure 4.15</b> The color of (a) pure DOX solution, (b) DOX solution after 26 h mixing with uncoated iron nanoparticles and (c) DOX solution after 26 h mixing with gold coated iron (Fe@Au) nanoparticles. The change in color of DOX indicates that the DOX is attached onto Fe@Au nanoparticles only.....	91
<b>Figure 4.16</b> DOX (a) loading and (b) release profile of gold coated iron (Fe@Au) MCP. ....	92
<b>Figure 4.17</b> FTIR spectra of (a) Fe@Au, (b) pure DOX and (c) DOX-attached Fe@Au nanoparticles. Amine ( $-\text{NH}_2$ ) group of DOX is involved in attachment to the Fe@Au nanoparticles. ....	93
<b>Figure 4.18</b> UV-vis spectra of (a) pure DOX, (b) DOX-attached Fe@Au and (c) Fe@Au colloid. Peak is broadened and red shifted at 535 nm upon addition of colloidal Fe@Au to DOX.....	94
<b>Figure 4.19</b> DOX loading on to PVA-IO nanoparticles, DOX loading increases with increase in PVA concentration.....	96

<b>Figure 4.20</b> DOX release from PVA-IO, DOX release follows the Fickian diffusion controlled process.....	97
<b>Figure 4.21</b> FTIR spectra of (a) pure DOX and (b) DOX-conjugated PVA-IO. Conjugation of DOX to the PVA-IO occurs via the interaction of $-\text{NH}_2$ and $-\text{OH}$ groups of DOX with $-\text{OH}$ groups of PVA.....	98
<b>Figure 4.22</b> Percent retention of (a) S-2 (0.102 mmol gold coated iron nanoparticles) and (b) S-3 (0.204 mmol gold coated iron nanoparticles) at various flow rates of fluid.....	101
<b>Figure 4.23</b> Percent retention of (a) S-4 (uncoated $\text{Fe}_3\text{O}_4$ ), (b) S-6 ( $\text{Fe}_3\text{O}_4$ coated with 1 wt% PVA), (c) S-7 ( $\text{Fe}_3\text{O}_4$ coated with 2 wt% PVA) and (d) S-8 ( $\text{Fe}_3\text{O}_4$ coated with 5 wt% PVA) at various flow rates of fluid. ....	103
<b>Figure 4.24</b> $\nabla H^2$ components of (a) Nd-Fe-B rectangular permanent magnet and (b) Nd-Fe-B cylindrical permanent magnet along the axis of vessel, when the vessel is at a distance of 5, 10 and 15 mm from the surface of magnet.....	108
<b>Figure 4.25</b> Trajectories of $\text{Fe}_3\text{O}_4$ MCP (particle size 100, 200 and 500 nm) in the vessel when $(\bar{v}) = 5 \text{ mm s}^{-1}$ , $d = 30 \text{ mm}$ . ....	110
<b>Figure 4.26</b> Trajectories of different MNCP of radius of 100 nm in the vessel when $(\bar{v}) = 5 \text{ mm s}^{-1}$ , $d = 30 \text{ mm}$ .....	111
<b>Figure 4.27</b> Representative plots of distance of capture vs MCP size for different flow rates of fluid. ....	112
<b>Figure 4.28</b> Distance of capture for various MCP with size of 100 nm and $\bar{v} = 5 \text{ mm.s}^{-1}$ using a typical permanent magnet. ....	113

---

**Figure 4.29** Distance of capture for various MCP with size of 100 nm and  $\bar{v} = 5 \text{ mm.s}^{-1}$  using a higher magnetic field gradient ( $100 \text{ T m}^{-1}$ )..... 114

**Figure 4.30** Temporal evolution of the concentration profile when a ferrofluid ( $R_p = 100 \text{ nm}$  and  $\chi = 0.4$ ) is continuously injected at the inlet of a 2-D channel. Initially the vessel is assumed to be filled with a PBS buffer flowing at  $10 \text{ mm.s}^{-1}$ . The centre of the magnet is placed at the mid point of the lateral coordinate. The vertical distance,  $d$  from the bottom wall of the vessel to surface of the magnet is 10 mm. .... 116

**Figure 4.31** Temporal evolution of the concentration profile when a ferrofluid ( $R_p=100 \text{ nm}$  and  $\chi = 0.4$ ) is continuously injected at the inlet of a 2-D channel. In this simulation  $d$  is kept constant at 10 mm. The contour plots represent: (a)  $\bar{v} = 1 \text{ mm.s}^{-1}$ , (b)  $\bar{v} = 5 \text{ mm.s}^{-1}$ , and (c)  $\bar{v} = 40 \text{ mm.s}^{-1}$ ..... 118

**Figure 4.32** Temporal evolution of the concentration profile when a ferrofluid ( $\bar{v} = 10 \text{ mm s}^{-1}$ ) is continuously injected at the inlet of a 2-D channel. In this contour plots: (a)  $d = 5 \text{ mm}$ ,  $R_p = 100 \text{ nm}$  and  $\chi = 0.4$ ; (b)  $d = 15 \text{ mm}$ ,  $R_p = 100 \text{ nm}$  and  $\chi = 0.4$ ; (c)  $d = 10 \text{ mm}$ ,  $R_p = 200 \text{ nm}$  and  $\chi = 0.4$ ..... 120

**Figure 4.33** (a) Temporal evolution of the concentration profile when a ferrofluid ( $R_p=100 \text{ nm}$  and  $\chi = 0.4$ ) is continuously injected at the inlet of a 2-D channel at flow rate ( $\bar{v}$ ) of  $10 \text{ mm.s}^{-1}$  under weak magnetic field ( $d = 50 \text{ mm}$ ). (b)The streamline contour plot of frame (i) in magnified view shows the trade off between the magnetic force and the convective force leading to the formation of vortices near the wall..... 121

**Figure 4.34** Temporal evolution of the concentration profile of a ferrofluid ( $R_p = 100 \text{ nm}$  and  $\chi = 0.4$ ) in a 2-D channel under the influence of a cylindrical magnet ( $d = 10 \text{ mm}$ ).

---

The contour plots represent: (a)  $\bar{v} = 1 \text{ mm.s}^{-1}$ , (b)  $\bar{v} = 10 \text{ mm.s}^{-1}$ , and (c)  $\bar{v} = 40 \text{ mm.s}^{-1}$ .

..... 123

---

## List of Tables

<b>Table 2.1</b> Some useful polymers to coat nanoparticles for biomedical applications.....	32
<b>Table 3.1</b> Summary of sample sets synthesized by the reverse micelle technique. ....	47
<b>Table 3.2</b> Summary of sample sets synthesized by the co-precipitation technique. ....	48
<b>Table 4.1</b> Saturation magnetization ( $M_s$ ) of Fe@Au. ....	72
<b>Table 4.2</b> Comparison of gold coated magnetic nanoparticles of current work with selected literature.....	77
<b>Table 4.3</b> Weight loss due to PVA in thermogravimetric analysis (TGA) in air. ....	84
<b>Table 4.4</b> Assignment of FTIR spectra of uncoated iron oxide, PVA-IO. ....	87
<b>Table 4.5</b> Saturation magnetization ( $M_s$ ) of uncoated and PVA-IO nanoparticles. ....	89
<b>Table 4.6</b> Parameters used in modelling and simulations. ....	107

---

## List of Abbreviations

CFD	Computational fluid dynamics
DLS	Dynamic light scattering
DOX	Doxorubicin
Fe@Au	Gold coated iron
FTIR	Fourier transform infrared
HCC	Hepato cellular carcinoma
MCP	Magnetic carrier particles comprising of small aggregates of nanoparticles
MDT	Magnetic drug targeting
MNP	Magnetic nanoparticles
MRI	Magnetic resonance imaging
PVA	Polyvinylalcohol
PVA-IO	Polyvinylalcohol coated iron oxide
TEM	Transmission electron microscopy
TGA	Thermo-gravimetric analysis
VSM	Vibrating sample magnetometry
XPS	X-ray photoelectron spectroscopy
XRD	X-ray diffraction

---

## List of Symbols

$\mu_0$	Magnetic permeability of free space
$\chi$	Magnetic susceptibility
$H$	Magnetic field strength
$B$	Magnetic field gradient
$R_p$	Hydrodynamic radius of particle
$V$	Volume of particle
$\eta$	Viscosity of fluid
$\rho$	Density of fluid
$\mathbf{v}_p$	Particle velocity
$\bar{v}$	Average velocity of fluid
$D$	Mass diffusivity
$h$	Half-height of rectangular magnet
$w$	Half-width of rectangular magnet
$R_{mag}$	Radius of cylindrical magnet
$d$	Distance between magnet and blood vessel
$R$	Radius of blood vessel

# Chapter 1

## Introduction

Cancer treatment is a key challenge in biomedicine with more than 10 million new cases every year [1]. Global cancer rates are expected to double by the year 2020, according to a report from the International Agency for Research on Cancer (IARC), a branch of the World Health Organization (WHO) [2]. The statistics for the global incidence and mortality rates for major types of cancer are shown in Fig.1.1 [3].

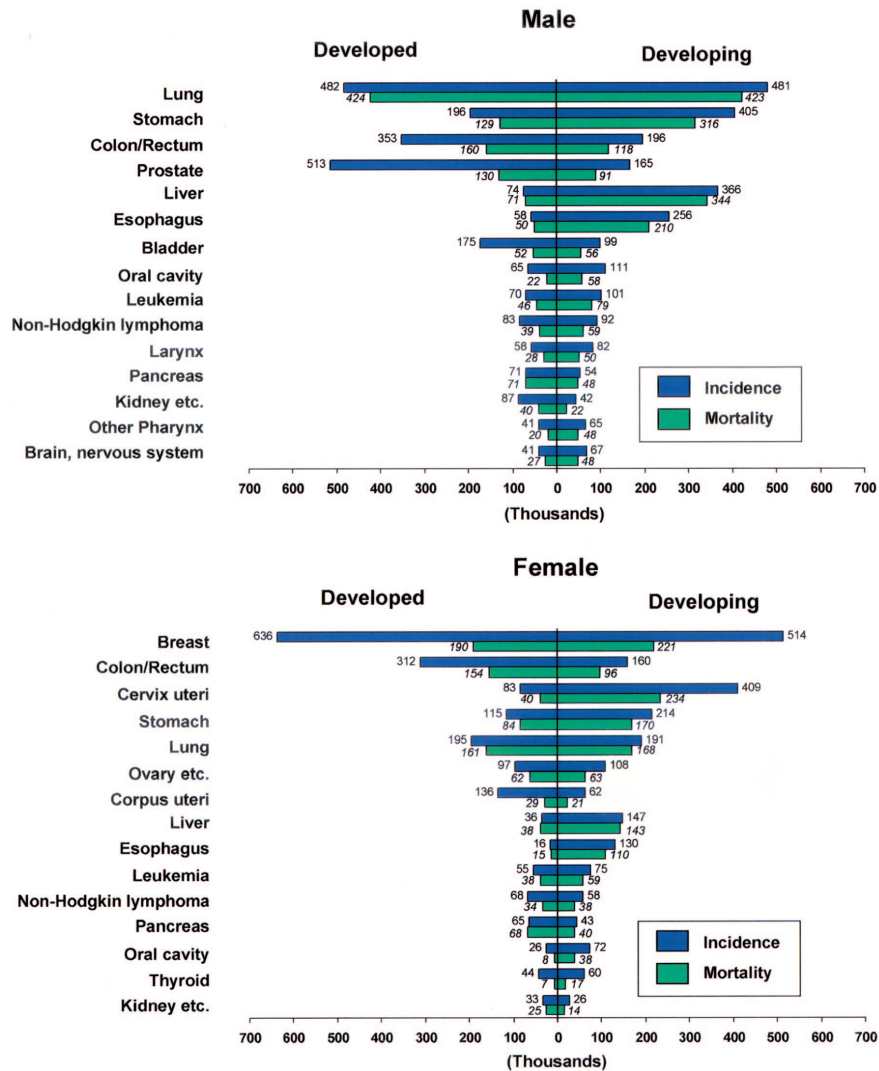


**Figure 1.1** Global incidence and mortality rates for cancer [3].

In developed countries, cancer is the second biggest cause of death after cardiovascular disease. The situation is also alarming in developing countries. Some cancers are more common in developed countries, e.g., prostate, breast and colon cancer. Cancer is characterized by a population of cells that grow and divide without respect to normal limits, these cells invade and destroy adjacent tissues and may spread to distant anatomic sites through a process called metastasis [4]. Cancer is caused by a number of factors such as unhealthy lifestyle (tobacco and alcohol use, inadequate diet, physical inactivity), exposure to environmental carcinogens (ultraviolet and ionizing radiation), chemical carcinogens (asbestos, tobacco) and biological carcinogens (virus, bacteria, fungi). There are different types of cancers according to localization, cell type, malignancy etc., but all share a common trait – if undetected and untreated at an early stage, the risk of death is high [3].

Nanotechnology is a multi-disciplinary field, integrating traditional disciplines such as physics, materials science, biology and chemistry for the development of novel materials and technologies. Nanotechnology is a growing area of research and has developed to such an extent that it has become possible to synthesize, characterize and tailor the functional properties of nanoparticles for improved therapeutics and diagnostics in medicine [5-8]. A major thrust of research in nanomedicine has been the development of nanocarriers for passively or actively targeted drug delivery for cancer therapy [9-13].

Magnetic nanoparticles (MNP) are a major class of nanoscale materials, which offer very attractive possibilities in biomedicine. MNP have sizes smaller than or comparable to those of a cell (10–100  $\mu\text{m}$ ), a virus (20–450 nm), a protein (5–50 nm) or a gene (2 nm wide and 10–100 nm long). MNP can be functionalized by either polymers or inorganic materials to which drugs or biological agents can be attached and driven by an external

magnetic field gradient. The penetrability of magnetic fields into human tissue enables such functionalized MNP to deliver anticancer drugs, radionuclide atoms and genes to a targeted region of the body, such as a tumor [14]. MNP can also be heated by an external high frequency alternating magnetic field, resulting in a moderate degree of tissue warming causing malignant cell destruction by thermal ablation/ hyperthermia of tumors [15]. MNP are also used as contrast agents to improve the resolution of tumor imaging in magnetic resonance imaging (MRI) [16].

Several types of MNP with various chemical compositions have been proposed and evaluated for biomedical applications to exploit nanoscale magnetic phenomena, such as enhanced magnetic moments and superparamagnetism [17]. Composition, size, morphology and surface chemistry can now be tailored by various processes to tune the *in-vivo* behaviour of nanoparticles [18]. Coated magnetic carrier particles (MCP) are comprised of small aggregates of magnetic nanoparticles with a biocompatible coating, which provides stabilization under physiological condition. Targeting MCP to the tumor using an external magnetic field enables the functionalized particles to be used as multimodal therapeutic agents combining drug delivery, hyperthermia and *in-vivo* imaging, which is a major advantage over non-magnetic particles.

## 1.1 Biomedical applications of magnetic nanoparticles

The major biomedical applications of magnetic nanoparticles are as follows:

### 1.1.1 Therapeutic applications

**Drug delivery:** Since the pioneering concept proposed by Freeman *et al* [19] that fine iron particles could be transported through the vascular system and concentrated in a specific region of the body with the aid of a magnetic field, the use of magnetic particles

for the delivery of drugs or antibodies to the organs or tissues has become an attractive field of research [20]. MNP have been evaluated extensively for the targeted delivery of pharmaceuticals through magnetic drug targeting (MDT) [21, 22] as well as for active targeting through the attachment of high affinity ligands [23]. Drug localization is based on the application of an external magnetic field, which retains the drug loaded MCP at a specific target site. They can then be internalized by the endothelial cells of the tissue. The small size of MNP enables their transport through the capillary systems of organs and tissues. MNP offer an attractive means of targeting therapeutic agents specifically to a diseased site, while simultaneously reducing dosage and deleterious side effects associated with non-specific uptake of cytotoxic drugs by healthy tissue, hence they have the potential to overcome the limitations associated with systemic distribution of conventional chemotherapies.

**Hyperthermia:** Hyperthermia is a therapeutic procedure used to raise the temperature of a region of the body affected by malignancy. Tumor cells are more sensitive to temperature than normal cells, hence there is a direct cancer cell killing effect for temperatures in the range of 42-47°C [24-27]. Hyperthermia involves dispersing MNP throughout the target tissue and then applying an AC magnetic field of sufficient strength and frequency to heat up the particles. This heat is conducted into the surrounding diseased tissue and the temperature is maintained above the therapeutic threshold of 42°C for 30 min or more to destroy the tumor.

### 1.1.2 Diagnostic applications

**NMR imaging:** The development of the NMR imaging technique for clinical diagnosis has suggested the exciting possibility of a new class of pharmaceuticals, called magnetopharmaceuticals. MNP are administered to a patient to enhance the image

contrast between normal and diseased tissue, thus indicating the status of organ functions or blood flow [28]. The contrast agents used in most NMR imaging studies to date have been paramagnetic. Superparamagnetic particles represent an alternative class of NMR contrast agents that are usually referred to as  $T_2$  (transversal relaxation time) or  $T_2^*$  contrast agents as opposed to  $T_1$  (longitudinal relaxation time) agents such as paramagnetic gadolinium (III) chelates [29]. Commercial iron oxide nanoparticles of maghemite (Endorem® and Resovite®) have been used as contrast agents in NMR imaging for the location and diagnosis of brain and cardiac infarcts, liver lesions and tumors [30].

**Cell labelling and magnetic separation:** Magnetic separation is based on the following processes: (i) tagging or labelling of the desired biological entity with biocompatible magnetic nanoparticles and (ii) separation of these tagged entities via a fluid-based magnetic separation device. Magnetic separation has been successfully applied to many aspects of biomedical and biological research. It has proven to be a highly sensitive technique for the selection of rare tumor cells from blood [31]. This has led to the enhanced detection of malarial parasites in blood samples, either by utilizing the magnetic properties of the parasite [32] or through labelling the red blood cells with an immunospecific magnetic fluid [33].

Researchers are seeking to exploit the properties of MNP to obtain medical breakthroughs in diagnosis [34-36] and improved drug delivery for cancer treatment [14, 21, 37-39]. *The synthesis, characterization, property evaluation and modelling of MCP for magnetically targeted drug delivery are described in this thesis.*

---

## 1.2 The need for drug targeting: motivation

The common methods of cancer treatment are surgery, radiotherapy, thermotherapy and chemotherapy [24]. However, conventional cancer therapies suffer from numerous drawbacks. Surgery is an invasive method by which the tumor is physically removed from the body. There is a risk of complications during the surgical process and also the possibility of post operative problems such as pain, infection, bleeding, blood clots and slow recovery of organ functions [40]. Radiotherapy involves exposing cancer cells to high-energy radiation such as gamma rays or X-rays to kill cancer cells. However, radiotherapy is non-specific in nature, i.e., it destroys healthy cells as well as cancerous cells. Side effects from radiotherapy include fatigue, damage to the skin, lungs, digestive tract, mouth and throat, changes in brain function, decrease in fertility and in some cases triggering of secondary cancers [40].

Common hyperthermia techniques are radiofrequency capacitance hyperthermia (RFCH), whole body hyperthermia (WBH) and isolated hepatic perfusion hyperthermia (IHPH) [24, 41, 42]. Due to the non-specificity of these methods, attainable tumor temperatures are limited to minimize the risk of collateral organ damage. There is high risk of death by organ failure due to the uniformly elevated body and hepatic temperatures, particularly in the case of WBH and IHPH [41].

In chemotherapy, highly cytotoxic drugs are injected intravenously and transported to the tumor site through blood flow. This treatment involves a schedule of regular administrations of drugs distributed over several days. The major disadvantage associated with chemotherapy is the general systemic distribution of drug throughout the body, which results in insufficient drug concentration at the tumor, decreasing the effectiveness of treatment. More importantly, these cytotoxic drugs are highly non-specific in nature,

---

i.e., they kill both healthy as well as tumor cells, resulting in serious side effects. These side effects include hair loss, nausea, diarrhea, infertility, cognitive impairment, heart damage, nerve damage, liver damage, lung damage, etc [40]. It is therefore very important to selectively target chemotherapeutic agents to the tumor as precisely as possible in order to reduce systemic distribution of cytotoxic drugs and to reduce the associated side effects. Targeted drug delivery can improve the outcome of chemotherapy by allowing the maximum fraction of drugs to interact exclusively with cancer cells, without adverse side effects to non-targeted sites [43]. This need has prompted a search for drug delivery method, which can address the limitations of conventional cancer treatment and provide more effective cancer therapy.

### **1.3 Magnetic drug targeting: the solution**

There has been keen interest in the development of a novel drug delivery system, which can deliver drug exclusively to specific parts of the body. A magnetically targeted drug delivery system using MCP targeted by an external magnetic field is a promising alternative to solve critical issues associated with conventional cancer therapies [18, 37, 38, 44-46]. In magnetically targeted drug delivery, MCP loaded with anti-cancer drug are injected into the patient body via the human circulatory system. These MCP are localized at the tumor by applying an external magnetic field near the tumor (Fig. 1.2). Drug release occurs following the localization of MCP in the tumor, either via enzymatic activity or changes in physiological conditions, e.g., pH, osmolality, or temperature [47]. Thus magnetically targeted drug delivery increases drug concentration at the tumor and minimizes the distribution of drug in healthy tissue. If the magnetic particles are coated with a gold shell, this shell can provide advantages such as improved computed tomography (CT) contrast, it can be heated by near infrared (NIR) light irradiation due to

photothermal effect; this multi modal treatment (synergistic effects of thermo therapy and chemotherapy) improves the efficacy of cancer therapy [48-51]. Despite the fact that systemic chemotherapy offers no survival benefit for cases of advanced Hepato Cellular Carcinoma (HCC), magnetically targeted chemotherapy offers improved survival and quality of life for these patients [52-54].

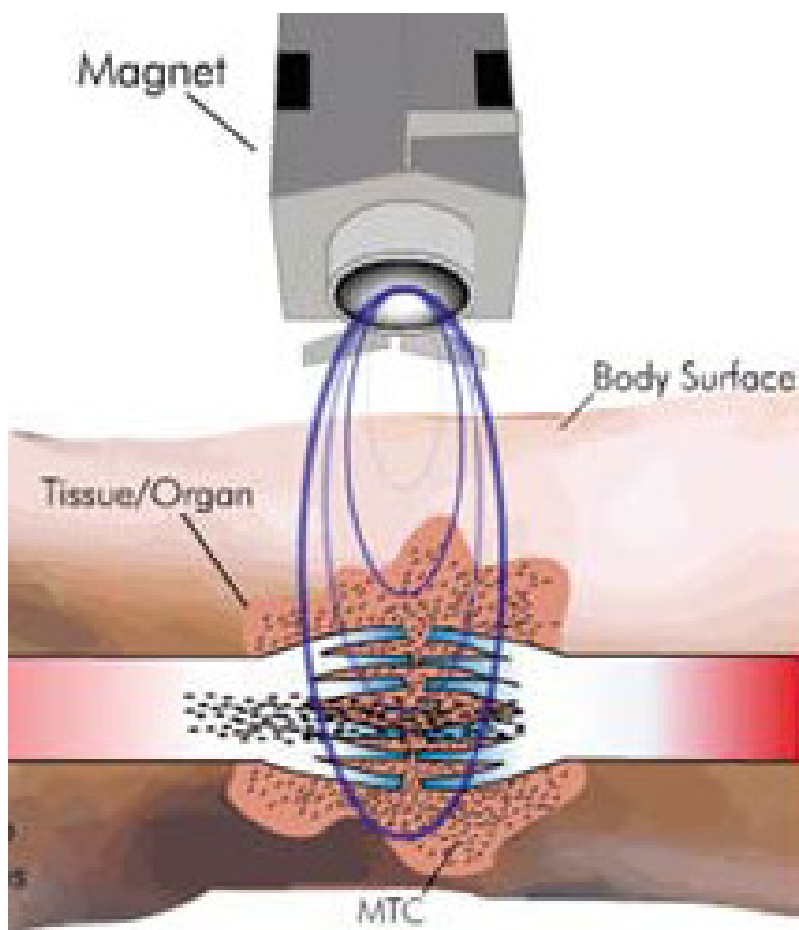


**Figure 1.2** Schematic representation of magnetic drug targeting to a specific region [55].

#### **1.4 Objective and scope of the work**

The delivery of anti-cancer drugs to specific target sites with minimum side effects is a challenge in conventional cancer treatments. The objective of this work is to study the

conditions for targeting of MCP to site specific drug delivery. The focus is on the synthesis, characterization and property evaluation of coated MCP with *in-vitro* experiments and modelling studies of the efficacy with which such particles can be captured by an external magnetic field. Figure 1.3 provides an overview of the thesis.

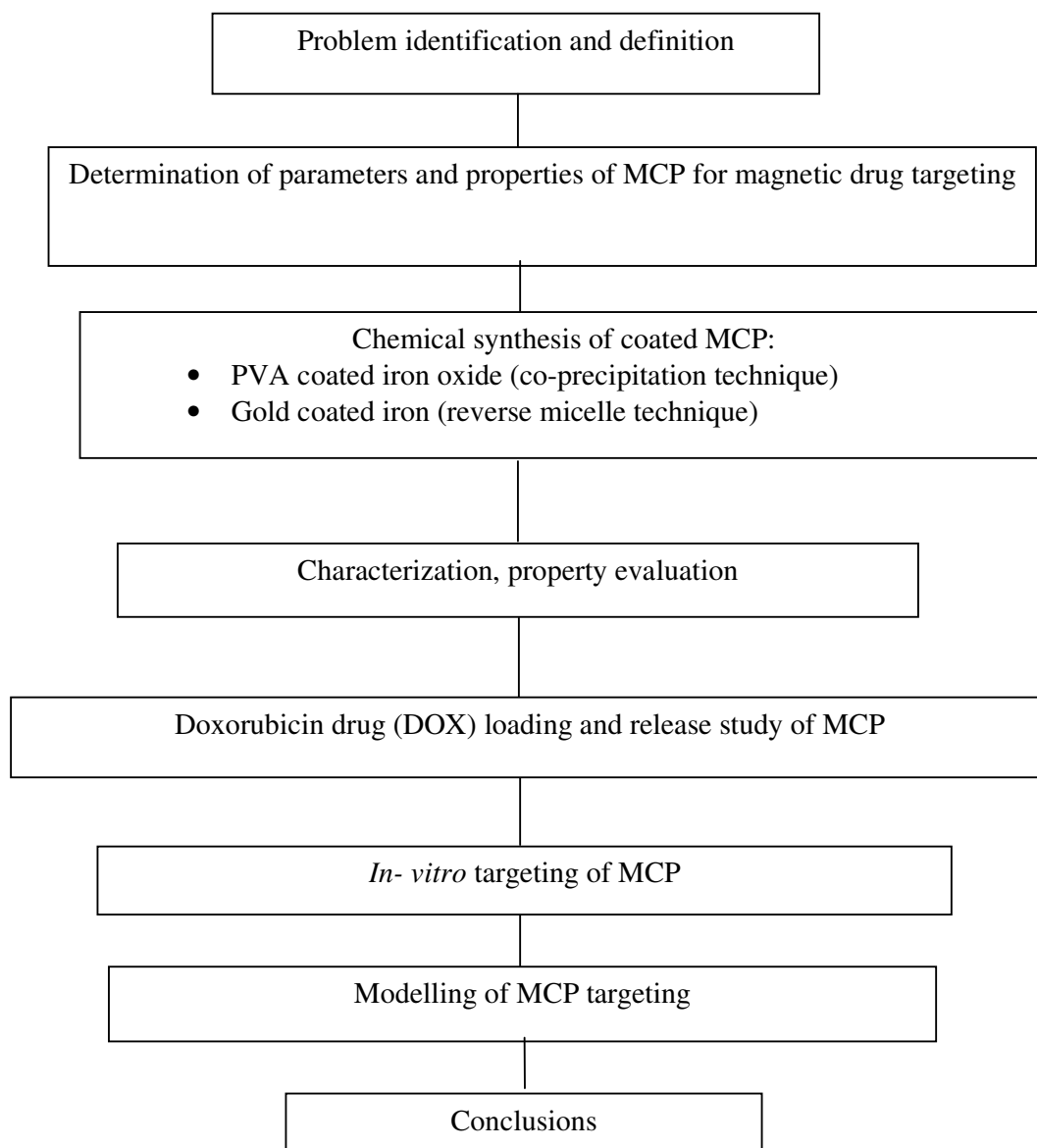


**Figure 1.3** Overview of the thesis.

Iron oxide nanoparticles are biocompatible in the doses required for therapeutic use and are sold commercially (i.e., Endorem, Feridex IV), they are currently in routine use as MRI contrast enhancement agents [36, 56, 57]. Superparamagnetic iron oxides nanoparticles, e.g., the commercially available Combidex, have undergone clinical trials for the use in detection of lymph node metastases [58]. The favourable biocompatibility and biodegradability of iron oxide nanoparticles have contributed greatly to their widespread use in biomedical applications, iron ions are incorporated as hemoglobin by erythrocytes during metabolism [59]. *In-vivo* experiments on animal models have shown that iron oxides are suitable for drug delivery [37, 60]. Human clinical trials for drug delivery have been conducted with iron oxide based ferrofluids, the injected dosage being well tolerated by patients [44].

Generally, particles with hydrophobic surfaces are more readily removed by the body's reticulo-endothelial system (RES) [61, 62]. However, hydrophilic coatings increase circulation time of MCP by reducing immediate clearance by the RES [63]. Hydrophilic polymer polyvinyl alcohol (PVA) is useful as a coating of magnetic particles because of its biocompatibility, biodegradability and it can also be readily functionalized [18, 64-66]. Another carrier system comprising of gold coated iron (Fe@Au) nanoparticles is of special interest. Bare iron nanoparticles can not be directly used for drug delivery since (a) free iron induces the formation of dangerous free radicals, (b) iron nanoparticles can aggregate resulting in the formation of thromboses and (c) free iron nanoparticles are easily oxidized. By coating the iron nanoparticles with gold, the oxidation of iron can be minimized. The interaction of gold nanoparticles with phagocytes showed the biocompatible properties of gold nanoparticles such as nontoxicity, nonimmunogenicity and high tissue permeability without hampering cell functionality [67]. Gold can also be

readily functionalized by the use of amine [68] and thiol groups [69], which facilitates the attachment of biologically relevant molecules.

In this work, Doxorubicin (DOX) was chosen as a model drug for drug loading and release studies of MCP. DOX is an anti-cancer drug used in chemotherapy. It is classified as an anthracycline antibiotic which interacts with DNA by intercalation [70]. DOX is orange-red crystalline solid, its chemical structure is given below:

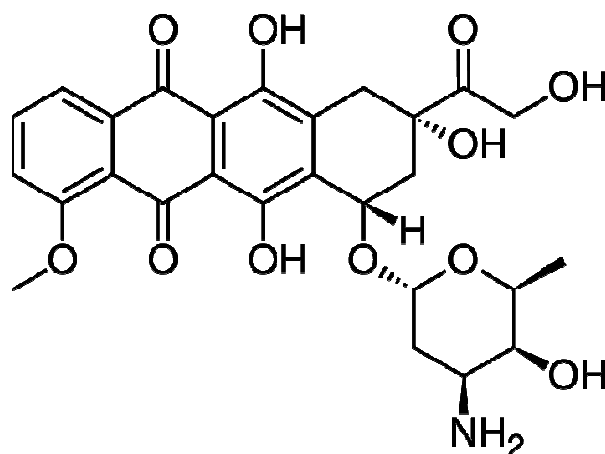


**Figure 1.4** Chemical structure of DOX [70].

Doxorubicin is commonly used to treat cancers of the bladder, breast, stomach, lung, ovaries, thyroid, multiple myeloma, pancreas, prostate, sarcomas, testis (germ cell), hyroid and uterus [71].

In this work, gold coated iron (Fe@Au) and PVA coated iron oxide (PVA-IO) MCP were investigated. The anti-cancer drug doxorubicin (DOX) was attached to these MCP and the binding mechanism of DOX with the coating was examined. DOX loading and release profiles as well as *in-vitro* targeting of these MCP were studied in order to determine the suitability of these MCP for magnetically targeted drug delivery. From the *in-vitro* experimental targeting of MCP results, it was found that 90% of PVA-IO and 86% of Fe@Au MCP can be retained at a field gradient of  $25 \text{ T m}^{-1}$  and a flow rate of  $1 \text{ mm s}^{-1}$ .

The modelling of targeting of MCP showed that  $\text{Fe}_3\text{O}_4$ ,  $\text{Fe@Au}$ , PVA-IO MCP (100 nm) can be targeted to the breast tumor and other skin tumors by a typical permanent magnet (maximum field gradient of  $25 \text{ T m}^{-1}$ ). The modelling results also showed that MCP with higher saturation magnetization e.g., Fe and FeCo can be targeted to lung, liver, kidney, pancreas tumors or a higher magnetic field gradient ( $100 \text{ T m}^{-1}$ ) can be used to localize these MCP to tumors situated deep inside the body. Computational Fluid Dynamics (CFD) simulations showed that when a suspension of MCP (ferrofluid) enters into the blood vessel, ferrofluid creeps along the wall of the blood vessel under an external magnetic field. Simulations also showed that for a given magnetic field strength, the time of exposure of magnetic field can be optimized for a given diameter of blood vessel and blood flow rate.

### 1.5 Novelty of work

The delivery of anticancer agents to specific target sites with minimum side effects is a challenge in conventional cancer treatments. Using a magnetic field to capture MCP loaded with anticancer drugs at the tumor site offers an alternative methodology for the targeted delivery of drugs. So far, studies of the conditions under which magnetic targeting is feasible have been mostly empirical. The novelty of the work lies in the synthesis, characterization and property evaluation of MCP for drug targeting combined with *in-vitro* experiments and modelling studies of the efficacy with which these particles can be retained at a given site by an external magnetic field. Concurrent drug loading and release studies of these MCP were also conducted. Contributions of this work are:

- $\text{Fe@Au}$  nanoparticles were synthesized by the reverse micelle method and particles were characterized. DOX was attached to  $\text{Fe@Au}$  MCP and the interaction of DOX with the gold coating was examined. For the first time, DOX

---

loading and release profiles of Fe@Au MCP as well as *in-vitro* targeting of these MCP at flow rates of the fluid comparable to that encountered in the capillary bed of a tumor were studied. A significant quantity of DOX (94%) was loaded onto the Fe@Au MCP and 25% of adsorbed DOX was released. Up to 86% of Fe@Au MCP was captured at a field gradient of  $25 \text{ T m}^{-1}$  and flow rate of  $1 \text{ mm s}^{-1}$ .

- Another MCP system, i.e., PVA coated iron oxide (PVA-IO) nanoparticles was studied. The synthesis, characterization, property evaluation as well as combined *in-vitro* drug loading, drug release and drug targeting using these PVA-IO MCP were carried out. PVA-IO nanoparticles were loaded with DOX and 45% of adsorbed drug was released. Up to 90% of PVA-IO MCP was captured at a field gradient of  $25 \text{ T m}^{-1}$  and flow rate of  $1 \text{ mm s}^{-1}$ .
- Modelling of the targeting of MCP at the tumor site was performed by determining the trajectory and distance of capture of MCP under various flow rates of fluid, magnetic properties of MCP and MCP size. The modelling results showed that  $\text{Fe}_3\text{O}_4$ , Fe@Au, PVA-IO MCP (100 nm size) can be targeted to breast tumors and other skin tumors by a typical permanent magnet. To target tumors situated deep inside the body, MCP with superior magnetic property, e.g., Fe and FeCo, or an external magnet having higher magnetic field gradient ( $100 \text{ T m}^{-1}$ ) must be chosen.
- The trapping of MCP was studied using nonlinear CFD simulations and these results were compared qualitatively with experimental results. Simulations showed that the ferrofluid creeps along the bottom wall under the influence of a magnetic field, which may cause friction and remove the drug before it reaches the targeted zone, hence drug injection should be as close as possible to the malignant location. For a given magnetic field strength, the time of exposure to

---

the magnetic field can be optimized once the diameter of the blood vessel and blood flow rate are known.

## 1.6 Methodology

A literature survey was carried out to examine the choice of synthesis procedure of coated magnetic nanoparticle carriers. The following routes were carried out to synthesize the magnetic carriers:

- Fe@Au nanoparticles were synthesized by the reverse micelle method.
- PVA-IO nanoparticles were synthesized by coprecipitation of iron oxide and subsequently coated with polyvinyl alcohol (PVA).

Phase identification and structural analysis of the carriers were performed by X-ray diffraction (XRD). The size and morphological characterization of the individual particles were carried out by transmission electron microscopy (TEM). Magnetic measurements were performed by vibrating sample magnetometry (VSM). The mass fraction of polymer attached to the magnetic particles was determined by thermo-gravimetric analysis (TGA).

Fe@Au and PVA-IO nanoparticles were loaded with the anti-cancer drug DOX, drug loading and release properties were studied by measuring the DOX concentration using a UV-vis spectrophotometer. The binding mechanism of DOX with the coating was examined by Fourier transform infrared (FTIR) spectroscopy. An *in-vitro* apparatus simulating the human circulatory system was constructed and used to determine the retention of MCP under different flow rates of fluid and varying magnetic field gradients. CFD simulations of MCP trapping by an external magnetic field were carried out using Ansys-Fluent software.

---

*In summary, the synthesis, characterization, property evaluation and modelling of MCP were performed to examine their potential for magnetic drug targeting applications.*

## 1.7 Organization of the thesis

The thesis consists of 5 chapters.

- **Chapter 1** is the introduction of the thesis. The limitations of conventional cancer treatments are highlighted and a possible solution, i.e., magnetically targeted drug delivery is suggested. The objective and scope of the thesis are presented along with a brief description of methodology.
- **Chapter 2**, literature review contains an introduction to magnetism and its relevance to medical applications. The state of the art of the development of various magnetic drug carriers, their synthesis techniques as well as *in-vitro* and *in-vivo* magnetic targeting using these magnetic carriers are discussed.
- **Chapter 3** describes the experimental procedures for synthesis, characterization, property evaluation and *in-vitro* targeting as well as drug loading and drug release of MCP used in this work. The development of a magnetic drug targeting model is also presented.
- **Chapter 4** presents results and discussion related to synthesis and characterization of Fe@Au as well as PVA-IO nanoparticles, DOX loading and release studies and *in-vitro* experimental capture of these MCP. Modelling of magnetic drug targeting and the CFD simulation results are also presented.
- **Chapter 5** presents the conclusions and future scope of this work.

## **Chapter 2**

### **Literature Review**

In this chapter, some fundamental concepts of magnetism are briefly discussed. To control the motion of MCP within the body, the magnetic force due to an externally applied magnetic field and a hemodynamic drag force due to blood flow combine to exert a total vector force on the MCP. To overcome the influence of blood flow to achieve the desired external magnetic field controlled trapping, the magnetic force due to the external magnetic field must be larger than the drag force. The relevant equations to model this targeting are discussed. The magnetic core materials, coating materials and the role of coatings are discussed. Wet chemical routes to synthesize magnetic nanoparticles are simpler and more efficient than physical methods with appreciable control over size, composition and sometimes even the shape of the nanoparticles [72, 73]. In this chapter different synthesis methods to produce magnetic nanoparticles for biomedical applications are presented.

#### **2.1 Classes of magnetic materials**

Magnetism arises from the orbital and spin motion of electrons in the material. Magnetic materials are classified on the basis of their response to an external magnetic field. Some fundamental concepts of magnetism are briefly discussed here. Further details can be found in textbooks on magnetism [74, 75].

### 2.1.1 M–H curves

Figure 2.1 represents a schematic diagram of a blood vessel in which magnetic particles are present. The magnetic particles and the biomolecules in the blood vessel have different magnetic properties, which are illustrated in Fig. 2.1.

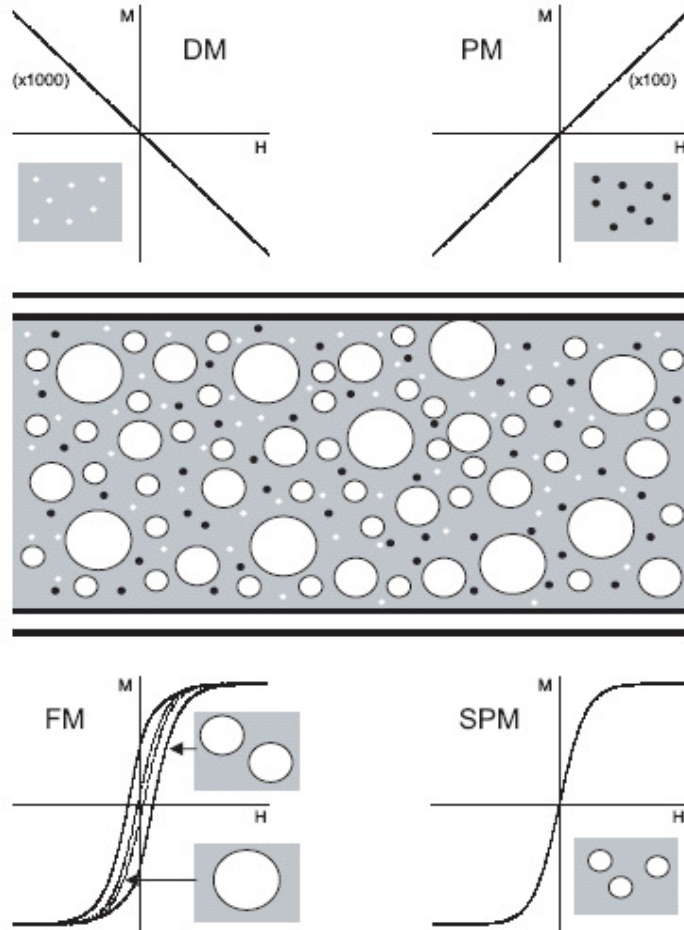


**Figure 2.1.** Magnetic responses associated with different classes of magnetic material, illustrated for a hypothetical situation in which ferromagnetic particles of a range of sizes from nanometre up to micron scale are injected into a blood vessel.  $M$ – $H$  curves are shown for diamagnetic (DM) and paramagnetic (PM) biomaterials in the blood vessel, and for the ferromagnetic (FM) injected particles, where the response can be either multi-domain (--- in FM diagram), single-domain (— in FM diagram) or superparamagnetic (SPM), depending on the size of the particle [76].

If a magnetic material is placed in a magnetic field of strength ( $\mathbf{H}$ ), the magnetic induction ( $\mathbf{B}$ ) is given as,

$$\mathbf{B} = \mu_0(\mathbf{H} + \mathbf{M}) \quad (2.1)$$

where  $\mu_0$  is the permeability of free space,  $\mathbf{M}$  is the magnetization ( $=\mathbf{m}/V$ ) represented as magnetic moment per unit volume, where  $\mathbf{m}$  is the magnetic moment and  $V$  is the volume of the material. All materials respond to the magnetic field depending on their atomic structure. The classification of a material's magnetic properties is based on its magnetic susceptibility ( $\chi$ ), which is defined by the ratio of the induced magnetization ( $M$ ) to the applied magnetic field ( $H$ ) as,

$$\chi = M/H, \quad (2.2)$$

$\chi$  holds in the limit that  $H$  approaches 0. In SI units,  $\chi$  is dimensionless and both  $M$  and  $H$  are expressed in  $\text{A.m}^{-1}$ .

Diamagnetism arises from orbiting electrons when these electrons are subjected to an applied magnetic field. Diamagnetism is found in all materials but it is usually very weak and characterized by negative susceptibility. In diamagnetic materials, the magnetic moment is anti-parallel to  $H$  resulting in very small and negative susceptibilities ( $\chi = -10^{-6}$  to  $-10^{-3}$ ). They do not retain magnetic properties when the external field is removed. For paramagnetic materials, partial alignment of atomic magnetic moments in the direction of external magnetic field takes place, leading to positive susceptibility ( $\chi = 10^{-6}$  to  $10^{-1}$ ). The magnetization is zero when the field is removed, since the magnetic moments associated with individual atoms do not interact magnetically in paramagnetic materials. However, some materials exhibit a permanent magnetic moment in the absence

of an external field; these are classified as ferromagnets, ferrimagnets and antiferromagnets, where the prefix refers to the nature of the coupling interaction between the electrons within the material [75]. In ferromagnets, the atomic moments exhibit strong interactions produced by large exchange forces, which result in the alignment of atomic moments in the same direction. In ferrimagnets, two sublattices couple through a super exchange mechanism resulting in antiparallel alignment. In antiferromagnets, the exchange coupling between neighboring moments causes moments to align in an antiparallel fashion.

The  $M$ – $H$  curve has a characteristic sigmoidal shape,  $M$  reaches a saturation value at large value of  $H$ . Furthermore, a hysteresis loop is observed in ferromagnets and ferrimagnets. Hysteresis arises from the irreversibility in the magnetization process due to (a) pinning of magnetic domain walls at impurities or grain boundaries within the material, and (b) intrinsic effects such as the magnetic anisotropy of the crystalline lattice [77]. The shape of the hysteresis loop depends on particle size, e.g., large particles (of the order of micron size or more) have a multi-domain structure and a narrow hysteresis loop, whereas smaller particles have a single domain structure and a broad hysteresis loop. All ferro- and ferrimagnets above their corresponding threshold temperatures behave like paramagnets, since thermal energy is sufficiently high to cause random fluctuations of magnetic moments, eliminating magnetic order. On the other hand, superparamagnetism is observed in particles that are so small that they consist of a single magnetic domain and ambient thermal energy is sufficient to overcome coupling forces, causing the atomic magnetic moment to fluctuate randomly. This leads to the anhysteretic but still sigmoidal  $M$ – $H$  curve (Fig. 2.1).

The value of coercivity is also size-dependent. As particle size decreases, coercivity increases to reach a maximum at a threshold particle size (typical values are 15 and 35 nm for Fe and Co metallic particles, respectively, while for  $\text{SmCo}_5$  it is 750 nm) [78] due to the transformation from a multi domain to a single domain structure. In bulk magnetic materials, a multidomain structure is constituted by regions of uniform magnetization, separated by domain walls, which minimize the sum of the energy due to the external magnetic field (magnetostatic energy) and the energy of the domain walls. As the volume of the magnetic particle decreases, the size of the domains and the width of the walls reduces until the energy cost to produce a domain wall is greater than the corresponding reduction in magnetostatic energy. Consequently, the system no longer divides itself into smaller domains, instead the structure maintains a single domain. In a single domain particle, it is not possible for magnetization reversal to take place by means of the boundary displacement process, which requires relatively weaker fields. Instead the magnetization of the particle must rotate as a whole, a process that requires a large field, depending on the anisotropy energy of the material. A further decrease in particle size causes the coercivity value to decrease rapidly to zero resulting in a transition to the superparamagnetic state. Superparamagnetism follows the activation law for the relaxation time  $\tau$  of the net magnetization of the particle [79].

$$\tau = \tau_0 \exp (\Delta E/k_B T), \quad (2.3)$$

where  $\Delta E$  is the energy required for moment reversal and  $k_B T$  is the thermal energy ( $k_B$  is Boltzman constant,  $T$  is temperature). The energy barrier is expressed as  $\Delta E = KV$ , where  $K$  is the anisotropy energy density and  $V$  is the particle volume. For small particles  $\Delta E$  is comparable to  $k_B T$  at room temperature, hence superparamagnetism is observed in small particles.

### 2.1.2 Action of forces on magnetic nanoparticles

Vector field theory can be used to understand the magnetic force needed to manipulate magnetic nanoparticles using an external magnetic field. The following discussion follows that of Pankhurst [76]. The magnetic force ( $\mathbf{F}_{mag}$ ) acting on a point-like magnetic dipole moment ( $\mathbf{m}$ ) under a magnetic field gradient ( $\mathbf{B}$ ) is given by:

$$\mathbf{F}_{mag} = (\mathbf{m} \cdot \nabla) \mathbf{B} \quad (2.4)$$

When magnetic nanoparticles are suspended in a weakly diamagnetic medium, such as water, the total moment on the particle can be expressed as  $\mathbf{m} = V\mathbf{M}$ , where  $V$  is the volume of the particle and  $\mathbf{M}$  is its volumetric magnetization. Further,  $\mathbf{M} = \Delta\chi\mathbf{H}$ , where  $\Delta\chi = \chi_m - \chi_w$  is the effective susceptibility of the particle relative to the water. For the case of a dilute suspension of nanoparticles in water, the overall response of the particles can be approximated by  $\mathbf{B} = \mu_0\mathbf{H}$ , so that Eqn. 2.4 becomes

$$\mathbf{F}_{mag} = V\Delta\chi(\mathbf{B} \cdot \nabla) \mathbf{B} / \mu_0 \quad (2.5)$$

Furthermore, if there are no time-varying electric fields or currents in the medium, the Maxwell equation  $\nabla \times \mathbf{B} = 0$  can be applied to the following mathematical identity,

$$\nabla(\mathbf{B} \cdot \mathbf{B}) = 2(\mathbf{B} \cdot \nabla) \mathbf{B}, \quad (2.6)$$

to obtain a more intuitive form of Eqn. 2.5,

$$\mathbf{F}_{mag} = V\Delta\chi \nabla B^2 / 2\mu_0, \text{ or}$$

$$\mathbf{F}_{mag} = 0.5V\Delta\chi \nabla(\mathbf{B} \cdot \mathbf{H}) \quad (2.7)$$

---

in which the magnetic force is related to the differential of the magnetostatic field energy density,  $0.5 \mathbf{B} \cdot \mathbf{H}$ .

The force that counteracts the magnetic force on the particle in the bloodstream is due to blood flow. Stokes law governs the hemodynamic forces on a particle in a flowing liquid,

$$F = 6 \pi \eta v r, \quad (2.8)$$

where  $F$  is the drag force,  $\eta$  is the viscosity of the fluid,  $v$  is the relative velocity of a spherical particle, and  $r$  is the radius.

## **2.2. Magnetically targeted drug delivery**

The basic shortcoming of most chemotherapeutic agents is their relative non-specificity and thus potential side effects to healthy tissues. To overcome this problem, magnetically targeted drug delivery utilizes an external magnetic field to localize the MCP to increase the site-specific delivery of therapeutic agents. In general, this process involves the attachment of a cytotoxic drug to biocompatible MCP, intravenous injection of these MCP in the form of a colloidal suspension, application of a magnetic field gradient to trap the MCP at the tumor site and the release of drug from the MCP. There are several variables, such as the physicochemical properties of the drug-loaded MCP, magnetic field strength, depth of the target tissue and rate of blood flow, which play a role in determining the effectiveness of this method of drug delivery.

---

**2.2.1. Prior efforts towards magnetically targeted drug delivery**

The use of magnetic nanoparticle carriers for the delivery of chemotherapeutic drugs has evolved since the 1970s. Zimmermann *et al* used magnetic erythrocytes for the delivery of cytotoxic drugs in 1976 [80]. Widder *et al* reported the targeting of magnetic albumin microspheres encapsulating anticancer drug doxorubicin to sarcoma tumors implanted in rat tails [81]. The initial results were encouraging, showing remission of the sarcomas compared to no remission in another group of rats, which were administered with ten times the dose but without magnetic targeting. Since that study, several researchers have reported magnetic drug delivery using animals models including swine [20, 82], rabbits [47] and rats [83-85]. Hafeli *et al* [86] synthesized biodegradable polylactic acid microspheres encapsulating magnetite and the beta-emitter <sup>90</sup>Y for targeted radiotherapy and successfully applied them to tumors [87]. Kubo *et al* [88] implanted permanent magnet at solid osteosarcoma in hamsters in order to deliver cytotoxic drugs using magnetic liposomes, they reported a four-fold increase of drug to the osteosarcoma sites compared to normal intravenous delivery. They also showed a significant increase in anti-tumor activity and no weight-loss as a side effect [89].

Magnetic drug targeting has also been employed to target cytotoxic drugs to brain tumors. Brain tumors are difficult to target because the drug must cross the blood–brain barrier. Pulfer and Gallo [84] reported that magnetic particles (1–2  $\mu\text{m}$ ) could be concentrated at the site of intracerebral rat glioma-2 (RG-2) tumors. Although the concentration of the particles in the tumor was low, it was significantly higher than non-magnetic particles. In a later study, they demonstrated that 10–20 nm magnetic particles were even more effective at targeting these tumors [85]. Mykhaylyk *et al* [90] used magnetite/dextran nanoparticles to target rat glial tumors. Deposition of adriamycin-associated magnetic albumin microspheres was also demonstrated in normal rats by James *et al* [91]. The

transmission electron micrographs showed the extravascular transport of microspheres as early as 2 h after dosing, the microspheres remained in the extravascular tissue for up to 72 h. A Phase I clinical trial was conducted by Lubbe *et al* [44, 92], they demonstrated that the infusion of ferrofluids was well tolerated in most of the patients studied and the ferrofluid was successfully directed to advanced sarcomas without associated organ toxicity. Wilson *et al* reported encouraging results of a clinical study combining magnetic targeting and MRI, in which they were able to monitor the trans-catheter delivery of magnetically targeted doxorubicin to the hepatic artery using intra-procedural MRI [93].

In addition to the clinical trials, theoretical research has been conducted to study the magnetic drug targeting process. It was reported that a magnetic field of 0.8 T is sufficient to exceed linear blood flow in the intratumoral vasculature to localize magnetic carriers [22]. Goodwin *et al* used magnetic carriers (0.5-5  $\mu\text{m}$ ) for drug targeting at the liver and lungs (8-12 cm) in the swine model using a permanent magnet (0.1 T) [94]. Preliminary investigations of the hydrodynamics of drug targeting suggested that a magnetic field of 0.2 T with field gradient of  $8 \text{ T m}^{-1}$  is sufficient to target magnetic nanoparticle carriers in femoral arteries [95]. Theoretical studies of magnetically targeted drug delivery were reported using a two-dimensional (2D) model, suitable for studying the deposition of magnetic particles under the influence of Stokes drag and a magnetic force within a network of blood vessels [96]. Furlani *et al* derived an analytical expression of a cylindrical magnet to calculate the trajectories of magnetic particles and proposed a parametric analysis of magnetic targeting as a function of parameters such as the carrier particle size, properties and volume fraction of the embedded magnetic nanoparticles, properties of the magnet and blood flow rate [97, 98]. Rotariu *et al* used computer simulation of magnetic field of different magnetic configurations such as cylindrical magnet, magnetic circuit with parabolic shape confocal poles and needle magnet to

determine the trajectories of magnetic particles within tumor microvasculature [99]. Another model has been reported to optimize the necessary magnetic field by simulating the magnetic particle's trajectory [100]. A CFD analysis was used for Y-shaped model flow system of blood vessel and the capture efficiency of magnetic particles was determined [101]. Analysis of magnetically induced localization of the ferrofluid at a targeted region was also reported, it was shown that ferrofluid accumulation behaved as a solid obstacle in the flow [102]. Li *et al* simulated the streamlines and contours of concentration of a ferrofluid in a vessel and showed that particle accumulation was affected by the magnetic property of the particles, magnetic field strength and gradient as well as fluid flow rate [103].

### **2.2.2 Magnetic nanoparticles: property requirements**

Magnetic nanoparticles for drug delivery should be endowed with specific characteristics including:

- Biocompatibility - particles should not have toxic or carcinogenic effects in the body.
- Size – particles should be able to diffuse through the intercellular space to achieve uniform distribution in a short time.
- Colloidal stability – particles must be stable in solution. Particles must be small enough to avoid sedimentation due to gravity. They should also avoid segregation, which means their surface needs to be engineered to provide steric or Coulombic repulsion.
- Superparamagnetism – Superparamagnetic nanoparticles are desirable in drug delivery, since such particles do not retain magnetization before and after

---

exposure to an external magnetic field, thus the probability of particle aggregation and possible embolization of capillary vessels can be avoided.

- Functionalization – In the case of intravascular injection, which delivers particles throughout the body, particles need to be conjugated with chemical groups that facilitate preferential targeting to the tumor.

### 2.2.3 Magnetic core materials

There are many magnetic materials available with a wide range of magnetic properties. However, biocompatibility requirement rules out magnetic materials such as cobalt and nickel, which are toxic and unlikely to be used as *in-vivo* biomedical agents without a non-toxic, protective coating. The magnetic core material usually chosen is iron oxide, e.g., magnetite ( $\text{Fe}_3\text{O}_4$ ) and maghemite ( $\gamma\text{-Fe}_2\text{O}_3$ ), mainly due to its low toxicity. The advantage of this magnetic material is that our body is designed to process excess iron, e.g., haemoglobin in our blood is an iron complex and is magnetic in nature. Superparamagnetic iron oxide nanoparticles (SPIONs) are also considered to be biodegradable, with Fe being reused/recycled by cells using normal biochemical pathways for Fe metabolism [104].

### 2.2.4 Coating materials

Nanoparticles are more reactive than bulk materials due to their high surface to volume ratio. As a result, these magnetic nanomaterials need to be protected by a biocompatible coating. This coating also prevents the leaching of potentially toxic components into the body during *in-vivo* applications. There are many choices of coating materials. One has to consider the nature of the coating and the ease of further functionalization to suit specific applications.

There are generally two routes to administer magnetic particles to a particular site in the body. Particles may be injected intravenously to let blood circulation transport them to the region of interest. Alternatively, a suspension of particles can be injected directly into the area where treatment is desired. Both techniques require that the particles do not aggregate and block their own spread. Magnetic nanoparticles have a high tendency to agglomerate and build larger structures even in the absence of a magnetic field. Therefore, these particles need to be coated with a protective shell, which prevents agglomeration. Stabilization of magnetic particles is important to obtain stable magnetic colloidal ferrofluids. The stability of a magnetic colloidal suspension results from the equilibrium between attractive and repulsive forces. Theoretically, four kinds of forces can contribute to the interparticle potential in the system: van der Waals attractive forces, electrostatic repulsive forces, magnetic dipolar forces between two particles and steric repulsion forces [105-107]. Stabilization of magnetic particles can be achieved by tuning one or both of the two repulsive forces: electrostatic and steric repulsion (Fig. 2.2).

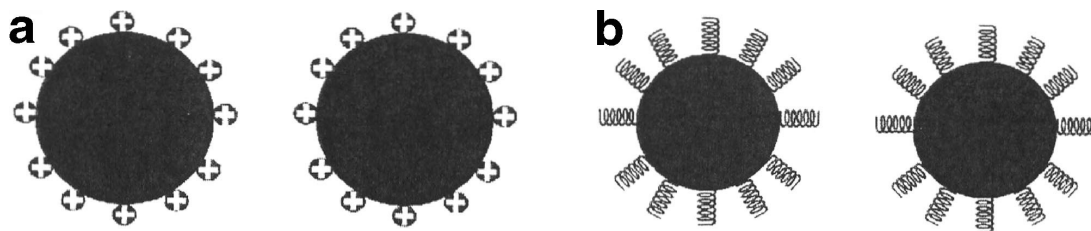


**Figure 2.2** Particles stabilized by (a) the electrostatic layer, (b) steric repulsion [108].

The coating provides binding sites for biomolecules for interaction with particles. There are diverse biological events that need to be considered in choosing a coating. Particles entering the bloodstream are rapidly coated by blood plasma proteins, known as opsonization. Normally, opsonization renders the particles recognizable by the body's major defence system, the reticulo-endothelial system (RES). The RES is a diffuse system

of specialized phagocytic cells, which can engulf inert materials associated with the connective tissue framework of the liver, spleen and lymph nodes. The RES can remove the opsonized particles, hence surface modification is required to ensure particles not only non-toxic and biocompatible, but also stable to the RES. To reduce RES uptake, nanoparticles are sterically stabilized by coating the surface with nonionic surfactants or polymeric macromolecules [63]. This can be achieved by physical adsorption, incorporation during the production of nanoparticles or by covalent attachment to any reactive surface groups.

Particles with highly hydrophobic surfaces are efficiently coated with plasma components and thus rapidly removed from circulation, whereas particles with more hydrophilic surfaces can resist the coating process and therefore are cleared more slowly [61]. Hence the coating should completely cover the particles and be as dense as possible to protect the magnetic core against contact with blood protein and phagocytosis-associated receptors. Longer polymer chains are more effective in suppressing opsonization.

In summary, the coating of magnetic nanoparticles for drug delivery should:

- stabilize nanoparticles in a biological suspension of pH around 7.4.
- reduce polydispersity.
- reduce uptake by the RES.
- provide functional groups at the surface for further derivatization.

#### **2.2.4.1 Monomeric stabilizers**

Functional groups such as carboxylates, phosphates, sulphates are known to bind to the surface of magnetite [109].

- **Carboxylates**

The surface of magnetite nanoparticles can be stabilized in an aqueous dispersion by the adsorption of citric acid [110]. Citric acid is adsorbed on the surface of the magnetite nanoparticles by coordinating via one or two of the carboxylate functional group, leaving at least one carboxylic acid group exposed to the solvent. This makes the surface negatively charged. VSOP C184, an iron oxide particle stabilized by citric acid coating is under clinical investigation [111]. Other monomeric carboxylate coatings, such as gluconic acid [112], dimercaptosuccinic acid [113], and phosphorylcholine [114] have also been used for the stabilization of iron oxide in aqueous medium. The stability range is strongly dependent on pH and the concentration of adsorbed acids.

- **Phosphates**

Several researchers have studied the possibility of using alkanephosphonic acid as efficient binding ligands on the surface of  $\text{Fe}_2\text{O}_3$  nanoparticles and as stabilizer for particle dispersion in organic solvents [115, 116]. Sahoo *et al* reported that alkyl phosphonates and phosphates could be used for obtaining thermodynamically stable dispersions of magnetic ferrite nanoparticles [109]. Superparamagnetic nanosized magnetite particles have also been prepared by controlled coprecipitation from solution containing  $\text{Fe}^{2+}$  and  $\text{Fe}^{3+}$  ions in the presence of highly hydrophilic poly(vinylalcohol phosphate) (PVAP) [64].

---

#### 2.2.4.2 Inorganic stabilizers

Magnetic nanoparticles can be coated with silica [117, 118], gold [119, 120] and gadolinium(III) [121]. These coatings not only provide stability to the nanoparticles in solution but also help in the binding of various biological ligands to the nanoparticle surface.

- **Silica**

Silica coating on the surfaces of magnetite nanoparticles reduces aggregation in the liquid, improves chemical stability and provides better protection against toxicity [122]. This coating stabilizes the magnetite nanoparticles by (a) shielding the magnetic dipole interactions and (b) since silica nanoparticles are negatively charged, this coating enhances the Coulombic repulsion of the magnetic nanoparticles [123]. Ferumoxsil (AMI-121) composed of iron oxide particles coated with a layer of inert silicon ([3-(2-amino-ethylamino)propyl]trimethoxysilane) has been tested in clinical trials by oral administration [124]. Various approaches have been explored to generate magnetic silica nanospheres. The Stober process involves hydrolysis and condensation of a sol-gel precursor e.g., tetraethyl orthosilicate (TEOS), by this process silica colloids loaded with superparamagnetic iron oxide nanoparticles have been prepared [125]. Another method is based on the deposition of silica from silicic acid solution, this method is easy to perform, more efficient in covering a higher proportion of the magnetite surface than the TEOS method, the particle size can also be controlled by changing the ratio of  $\text{SiO}_2/\text{Fe}_3\text{O}_4$  [126].

Another synthesis method is an emulsion method, in which micelles or reverse micelles are used to confine and control the silica coating. Yang *et al* prepared monodisperse silica coated superparamagnetic iron oxide nanoparticles by the emulsion method and

demonstrated entrapment of biological macromolecules in the pore of the nanoparticles [127]. Tartaj *et al* synthesized submicron size silica coated magnetic spheres by the pyrolysis method [118]. The advantage of having surface enriched in silica is the presence of surface silanol ( $-\text{Si}-\text{OH}$ ) groups, which can easily react with various coupling agents to covalently attach specific ligands to these magnetic particles. For example, amine groups have been introduced on the surface of silica coated  $\text{Fe}_3\text{O}_4$  nanoparticles by hydrolysis and condensation of an organosilane, such as aminopropyltriethoxysilane, on the surfaces of  $\text{Fe}_3\text{O}_4$  nanoparticles [128].

- **Gold**

Gold is another inorganic coating, which is highly useful in imparting functionality to magnetic nanoparticles as well as to improve their stability in aqueous dispersions [129]. Lin *et al* synthesized core/shell structured Fe/Au nanoparticles by a reverse micelle approach [119]. The Au shell was used to protect the Fe core and provide further organic functionalization. Au coated magnetite nanoparticles (60 nm) were synthesized by the reduction of Au (III) onto the surface via iterative hydroxylamine seeding [130]. Magnetite nanoparticles were stabilized by oleic acid and gold seed nanoparticles were covalently attached, resulting gold nanoshells [131]. It is well-known that thiols ( $-\text{SH}$ ) have high affinity to the gold surface, this property can be used in biotechnology, e.g., for binding antigens in immunoassay [132].

#### **2.2.4.3 Polymer stabilizers**

Several approaches have been developed to coat iron oxide nanoparticles, including *in-situ* coatings and post-synthesis coatings. Coating magnetic nanoparticles with natural polymers such as carbohydrates and proteins are common [133-137]. Many natural

polymers are biocompatible and therefore suitable for coating nanoparticles in biomedical applications.

The most common coatings are dextran, carboxymethylated dextran, carboxydextran, starch, chitosan, polyacrylic acid, polyethylene glycol (PEG), polyvinyl alcohol (PVA) [23]. The most common natural or synthetic organic polymers shells are described in Table 2.1.

**Table 2.1** Some useful polymers to coat nanoparticles for biomedical applications [18].

<b>Polymers</b>	<b>Applications</b>
Polyethylene glycol (PEG)	Improves biocompatibility, blood circulation time and internalization efficiency
Dextran	Enhances circulation time, stabilizes colloidal solution
Polyvinylpyrrolidone (PVP)	Enhances circulation time, stabilizes colloidal solution
Fatty acids	Colloidal stability, functional carboxyl groups
Polyvinyl alcohol (PVA)	Prevents coagulation of monodisperse particles
Polyacrylic acid	Increases stability and biocompatibility, helps bioadhesion
Polypeptides	Useful in cell biology, e.g., cell targeting
Poly (D,L-lactide)	Biocompatible, low toxicity
Poly (N-isopropylacryl-amide) (PolyNIPAAm)	Thermosensitive drug delivery and cell separation
Chitosan	Natural hydrophilic and cationic linear polymer widely used as non-viral gene delivery system, biocompatible
Gelatin	Natural polymer used as gelling agent, hydrophilic emulsifier, biocompatible

- **Dextran**

Dextran is a polysaccharide polymer composed exclusively of R-D-glucopyranosyl units with varying degrees of chain length and branching. Dextran has been often used as a polymer coating mostly because of its biocompatibility [138]. The formation of

magnetite in the presence of dextran (M. Wt: 40,000) has been reported [139], dextran was functionalized with hydroxyl groups to allow for binding of amino groups of proteins. The same process was used for ferucarbotran and ferumoxylol with *in-situ* coating of carboxydextran and carboxymethyl dextran, respectively. An important factor in the choice of dextran is the favorable size of dextran chains, which enables optimum polar interactions (mainly chelation and hydrogen bonding) with iron oxide surfaces. Although single hydrogen bonds are relatively weak, the total bonding energy of hydrogen bonds over the length of a polysaccharide molecule can be very high because of the large number of hydroxyl groups per molecule [140]. Bautista *et al* described dextran surface modification of pure superparamagnetic iron oxide nanoparticles prepared by laser pyrolysis and co-precipitation methods [141].

- **Polyethylene glycol (PEG)**

PEG is a hydrophilic, water-soluble, biocompatible polymer. Several investigations have reported the use of PEG to increase biocompatibility of iron oxide dispersions and blood circulation times [142-145]. Superparamagnetic iron oxide nanoparticles coated with polymerized polyethylene glycolylated bilayers were prepared [146]. Kumagai *et al* reported a simple route to synthesize PEG-coated iron oxide nanoparticles by hydrolysis of  $\text{FeCl}_3 \cdot 6\text{H}_2\text{O}$  in water and the subsequent treatment with poly(ethylene glycol)-poly(aspartic acid) block copolymer [147]. The PEG-coated nanoparticles revealed excellent solubility and stability in aqueous solution as well as in physiological saline.

- **Polyvinyl alcohol (PVA)**

PVA is a hydrophilic, biocompatible polymer. PVA coating onto the particle surface prevents their agglomeration, ideally resulting in monodisperse particles [148, 149]. Lee

*et al* modified the surface of magnetite nanoparticles with PVA by precipitation of iron salts in PVA aqueous solution to form a stable dispersion [150]. Chastellain *et al* synthesized PVA coated iron oxide nanoparticles and demonstrated colloidal stability of the final polymer coated product [151]. The cytotoxicity and uptake of PVA coated iron oxide nanoparticles by human melanoma cells were determined for various iron/polymer mass ratios [65]. PVA is a synthetic polymer that can transform into a polymer gel, which is a type of macromolecular network [152].

- **Alginate**

Alginate is an electrolytic polysaccharide with several carboxyl groups, the  $\text{COO}^-$  of the alginate can interact with iron ions, the resulting electrostatic repulsion can make the superparamagnetic iron oxide nanoparticles (SPIONs)-alginate system stable. Several researchers have reported the preparation of iron oxide nanoparticles with alginate [153-155] : the standard chemical synthesis consists of three steps: (a) gelation of alginate and ferrous ions, (b) *in-situ* precipitation of ferrous hydroxide by the alkaline treatment of alginate and (c) oxidation of ferrous hydroxide with an oxidizing agent ( $\text{O}_2$  or  $\text{H}_2\text{O}_2$ ). Morales *et al* described the synthesis of magnetic iron oxide nanoparticles into alginate beads with controlled size and magnetic properties for drug delivery applications [156].

- **Chitosan**

Chitosan is an alkaline, nontoxic, hydrophilic, biocompatible and biodegradable polymer. The synthesis of magnetic nanoparticles encapsulated in chitosan is of great interest [157, 158]. Kim *et al* synthesized superparamagnetic iron oxide nanoparticles (SPIONs) by a sonochemical method and dispersed them in chitosan with oleic acid as a surfactant [159]. Microspheres composed of SPIONs and chitosan were reported as a novel MRI detectable

embolic material [160], the SPION-chitosan microspheres showed a strong enhancement of MRI contrast.

Other different polymers that have been used for coating of magnetic nanoparticles include poly-L-lactic acid (PLA) [161], polymethacrylic acid [162], polyvinylpyrrolidone (PVP) [163] and polyacrylic acid (PAA) [164].

## **2.3 Synthesis of magnetic nanoparticles**

Numerous chemical methods such as co-precipitation, microemulsion, sol-gel method, polyol method, hydrolysis and thermolysis of precursors can be used to synthesize magnetic nanoparticles for biomedical applications. The synthesis of superparamagnetic nanoparticles is a complex process because of their colloidal nature. The main chemical challenge consists of defining experimental conditions, leading to formation of monodisperse magnetic grains of suitable size. Another critical point is to select a reproducible process that can be industrialized without any complex purification procedures such as ultra-centrifugation, size exclusion chromatography, magnetic filtration or flow field gradient. Some common methods to prepare particles with homogeneous composition and narrow size distribution are discussed below.

### **2.3.1 Precipitation from solution**

There are many different synthesis methods for magnetic nanoparticles of uniform size and shape. For drug delivery applications, it is generally desired to synthesize magnetic nanoparticles having a narrow size distribution. The most common approach is solution chemistry, wet chemical routes are considered simpler, more tractable, and more efficient, with appreciable control over size and composition of the nanoparticles compared to physical methods such as gas phase deposition or electron beam lithography.

Uniform particles are usually prepared via homogeneous precipitation reactions [165]. Figure 2.3 shows a schematic diagram of the different mechanisms proposed to explain the formation of uniform particles. In homogeneous precipitation, first a single burst of nucleation occurs when the concentration of constituent species reaches critical supersaturation. These nuclei formed are allowed to grow uniformly by diffusion of solutes from the solution. To achieve monodispersity, these two stages must be separated and nucleation should be avoided during the period of growth. This is the classical model proposed by LaMer and Dinegar [166] to explain the mechanism of formation of sulfur colloids (curve I of Fig. 2.3). However, uniform particles have been obtained after multiple nucleation events via a self-sharpening growth process (Ostwald ripening, curve III of Fig. 2.3) [167]. In addition, uniform particles have also been obtained as a result of aggregation of much smaller subunits rather than continuous growth by diffusion (curve II of Fig. 2.3) [168-170]. An artificial separation between nucleation and growth processes may be achieved by seeding, in which foreign particles are introduced into the solution of monomers below the critical supersaturation [165].

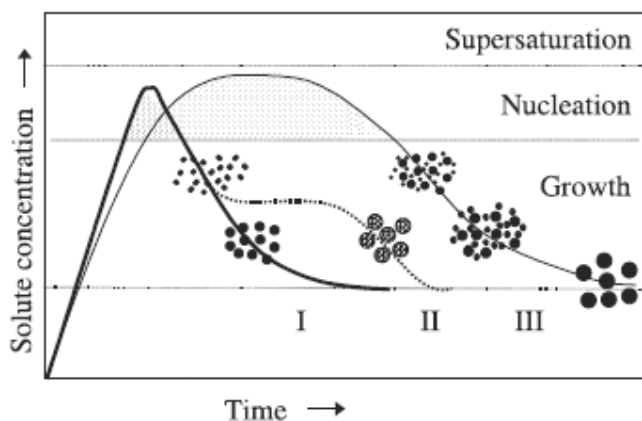
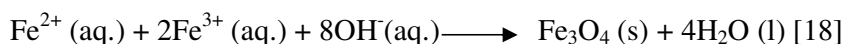


**Figure 2.3** Mechanism of formation of uniform particles in solution: curve I: single nucleation and uniform growth by diffusion (classical model of LaMer and Dinegar);

curve II: nucleation, growth and aggregation of smaller subunits; curve III: multiple nucleation events and Ostwald ripening growth [171].

The most important solution based synthesis methods to prepare magnetic nanomaterials include co-precipitation, reverse micelle, polyol process and decomposition of organic precursors.

**Coprecipitation:** Spherical iron oxide particles with narrow size distribution can be synthesized by the co-precipitation of  $\text{Fe}^{2+}$  and  $\text{Fe}^{3+}$  aqueous salt solutions by adding a base [172]. The control of size, shape and composition of particles depends on the type of salts used (chlorides, sulphates, nitrates, etc.),  $\text{Fe}^{2+}$  and  $\text{Fe}^{3+}$  ratio, temperature, reaction time, pH, and ionic strength (electrolyte concentration) of the media [173]. The conventional reaction for the preparation of magnetite can be written as follows:



Complete precipitation of magnetite between pH 9 and 14 is expected if the molar ratio of  $\text{Fe}^{2+} : \text{Fe}^{3+}$  is 1 : 2. The reaction should be carried out in a non-oxidizing environment to avoid the oxidation of  $\text{Fe}_3\text{O}_4$  to  $\text{Fe}_2\text{O}_3$ . The nanoparticles are generally coated with organic or inorganic molecules during the precipitation process to prevent oxidation and agglomeration. For example, dextran can be coated by shaking the aqueous suspension of the magnetic nanoparticles in 1% dextran for a few hours [174]. The synthesis of nanosized iron oxide in the presence of dextran renders the magnetic nanoparticles biocompatible and makes this method especially appropriate for *in-vivo* applications.

**Reverse micelle:** Micelle formation is a phenomenon of surfactant chemistry. Surfactants have a hydrophilic head and a long hydrophobic tail [175]. Reverse micelle solutions are

clear, isotropic liquid mixtures of oil, water and surfactants, which are rendered thermodynamically stable by the presence of a surfactant. In this system, surfactant molecules are dispersed in a continuous oil phase and microdroplets of aqueous phase are trapped within assemblies of surfactants. The surfactant stabilized microcavities (10 nm) provide a confinement effect, which limits particle nucleation, growth, and agglomeration [176]. This technique is a versatile and simple method to prepare nanosized particles, which are useful for both *in-vivo* and *in-vitro* applications [177-182]. Magnetic particles with average sizes of 4-12 nm were synthesized using microemulsions of ferrous dodecyl sulphate, the particle size could be controlled by the surfactant concentration and temperature [183]. Ultrafine magnetite nanoparticles (4 nm) were prepared by the reaction of aqueous  $\text{FeCl}_2$  and  $\text{FeCl}_3$  solutions with ammonium hydroxide within reverse micelle nanocavities using AOT as surfactant and heptane as the oil phase [184]. Carpenter *et al* [185] prepared metallic iron particles coated with a thin layer of gold by the reverse micelle reaction using cetyltrimethylammonium bromide (CTAB) as the surfactant, octane as the oil phase, and aqueous reactants of iron salts and sodium borohydride. The sequential synthesis by reverse micelles is utilized to prepare an iron core by the reduction of ferrous sulphate with sodium borohydride, the shell layer is then formed using an aqueous hydrogen tetrachloroaurate solution in the presence of excess sodium borohydride. The particle size can be controlled by the micelle size.

**Polyols:** Liquid polyol is used as a solvent of metallic precursor, reducing agent and in some cases as a complexing agent for the metallic cations [165]. The reaction involves reducing metallic salts directly to metals by a polyol. The solution of metal precursors in polyol is stirred and heated at a fixed temperature. Metal particles with well-defined shape and size can be obtained by controlling the precipitation kinetics. This method was first employed to synthesize noble metals such as Ru, Pd, Pt, Au, and other metals such as

Co, Ni or Cu [186, 187]. Iron particles (100 nm) can be prepared by the disproportionation reaction of ferrous hydroxide in organic media [187].  $\text{FeCl}_2$  and NaOH react in ethylene glycol (EG) or polyethylene glycol (PEG), the precipitation occurs at temperature of 80–100°C. Iron alloys can also be prepared by co-precipitation of Fe, Ni, and/or Co in EG and PEG [188, 189].

**High-temperature decomposition of organic precursors:** The decomposition of iron precursors at high temperatures results in magnetic iron oxide nanoparticles with a narrow size distribution and crystallinity, e.g., Alivisatos *et al* synthesized nanocrystals (4–10 nm) of maghemite by adding solutions of  $\text{FeCup}_3$  (Cup: *N*-nitrosophenylhydroxylamine) in octylamine into long chain amines at 250–300°C [190]. Hyeon *et al* synthesized monodisperse maghemite nanoparticles (13 nm) by addition of  $\text{Fe}(\text{CO})_5$  to a mixed solution of surfactant and oxidant (trimethylamine oxide) [191]. Sun *et al* prepared monodispersed magnetite nanoparticles (3–20 nm) by high-temperature (265°C) decomposition of iron (III) acetylacetonate in phenyl ether in the presence of alcohol, oleic acid, and oleylamine [192].

**Other solution techniques:** Ferritin consists of a central core of hydrated iron (III) oxide encapsulated with a protein shell [193]. Mann *et al* reported the synthesis of magnetite/maghemite nanoparticles (6–7 nm) by oxidation of ferritin with trimethylamino-*N*-oxide [194]. Another method is the use of dendrimers as templating hosts for the production of iron ferrite nanoparticles [195]. Carboxylated polyamidoamine PAMAM dendrimers (generation 4.5) were utilized for the synthesis and stabilization of ferrimagnetic iron oxide nanoparticles. Other solution techniques for the preparation of magnetite and maghemite nanoparticles include sonochemical-assisted synthesis [196–198] and electrochemical methods [199].

---

### 2.3.2 Chemical vapour condensation (CVC)

Spray pyrolysis and laser pyrolysis have been employed to synthesize large quantities of homogeneous magnetic nanoparticles. These methods allow for continuous operation.

**Spray pyrolysis:** In spray pyrolysis, a metal precursor solution is fed into a rotating furnace through a nozzle. The solvent evaporates and the metal precursor decomposes to metal oxide powders [200]. This method is useful to prepare uniformly dispersed particles with well-defined shape and size. It was reported that  $\text{Fe}^{3+}$  is partially reduced to a mixture of  $\text{Fe}^{2+}$  and  $\text{Fe}^{3+}$  in the presence of organic reducing agents resulting in the formation of magnetite, which is oxidized to maghemite. [201].

**Laser pyrolysis:** In this process, a carbon dioxide laser is used to heat up a mixture of gases, which initiates the chemical reaction. Pure, crystalline  $\gamma\text{-Fe}_2\text{O}_3$  nanoparticles (5 nm) with narrow size distribution have been prepared using  $\text{Fe}(\text{CO})_5$  (iron pentacarbonyl) as a precursor together with ethylene [202]. As  $\text{Fe}(\text{CO})_5$  does not absorb the laser radiation, ethylene is used to absorb the radiation and heat the iron pentacarbonyl, which is decomposed to iron oxide.

## 2.4 Magnetic composites

Magnetic composites consisting of superparamagnetic nanoparticles dispersed in diamagnetic matrices are used for *in-vivo* applications. The diamagnetic matrices provide functionality and biocompatibility. The synthesis procedures of superparamagnetic composites are as follows:

---

### 2.4.1 Magnetic nanoparticles encapsulated in polymer matrices

Encapsulation of magnetic particles in polymers results in enhanced compatibility with biological entities compared to bare particles [203]. The coating also reduces susceptibility to leaching and protects particle surfaces from oxidation. Therefore, encapsulation improves dispersibility, chemical stability and reduced toxicity [204].

Polymer coated magnetite nanoparticles were synthesized by seed precipitation polymerization of methacrylic acid and hydroxyethyl methacrylate in the presence of the magnetite nanoparticles [205]. Sometimes cross-linking of polymers is used to encapsulate magnetic nanoparticles. When magnetite is dispersed in aqueous albumin [206], or chitosan [207], or PVA [208], and a cross-linker is added, a polydispersed magnetic latex (0.3 microns) with 24 wt% magnetite content is formed [206]. Reverse emulsion polymerization technique can also be used for the preparation of superparamagnetic latex [209]. In this process, a ‘double-hydrophilic’ diblock copolymer is used to precipitate magnetic iron oxide. This diblock copolymer sterically stabilizes superparamagnetic iron oxide. An inverse emulsion, comprising of magnetic particles and monomer in decane with a little concentration of diblock copolymer, is ultrasonicated and magnetic latex is formed after subsequent polymerization. Superparamagnetic magnetite core and polymeric shell in a inverse microemulsion was synthesized by Chu *et al* [210]. The copolymerization of methacrylic acid, hydroxyethyl methacrylate and cross-linker in microemulsion resulted a stable hydrophilic polymeric shell around the magnetic nanoparticles. The particle size is governed by the monomer concentration and water/surfactant ratio.

---

### 2.4.2 Magnetic nanoparticles encapsulated in inorganic matrices

Superparamagnetic composites in inorganic matrices, e.g., silica as dispersion media, have been reported [181, 211, 212]. The advantage of using silica is that the presence of surface silanol groups reacts with alcohols and silane coupling agents to produce dispersions that are stable in non-aqueous solvents [213]. In addition, the silica surface provides stability in suspensions even with a high volume fraction of particles [214].

Silica coated  $\gamma$ -Fe<sub>2</sub>O<sub>3</sub> hollow spherical particles (150 nm) were synthesized by the aerosol pyrolysis of methanol solutions containing iron ammonium citrate and tetraethoxysilane (TEOS) [215]. Rapid evaporation of methanol favours the surface precipitation of iron oxide [200]. The low solubility of iron ammonium citrate in methanol compared to TEOS promotes the initial precipitation of the iron salt solid shell. The continuous shrinkage of this iron salt solid shell facilitates enrichment of the silicon oxide precursor (TEOS) at the surface. The thermal decomposition of the precursor results in the formation of silica coated  $\gamma$ -Fe<sub>2</sub>O<sub>3</sub> hollow spheres. The reverse micelle method has also been used for the synthesis of silica coated iron oxide nanoparticles [216]. Non-ionic surfactants (Triton X-100, Igepal CO-520 and Brij-97) were used to form microemulsions in which superparamagnetic iron oxide nanoparticles were formed by the co-precipitation reaction of ferrous and ferric ions with inorganic bases (NaOH or NH<sub>4</sub>OH).

### 2.5 Innovative aspects of the current work

From the literature survey, it is evident that the potential application of magnetic nanoparticles in cancer therapy is enormous. Although there is a significant progress in the development of different magnetic drug carrier systems, so far studies of the conditions under which magnetic targeting is feasible have been mostly empirical. Hence,

the current work was undertaken with the aim of synthesis, characterization and property evaluation of MCP with an experimental and modelling study of the efficacy with which these particles can be retained in the tumor.

1. Most of the prior work on gold coated iron (Fe@Au) nanoparticles mainly focused on structural, optical, photothermal and magnetic properties, no drug loading and release studies were conducted. In this work, the anti-cancer drug DOX was attached to Fe@Au nanoparticles. The binding of DOX with the gold coating was studied, which was due to the interaction of amine ( $-\text{NH}_2$ ) group of DOX with the Au shell. DOX loading and release profiles of Fe@Au nanoparticles were also studied. Up to 94% of DOX was loaded and 25% of adsorbed DOX was released.
2. Previous work on gold coated magnetic nanoparticles was focused on the thermotherapy application due to photothermal effect of gold [217-219]. However, their magnetic drug targeting application was not studied. The current work addressed this topic, for the first time the *in-vitro* targeting of Fe@Au nanoparticles at flow rates of the fluid comparable to that encountered in the capillary bed of tumor was studied in this work, 86% of Fe@Au nanoparticles was captured at a field gradient of  $25 \text{ T m}^{-1}$  and flow rate of  $1 \text{ mm s}^{-1}$ .
3. Prior work on PVA coated iron oxide nanoparticles was concentrated mostly on synthesis, characterization and functionalization studies [150, 151, 220]. Combined drug loading, drug release and *in-vitro* drug targeting of this system was not studied. The current work investigated the drug loading and release of DOX for different PVA coated iron oxide nanoparticles as well as *in-vitro* experimental targeting of this carrier system to study its feasibility to be used in magnetically targeted drug delivery. A maximum of 45% of adsorbed drug was released from PVA-IO nanoparticles and

---

90% of these MCP were captured at a field gradient of  $25 \text{ T m}^{-1}$  and flow rate of  $1 \text{ mm s}^{-1}$ .

4. There is insufficient work on combined modelling and experimental magnetic drug targeting [20, 22, 38]. The capture of MCP inside the blood vessel was modelled, which showed that  $\text{Fe}_3\text{O}_4$ ,  $\text{Fe@Au}$ , PVA-IO of 100 nm size can be targeted to breast tumors and other skin tumors located in the hand, leg and neck by a typical permanent magnet. In order to target tumors situated deep inside the body, MCP with higher saturation magnetization, such as Fe and FeCo, or an external magnet with higher magnetic field gradient ( $100 \text{ T m}^{-1}$ ) must be chosen. MCP deposition inside the blood vessel was also studied by simulating a time dependent CFD model, which showed that for a given magnetic field strength and vessel diameter, efficient MCP deposition was possible only for a certain window of flow rate. The simulations also showed that the ferrofluid creeps along the bottom wall under the influence of magnetic field, which can cause friction to the attached drug; therefore, drug injection should be as close as possible to the tumor site.

---

## Chapter 3

### Experimental Procedures and Model Development

This chapter describes the experimental procedures for the synthesis, characterization, property evaluation of uncoated as well as gold coated iron (Fe@Au) and PVA coated iron oxide (PVA-IO) MCP used in the current work. *In-vitro* drug loading, drug release and magnetic drug targeting procedures are also described. A model is presented to predict the transport and capture of MCP by an external magnet.

#### 3.1 Synthesis of gold coated iron (Fe@Au) MCP

Fe@Au nanoparticles were synthesized by the reverse micelle technique. Reagents used for the synthesis of Fe@Au nanoparticles were cetyltrimethylammonium bromide (CTAB) ( $C_{19}H_{42}BrN$ , Acros Organics), iron (II) sulphate heptahydrate ( $FeSO_4 \cdot 7H_2O$ , Fischer Chemicals), hydrogen tetrachloroaurate ( $HAuCl_4$ ), sodium borohydride ( $NaBH_4$ , Fluka Chemical), octane ( $C_8H_{18}$ , Aldrich) and n-butanol ( $C_4H_{10}O$ , Aldrich). In this reaction, CTAB was used as surfactant, n-butanol as co-surfactant and octane as oil phase.

The synthesis reaction was performed in an oxygen free glove box in two steps, in each step predetermined amount of aqueous reactants were mixed with CTAB, n-butanol and octane to form the reverse micelle solution. The procedure and the quantity of components used for the synthesis are schematically presented in Fig. 3.1.

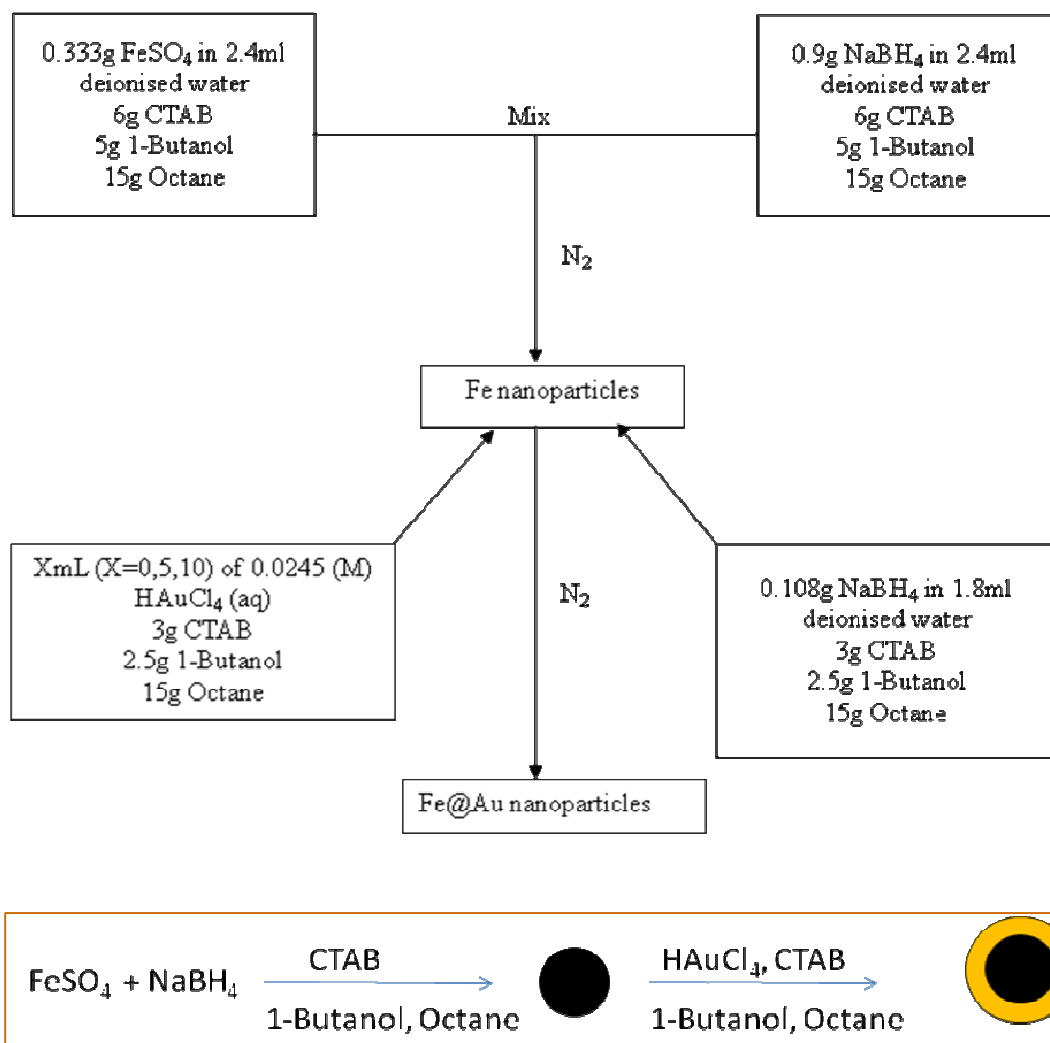


**Figure 3.1** Schematic diagram showing a typical procedure for formation of Fe@Au MCP by the reverse micelle technique.  $\text{FeSO}_4$  and  $\text{HAuCl}_4$  are reduced by  $\text{NaBH}_4$ , CTAB is surfactant, 1-butanol is co-surfactant and octane is oil phase.

In a typical experiment, 0.333 g  $\text{FeSO}_4$  was dissolved in 2.4 ml deionised water in a beaker and 6 g CTAB, 5 g 1-butanol and 15 g octane were added to it. In another beaker, 0.9 g  $\text{NaBH}_4$  was dissolved in 2.4 ml water and mixed with 6 g CTAB, 5 g 1-butanol and 15 g octane. Micellar solutions containing  $\text{FeSO}_4$  and  $\text{NaBH}_4$  were mixed together under stirring, color change from pale green to black was observed.  $\text{NaBH}_4$  reduces  $\text{FeSO}_4$  resulting in the formation of iron core. Once the iron nanoparticles formed, a micellar solution containing 0.0245 (M)  $\text{HAuCl}_4$  (aq), 3 g CTAB, 2.5 g 1-butanol and 15 g octane was added followed by the addition of a micellar solution of  $\text{NaBH}_4$  (aq). Au (III) is reduced to Au (0) by  $\text{NaBH}_4$  and gold forms a coating on the outer surface of the iron particles [74]. The volume of  $\text{HAuCl}_4$  was varied to alter the thickness of gold coating. The synthesized nanoparticles were washed with 1:1 methanol/water mixture and dried under vacuum and stored, the resulting powder was black. Following the above synthesis procedure, three sample sets were prepared by varying the concentration of gold (Table 3.1). Increasing the gold concentration beyond the range studied in this work resulted in very low saturation magnetization ( $M_s$ ), hence they were not examined further.

**Table 3.1** Summary of sample sets synthesized by the reverse micelle technique.

Sample set	S-1	S-2	S-3
mmol of Au/ mmol of Fe	0	0.102	0.204

### 3.2 Synthesis of PVA coated iron oxide (PVA-IO) MCP

PVA-IO nanoparticles were synthesized by co-precipitation of iron oxide at high pH, followed by coating with PVA solution. Chemicals used for the synthesis of PVA-IO

nanoparticles were ferrous chloride tetrahydrate ( $\text{FeCl}_2 \cdot 4\text{H}_2\text{O}$ , Aldrich), ferric chloride hexahydrate ( $\text{FeCl}_3 \cdot 6\text{H}_2\text{O}$ , Aldrich), sodium hydroxide ( $\text{NaOH}$ , Merck Inc.) and polyvinyl alcohol (PVA, Fluka) with average molecular weight of 31000-50000 (99% degree of hydrolysis). A mixed solution of ferrous and ferric ions (molar ratio 1:2) was prepared by dissolving 0.15 mol  $\text{FeCl}_2 \cdot 4\text{H}_2\text{O}$  and 0.3 mol  $\text{FeCl}_3 \cdot 6\text{H}_2\text{O}$  in 30 mL water. Black iron oxide was precipitated by adding mixed solution of ferrous and ferric ions drop by drop to 100 mL of 0.4 M  $\text{NaOH}$  solution ( $\text{pH}=13$ ) while stirring at 600 rpm with an impeller and purging with  $\text{N}_2$ . The mixture was continuously purged by  $\text{N}_2$  for 20 minutes. Precipitates were separated from the supernatant liquid by centrifugation. The precipitates were washed with deionized water (purged with  $\text{N}_2$ ) by ultrasonication and then separated by centrifugation at 5000 rpm.

For coating of iron oxide nanoparticles, aqueous PVA solutions were prepared by dissolving dry PVA powder in deionized water at  $55^\circ\text{C}$ . Iron oxide nanoparticles were added and mixed with PVA solution by stirring with an impeller for 12 hours. PVA-IO were separated by the use of a permanent magnet and dried in a vacuum oven for characterization. Following the above synthesis procedure, 5 sets of samples were prepared by varying the concentration of PVA (Table 3.2).

**Table 3.2** Summary of sample sets synthesized by the co-precipitation technique.

Sample set	S-4	S-5	S-6	S-7	S-8
PVA concentration (wt%)	0	0.5	1	2	5

---

### 3.3 Characterization and *in-vitro* tests

The synthesized Fe@Au and PVA-IO nanoparticles were characterized by transmission electron microscopy (TEM), X-ray diffraction (XRD), vibrating sample magnetometry (VSM), dynamic light scattering (DLS), X-ray photoelectron spectroscopy (XPS), thermal gravimetric analysis (TGA) and Fourier transform infrared (FTIR) spectroscopy. *In-vitro* targeting of these MCP, their drug loading and release studies were carried out.

#### 3.3.1 Transmission electron microscopy

The size and morphological characterization of individual nanoparticles were performed using a JEOL 2010 transmission electron microscope (TEM) operating at 200 kV. TEM samples were prepared by dispersing nanoparticles in acetone for 30 min by ultrasonic vibration. The dilute suspension was dropped on a carbon coated copper grid and dried in vacuum.

#### 3.3.2 X-ray diffraction

X-ray diffraction (XRD) measurements were performed on dry powder using a Shimadzu XRD-6000 X-ray diffractometer with Cu-K $\alpha$  radiation (wavelength = 0.154 nm). The powder was packed in a glass sample holder and the XRD patterns were collected in the  $2\theta$  range of 10° to 90° with a step size of 0.02°. Phase identification was carried out by matching peak positions and relative intensities to reference JCPDS files. The Rietveld refinement of the XRD pattern was conducted using TOPAS (version 4.1) software.

### **3.3.3 Magnetic measurements**

A LakeShore 7404 vibrating sample magnetometer was used to measure the magnetic properties of the synthesized nanoparticles at room temperature in an applied magnetic field range of 0 to 10 kOe.

### **3.3.4 Dynamic light scattering**

Dynamic light scattering was used to measure the hydrodynamic diameters of aggregates of magnetic nanoparticles in PBS. Dilute suspensions ( $< 0.2 \text{ mg.ml}^{-1}$ ) were taken in quartz cuvettes and investigated using a Malvern Instruments Zetasizer Nano DLS unit. The samples were equilibrated for 5 min before each measurement.

### **3.3.5 X-ray photoelectron spectroscopy**

X-ray photoelectron spectra were recorded using the Kratos Ultra system with a monochromatic Al K $\alpha$  X-ray source operating at 15 kV and 10 mA. The sampling area on the specimen was typically about 700  $\mu\text{m}$  by 400  $\mu\text{m}$ . A step-scan interval of 1 eV was used for wide scans, and 0.1 eV for high-resolution scans with acquisition times of 60 sec for both resolutions.

### **3.3.6 Thermo gravimetric analysis**

Thermo gravimetric analysis was performed to determine the polymer content of PVA-IO nanoparticles. Powder sample was placed in a ceramic pan, heated to 600°C at a ramp rate of 10°C min $^{-1}$  under oxygen flow in TGA Q500 thermo gravimetric analyzer. The weight loss was measured as a function of temperature.

---

### 3.3.7 Fourier transform infrared spectra

Fourier transform infrared (FTIR) spectra were recorded by a Nicolet Magna-IR 550 spectrometer in the region of 4000-400  $\text{cm}^{-1}$  with 4  $\text{cm}^{-1}$  resolution. FTIR samples were prepared by mixing and grinding nanoparticles with KBr powder followed by pelletizing.

### 3.3.8 Doxorubicin (DOX) drug loading and release

The water-soluble anti-cancer drug DOX was chosen as a model drug for drug loading and release study. The DOX loading was carried out by dispersing 5 mg of Fe@Au / PVA-IO nanoparticles in 5 mL aqueous DOX solution (drug concentration = 0.1 mg/mL) following the experimental procedure described by Kuznetsov *et al* [221]. The suspension of coated magnetic nanoparticles in DOX solution was shaken in a rotary shaker (200 rpm) for 26 h to facilitate DOX uptake. At different time intervals, the magnetic nanoparticles were removed from DOX solution using a permanent magnet and the optical density of particle free DOX solution was measured at 498 nm by a UV-vis spectrophotometer [222]. After the measurements, magnetic nanoparticles were redispersed for further DOX loading. Beyond a certain time, there was no concentration change of DOX in the solution since the loading capacity of the particles had reached the saturation. The drug loading capacity was determined as the difference between the initial DOX concentration and the DOX concentration left in the supernatant. The drug loaded magnetic nanoparticles were then magnetically separated and dried in the vacuum oven. The drug release test was performed by dispersing the dried drug loaded nanoparticles in 5 mL PBS buffer at 37°C. The released concentration of DOX was measured at fixed time intervals by UV-vis spectrophotometry at 498 nm.

### 3.3.9 *In-vitro* targeting of MCP

*In-vitro* tests for targeting of MCP were conducted to determine the retention of MCP under various flow rates of fluid with different magnetic field gradients. An *in-vitro* apparatus (Fig. 3.2) simulating the human circulatory system was constructed.

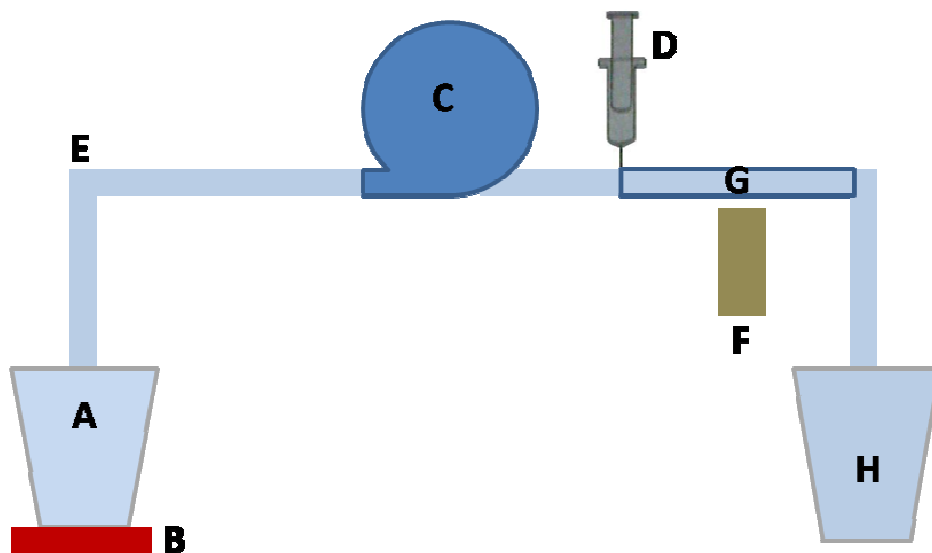


**Figure 3.2** Schematic of an *in-vitro* experiment simulating the human circulatory system; A: intake beaker, B: vibrating plate, C: pump, D: syringe, E: silicone tube, F: permanent magnet, H: outlet beaker, G: region of targeting.

PBS buffer (simulating blood) in beaker (A) was pumped through a tube (E) of inner diameter of 1 mm into a beaker (H) by a pump (C). The flow rate of fluid can be changed by adjusting the pump. The ferrofluid containing suspension of MCP ( $0.33 \text{ mg cc}^{-1}$ ) was injected at the intake (D). A permanent magnet (F) was placed near the target region (G) and the magnetic field was varied by adjusting the vertical position of the magnet from the tube. The mass of particles deposited was determined from the difference between initial mass of the particles and the mass of the particles collected after each experiment.

The percentage retention of MCP was measured by the ratio of the deposited mass of MCP relative to the initial mass.

### 3.4 Model development

The cylindrical tube employed in the *in-vitro* experiments is assumed to be a two-dimensional (2-D) rectangular channel (Fig. 3.3). In this figure,  $x$ - and  $y$ - denote the horizontal and vertical coordinates. The magnet is placed midway along the  $x$ -axis.

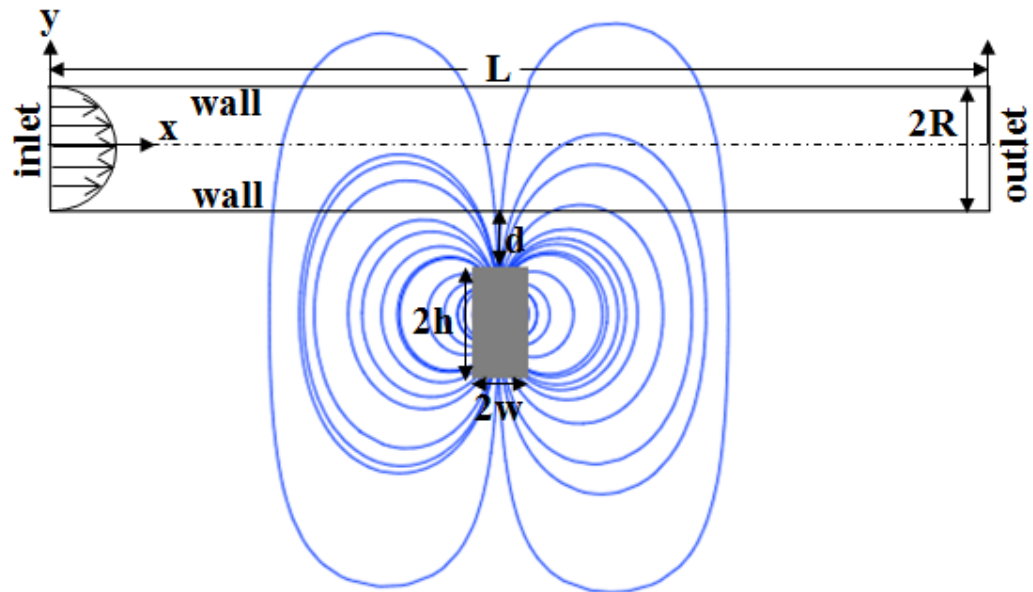


**Figure 3.3** The 2-D rectangular channel mimicking a cylindrical tube and frame of reference for analysis.

There are several forces acting on a particle in a streaming fluid:

- 
- Hydrodynamic force ( $\mathbf{F}_f$ ): This force is generated by the pressure difference due to the heartbeat. This force creates a velocity field and defines the flow speed of the carriers in fluid.
  - Magnetic force ( $\mathbf{F}_{mag}$ ): This force is due to an external magnetic field, which accelerates MCP perpendicular to the flow direction.
  - Inertia forces: Normally the inertia forces are several orders of magnitude smaller than the accelerating force and hence neglected.
  - Gravitational and buoyancy forces: These forces are negligible for monodisperse suspensions with a particle diameter smaller than 1  $\mu\text{m}$ .

Therefore, the transport of MCP is predicted by balancing the dominant magnetic and fluidic forces as [97],

$$\mathbf{F}_{mag} + \mathbf{F}_f = 0 \quad (3.1)$$

The magnetic force acting on a particle is determined from the following expression [103]:

$$\mathbf{F}_{mag} = VM_p \nabla B = 0.5\mu_0\chi V \nabla H^2 \quad (3.2)$$

Here,  $\mu_0$  is the magnetic permeability of free space,  $V$  is the volume of MCP,  $\chi$  is the magnetic susceptibility of MCP,  $H$  and  $B$  are the magnetic field strength and gradient of the magnet.

The fluidic force is predicted using Stokes' approximation for the drag on a sphere in a laminar flow field [223]

$$\mathbf{F}_f = -6\pi\eta R_p (\mathbf{v}_p - \mathbf{v}_f) \quad (3.3)$$

Here,  $R_p$  is the hydrodynamic size of MCP,  $\mathbf{v}_p$  is the velocity of MCP,  $\eta$  and  $\mathbf{v}_f$  are the viscosity and flow rate of fluid, respectively.

### 3.4.1 Magnetic field

The magnetic field strength can be decomposed into components as,

$$\mathbf{H}(x, y) = H_x(x, y)\vec{\mathbf{x}} + H_y(x, y)\vec{\mathbf{y}} \quad (3.4)$$

The analytical expressions obtained for the  $x$ - and  $y$ -component of the magnetic field strength for rectangular magnet can be expressed as follows [224]:

$$H_x(x, y) = \frac{M_s}{4\pi} \left[ \ln \left( \frac{(x+w)^2 + (y+d+R)^2}{(x+w)^2 + (y+d+R+2h)^2} \right) - \ln \left( \frac{(x-w)^2 + (y+d+R)^2}{(x-w)^2 + (y+d+R+2h)^2} \right) \right] \quad (3.5)$$

$$H_y(x, y) = \frac{M_s}{2\pi} \left[ \tan^{-1} \left( \frac{2h(x+w)}{(x+w)^2 + (y+d+R+h)^2 - h^2} \right) - \tan^{-1} \left( \frac{2h(x-w)}{(x-w)^2 + (y+d+R+h)^2 - h^2} \right) \right] \quad (3.6)$$

Here the width and the height of the rectangular magnet are  $2w$  and height  $2h$ , respectively;  $d$  is the distance between the surface of the magnet and the bottom wall of tube,  $R$  is the half-width of the channel (Fig. 3.3).

The analytical expressions for the  $x$ - and  $y$ -component of the magnetic field strength for a cylindrical magnet having radius  $R_{mag}$  is expressed as [97]:

$$H_x(x, y) = \frac{M_s R_{mag}^2}{2} \left( \frac{2(y + d + R_{mag} + R)x}{[(y + d + R_{mag} + R)^2 + x^2]^2} \right) \quad (3.7)$$

$$H_y(x, y) = \frac{M_s R_{mag}^2}{2} \left( \frac{(y + d + R_{mag} + R)^2 - x^2}{[(y + d + R_{mag} + R)^2 + x^2]^2} \right) \quad (3.8)$$

### 3.4.2 Flow velocity

The nature of the flow, whether laminar or turbulent, is determined by Reynolds number (Re);  $Re = v_f D \rho / \eta$ , where  $D$  is the diameter of the vessel,  $\rho$  and  $\eta$  are the density and viscosity of the fluid, respectively. For a dilute particle suspension (0.33 mg/cc) in a fluid and a given vessel diameter, this Reynolds number is dependent on flow rate of fluid. In the flow regime (up to 40 mm/s) studied in this work, the Reynolds number is 33 (i.e.  $Re < 1100$ ). Therefore, the flow was assumed to be fully developed laminar flow. Based on these assumptions, the fluid velocity is given by

$$v_x = 2\bar{v} \left( 1 - (x/R)^2 \right) \quad (3.9)$$

where  $\bar{v}$  is the average velocity of fluid and  $R$  is the radius of the vessel.

The fluidic force components are

$$F_{fx} = -6\pi\eta R_p v_x \quad (3.10)$$

and

$$F_{fy} = -6\pi\eta R_p v_y \quad (3.11)$$

The viscosity of blood plasma ( $\eta = 1.2 \times 10^{-3} \text{ N.s.m}^{-2}$ ) was used in Eqns. 3.10 and 3.11 [225].

### 3.4.3 Equation of motion

The equation of motion of MCP in the vessel can be written by balancing the magnetic and fluidic forces in component form as,

$$F_{magx} = F_{fx} \quad \text{and} \quad F_{magy} = F_{fy} \quad (3.12)$$

From Eqns. 3.5 and 3.6 we obtain,

$$B_x(x, y) = \frac{\mu_0 M_s}{4\pi} \left[ \ln \left( \frac{(x+w)^2 + (y+d+R)^2}{(x+w)^2 + (y+d+R+2h)^2} \right) - \ln \left( \frac{(x-w)^2 + (y+d+R)^2}{(x-w)^2 + (y+d+R+2h)^2} \right) \right] \quad (3.13)$$

$$B_y(x, y) = \frac{\mu_0 M_s}{2\pi} \left[ \tan^{-1} \left( \frac{2h(x+w)}{(x+w)^2 + (y+d+R+h)^2 - h^2} \right) - \tan^{-1} \left( \frac{2h(x-w)}{(x-w)^2 + (y+d+R+h)^2 - h^2} \right) \right] \quad (3.14)$$

From Eqns. 3.13 and 3.14 we get,

$$\begin{aligned} \frac{\partial B(x, y)}{\partial x} &= \frac{\mu_0 M_s}{4\pi \sqrt{0.25[\ln(a) - \ln(b)]^2 + [\tan^{-1}(c) - \tan^{-1}(d)]^2}} \\ &\times \left[ (\ln(a) - \ln(b))(e - f - g + q) + 4(\tan^{-1}(c) - \tan^{-1}(d))(m - n) \right] \end{aligned} \quad (3.15)$$

---


$$\frac{\partial B(x, y)}{\partial y} = \frac{\mu_0 M_s}{4\pi \sqrt{0.25[\ln(a) - \ln(b)]^2 + [\tan^{-1}(c) - \tan^{-1}(d)]^2}} \times \left[ (\ln(a) - \ln(b))(i - j - k + l) + 8(\tan^{-1}(c) - \tan^{-1}(d))(o - p) \right] \quad (3.16)$$

where,

$$a = \frac{(x+w)^2 + (y+d+R)^2}{(x+w)^2 + (y+d+R+2h)^2}, \quad b = \frac{(x-w)^2 + (y+d+R)^2}{(x-w)^2 + (y+d+R+2h)^2},$$

$$c = \frac{2h(x+w)}{(x+w)^2 + (y+d+R+h)^2 - h^2}, \quad d = \frac{2h(x-w)}{(x-w)^2 + (y+d+R+h)^2 - h^2},$$

$$e = \frac{(x+w)}{(x+w)^2 + (y+d+R)^2}, \quad f = \frac{(x+w)}{(x+w)^2 + (y+d+R+2h)^2},$$

$$g = \frac{(x-w)}{(x-w)^2 + (y+d+R)^2}, \quad q = \frac{(x-w)}{(x-w)^2 + (y+d+R+2h)^2},$$

$$i = \frac{(y+d+R)}{(x+w)^2 + (y+d+R)^2}, \quad j = \frac{(y+d+R)}{(x-w)^2 + (y+d+R)^2},$$

$$k = \frac{(y+d+R+2h)}{(x+w)^2 + (y+d+R+2h)^2}, \quad l = \frac{(y+d+R+2h)}{(x-w)^2 + (y+d+R+2h)^2},$$

$$\begin{aligned}
 m &= \frac{h \left( (y+d+R+h)^2 - (x+w)^2 - h^2 \right)}{\left( (x+w)^2 + (y+d+R+h)^2 - h^2 \right)^2 + 4h^2 (x+w)^2}, \\
 n &= \frac{h \left( (y+d+R+h)^2 - (x-w)^2 - h^2 \right)}{\left( (x-w)^2 + (y+d+R+h)^2 - h^2 \right)^2 + 4h^2 (x-w)^2}, \\
 o &= \frac{h (y+d+R+h) (x-w)}{\left( (x-w)^2 + (y+d+R+h)^2 - h^2 \right)^2 + 4h^2 (x-w)^2}, \\
 p &= \frac{h (y+d+R+h) (x+w)}{\left( (x+w)^2 + (y+d+R+h)^2 - h^2 \right)^2 + 4h^2 (x+w)^2}, \tag{3.17}
 \end{aligned}$$

The magnetic force can be decomposed into components as,

$$\mathbf{F}_{mag}(x, y) = F_{magx}(x, y) \vec{\mathbf{x}} + F_{magy}(x, y) \vec{\mathbf{y}} \tag{3.18}$$

where,

$$F_{magx} = VM_p \frac{\partial B}{\partial x} \quad \text{and} \quad F_{magy} = VM_p \frac{\partial B}{\partial y} \tag{3.19}$$

Combining Eqns. 3.10, 3.11, 3.12 and 3.19 we get,

$$\frac{dy}{dt} = \frac{2M_p R_p^2}{9\eta} \frac{\partial B}{\partial y} \tag{3.20}$$

and

---


$$\frac{dx}{dt} = \frac{2M_p R_p^2}{9\eta} \frac{\partial B}{\partial x} + 2\bar{v} \left(1 - (x/R)^2\right) \quad (3.21)$$

Eqns. 3.20 and 3.21 are solved numerically to predict the trajectory (x(t), y(t)) of the MCP.

### 3.5 CFD simulations

In the CFD simulations, the liquid is assumed to be Newtonian and incompressible, PBS buffer (a water based chloride, phosphate salt solution of Na and K) shows characteristics similar to water at room temperature and atmospheric pressure. Gravity is neglected owing to the small dimensions of nanoparticles and the overwhelming effect of the externally applied magnetic field. Low flow rate ensures Reynolds number in the laminar regime for the experiments and simulations. Thus the following Navier-Stokes equations of motion with the equation of continuity can describe the motion of the PBS buffer flowing inside the channel (Fig. 3.3):

$$\nabla \cdot \mathbf{v} = 0, \quad (3.22)$$

$$\frac{\partial \mathbf{v}}{\partial t} + \mathbf{v} \cdot \nabla \mathbf{v} = -\frac{1}{\rho} \nabla p + \nu \nabla^2 \mathbf{v} + \mathbf{F} \quad (3.23)$$

Here  $\mathbf{v}$ ,  $p$ ,  $\eta$ ,  $\rho$ ,  $\nu (= \eta / \rho)$  and  $\mathbf{F}$  denote the velocity vector, pressure, viscosity, density, kinematic viscosity and the external body force due to the applied magnetic field, respectively. The continuum approximation was assumed as sparse suspension of MCP can undergo continuous motion within the length and time scales of the flow. Therefore, the ferrofluid with MCP suspension can be modelled employing a multiple species balance equation across the control volume:

---


$$\frac{\partial}{\partial t}(\rho Y) + \nabla \cdot (\rho Y \mathbf{v}_p) = \nabla \cdot [D \nabla (\rho Y)] \quad (3.24)$$

Here  $Y$ ,  $\mathbf{v}_p$  and  $D$  are the mass fraction of MCP in ferrofluid, velocity of MCP and mass diffusivity, respectively. The equations of motion, the continuity equation and the species balance equation were solved employing the software ANSYS FLUENT<sup>TM</sup>. Mass and volume weighted mixing law was employed to calculate  $\eta$  and  $\rho$  of the mixture, a dilute-approximation with constant diffusion coefficient was employed for mass diffusivity constant ( $D$ ). The velocity of MCP ( $\mathbf{v}_{mag}$ ) due to magnetic field was obtained by balancing hydrodynamic drag forces and magnetic forces as  $\mathbf{v}_{mag} = \mathbf{F}_{mag} / 6\pi\eta R_p$ , where  $R_p$  is the size of MCP. The total velocity  $\mathbf{v}_p$  of MCP in the species balance (Eqn. 3.24) is  $\mathbf{v}_p = \mathbf{v} + \mathbf{v}_{mag}$  [103].

### 3.5.1 Boundary conditions

The walls in the geometries are considered to be no-slip and impermeable:

$$v_x = v_y = 0 \quad (3.25)$$

$$\frac{\partial p}{\partial z} = 0 \quad (3.26)$$

In the velocity inlet boundary condition, ANSYS FLUENT uses the velocity and scalar quantities to compute inlet mass flow rate. The mass flow rate entering a fluid cell adjacent to a velocity inlet boundary is computed as,

$$\dot{m} = \int \rho \vec{v} \cdot d\mathbf{A}. \quad (3.27)$$

The inlet flow was modelled as a fully developed parabolic profile  $\left[ v_x = 2\bar{v} \left( 1 - (x/R)^2 \right) \right]$  where the average velocity ( $\bar{v}$ ) was incorporated from the range of flow rates used in the experiments (1.5 mm. s<sup>-1</sup> to 40 mm. s<sup>-1</sup>). The typical inlet MCP concentration (0.33 mg cc<sup>-1</sup>) was also obtained from the experiments. At the channel exit, the ‘pressure outlet’ boundary condition was used in simulations.

### 3.5.2 Magnetic force field

The magnetic field imposed by the permanent magnet was modelled as a source term to the momentum equation. In this study, rectangular and cylindrical magnets were considered to study the influence of the magnet shape on the deposition of MCP. It was assumed that at any instant the magnetic force per unit volume is  $\mathbf{F} = n\mathbf{F}_{mag}$  where  $n$  is the number of MCP present per unit volume of PBS. The magnetic force ( $\mathbf{F}_{mag}$ ) acting on each particle was calculated from Eqn. 3.2.

### 3.5.3 Grid generation and solution methodology

In the pre-processing stage the grid was prepared using commercial software GAMBIT. The equations of motion, continuity equation and the species balance equation together with the boundary conditions were solved employing the commercial software ANSYS FLUENT<sup>TM</sup>. Fluent uses a control-volume based technique to convert the governing equations to algebraic equations, which are again solved numerically in time. This control volume technique consists of integrating the governing equations about each control volume, yielding discrete equations that conserve each quantity on a control-volume basis. The co-located scheme used by ANSYS FLUENT solver stores both pressure and velocity at cell centers. The default ‘standard’ interpolation scheme was used, which

interpolates the pressure values at the faces using momentum equation coefficients. The momentum and species equations were solved employing the ‘first order upwind’ discretization scheme. The unsteady solver was used for time marching over a period after ensuring a converged solution at each time step. The results obtained are grid independent.

## Chapter 4

### Results and Discussion

This chapter describes the results and discussion of the synthesis, characterization, *in-vitro* tests and modelling of MCP targeting. Comparison of the current work to selected reports from literature is also presented.

#### 4.1 Gold coated iron (Fe@Au) MCP system

Here structural, morphological and magnetic properties of Fe@Au nanoparticles are presented. The particles were characterized by XRD, TEM, XPS and VSM. DOX loading and release studies as well as *in-vitro* targeting of Fe@Au MCP under physiologically relevant flow speeds of fluid are also presented.

##### 4.1.1 Physical properties

Representative powder X-ray diffraction patterns of reverse micelle synthesized Fe@Au nanoparticles are presented in Fig. 4.1.

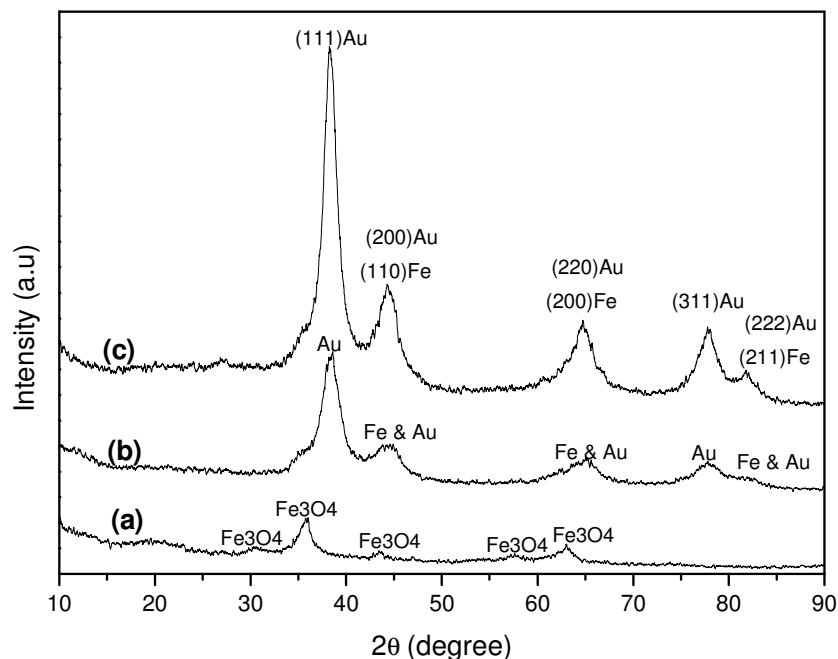


**Figure 4.1** X-ray diffraction pattern of (a) S-1 (uncoated), (b) S-2 (0.102 mmol gold coated iron nanoparticles) and (c) S-3 (0.204 mmol gold coated iron nanoparticles). The uncoated particles are oxidized to iron oxide whereas in gold coated particles, iron peaks overlap with gold peaks.

The X-ray diffraction pattern of S-1 shows peaks corresponding to the magnetite ( $\text{Fe}_3\text{O}_4$ ) phase. As there was no coating of gold in S-1, iron was oxidized to form iron oxide ( $\text{Fe}_3\text{O}_4$ ). For sample sets S-2 and S-3, peaks corresponding to gold were observed at  $2\theta = 38.1^\circ, 44.4^\circ, 64.6^\circ, 77.6^\circ$  and  $81.8^\circ$ . In sample sets S-2 and S-3, the peaks of  $\alpha$ -iron were overlapped with the peaks of gold at  $2\theta = 44.4^\circ, 64.6^\circ$  and  $81.8^\circ$ , consistent with previous reports [119, 226]. The Rietveld refinement of corresponding powder diffraction pattern was performed and it was found that 83 atomic % Fe, 17 atomic % Au and 49.5 atomic % Fe, 50.5 atomic % Au were present in S-2 and S-3, respectively. Figure 4.2 shows the selected area electron diffraction (SAED) pattern of S-3 obtained from transmission

electron microscopy. The diffraction rings were indexed and it was observed that gold 200, 220, 222 peaks overlapped with iron 110, 200, 211 peaks (Fig. 4.2).

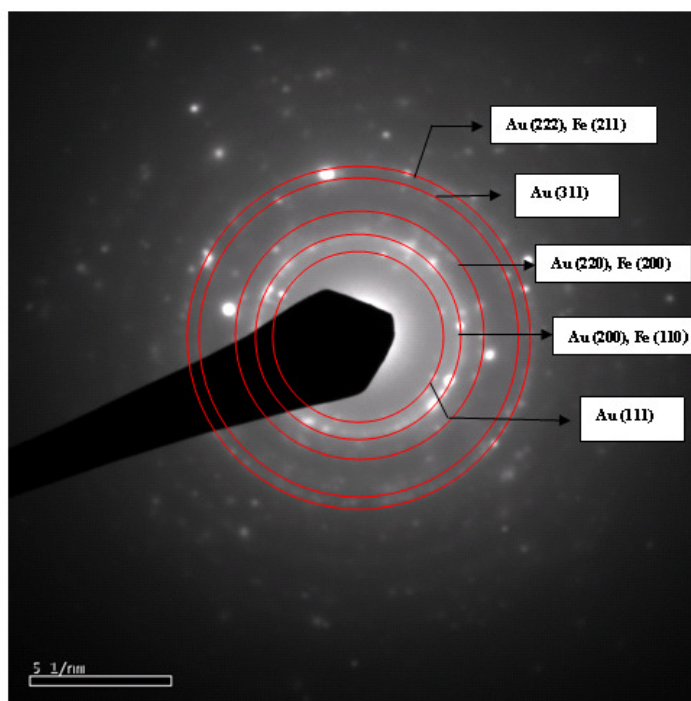


**Figure 4.2** Selected area electron diffraction (SAED) pattern of S-3 (0.204 mmol gold coated iron nanoparticles). Gold 200, 220, 222 diffraction peaks overlap with iron 110, 200, 211 peaks.

The EDX spectrum of S-3 generated with an electron nanoprobe (~20 nm in diameter) revealed both iron and gold peaks (Fig. 4.3). No oxygen peak was found, suggesting that there was negligible oxidation of iron. The peaks corresponding to carbon and copper were from the sample holder.

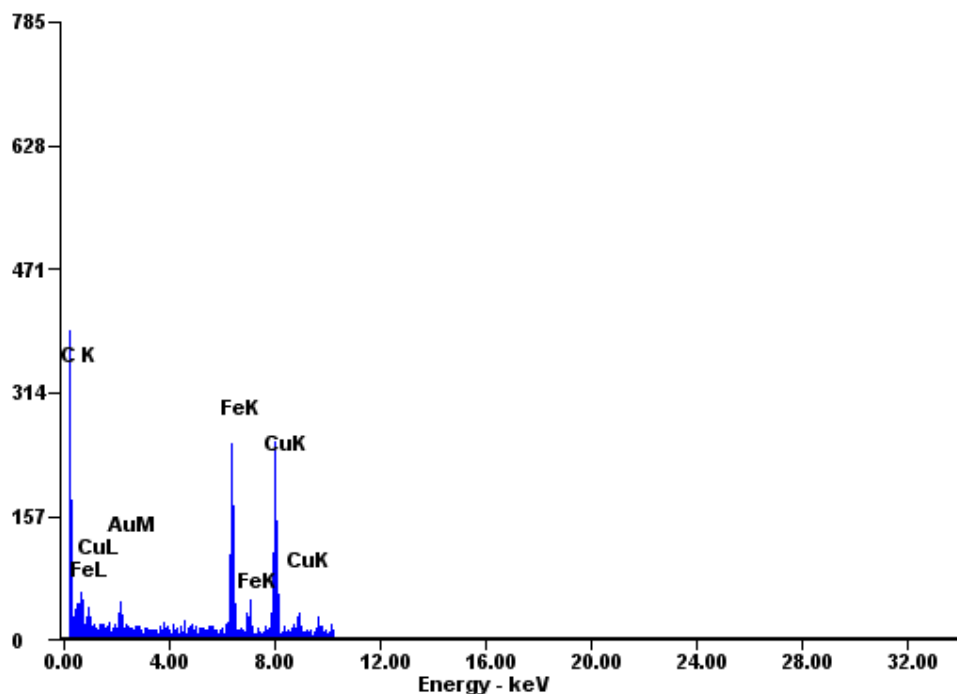


**Figure 4.3** EDX spectrum of S-3 (0.204 mmol gold coated iron nanoparticles). The absence of oxygen peak indicates that iron is not oxidized when coated with gold. The peaks of carbon and copper arise from the sample holder.

X-ray photoelectron spectroscopy (XPS) was used to study the surface composition of Fe@Au nanoparticles. Figure 4.4 shows the XPS spectra and peak fit of (a) Fe 2p and (b) Au 4f regions of Fe@Au nanoparticles (S-2 and S-3). The position of Fe 2p<sub>1/2</sub> line at 723.2 eV and that of Fe 2p<sub>3/2</sub> line at 710 eV (Figure 4.4.a) corresponded to

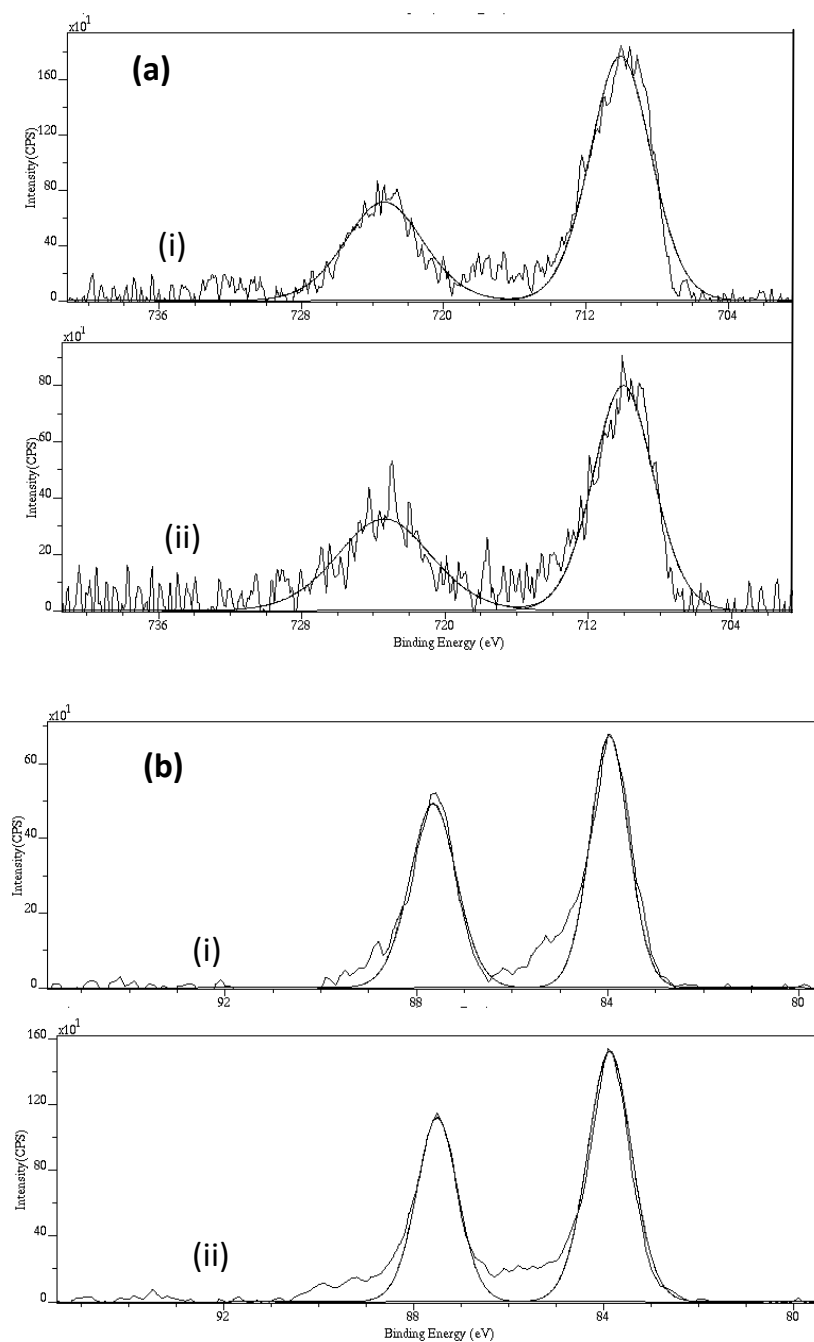


**Figure 4.4** XPS spectra and peak fit of the (a) Fe 2p and (b) Au 4f regions of (i) S-2 (0.102 mmol gold coated iron nanoparticles) and (ii) S-3 (0.204 mmol gold coated iron nanoparticles). The detection of Fe with Au coating in XPS spectra suggests that Au coating is thin.

the Fe (0) state [227] in both the gold coated samples. Analysis of XPS spectra revealed that the surface elemental atomic ratio of gold to iron increased from S-2 to S-3 with increasing gold concentration. The detection of Fe with Au coating in XPS spectra suggests that the gold coating thickness is less than 5 nm [228].

The size and morphology of individual particles were observed in the TEM micrographs (Fig. 4.5). It was observed that the particles were equiaxed for both coated and uncoated samples. The average size of uncoated particles was 10 nm (SD 1), gold coated iron nanoparticles particles had an average size of 15 nm (SD 5). The corresponding size distribution of S-1 and S-3 are shown in Fig. 4.5 c and Fig. 4.5 d, respectively.

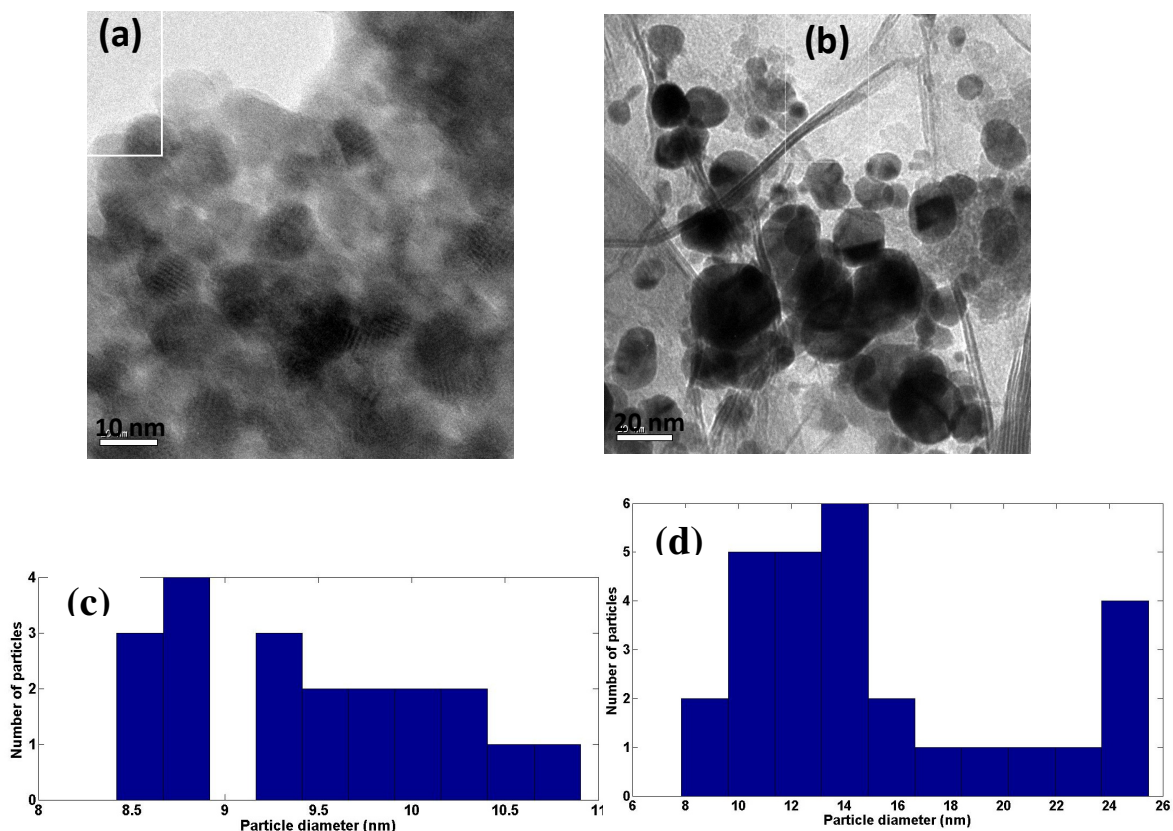


**Figure 4.5** TEM micrographs of (a) S-1 (uncoated) and (b) S-3 (0.204 mmol gold coated iron nanoparticles). The corresponding size distribution of (c) S-1 (uncoated) and (d) S-3 (0.204 mmol gold coated iron nanoparticles).

The colloidal stability of Fe@Au nanoparticles in PBS (pH=7.4) was monitored by dynamic light scattering (DLS) method. PBS represents the typical pH of physiological medium and is a very common biological buffer. Particle size determined by DLS provides the size of aggregates in suspension which is larger than the individual particle size. Figure 4.6 shows the average hydrodynamic diameter of uncoated and Fe@Au nanoparticles as a function of time. The flocculation of uncoated iron nanoparticles occurred within 1 h, whereas Fe@Au nanoparticles were relatively stable up to 4 h, after which flocculation resulted in large aggregates by 6 h.

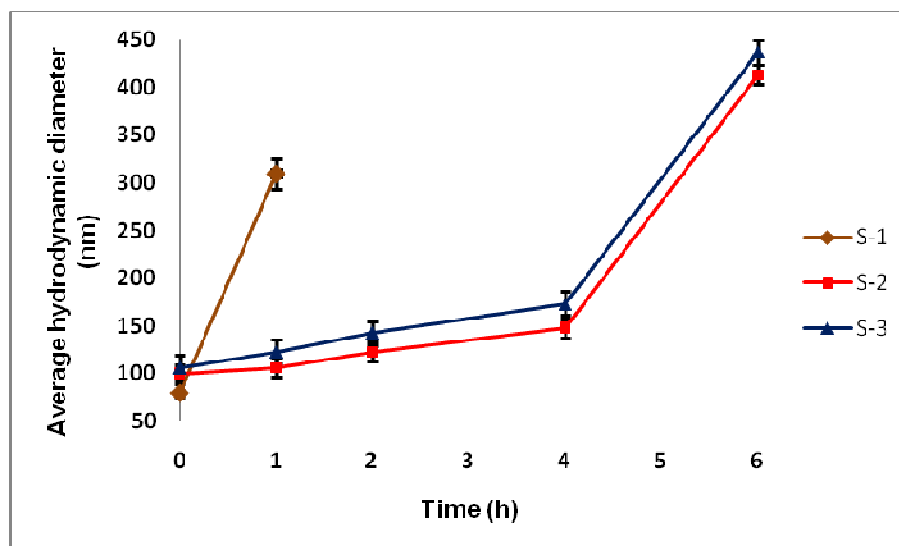


**Figure 4.6** Average hydrodynamic diameter of S-1 (uncoated), S-2 (0.102 mmol gold coated iron nanoparticles) and S-3 (0.204 mmol gold coated iron nanoparticles) in PBS. Uncoated iron nanoparticles flocculate within 1 h, whereas Fe@Au nanoparticles are relatively stable up to 4 h.

Representative plots of magnetization versus field curve measured at room temperature are shown in Fig. 4.7.

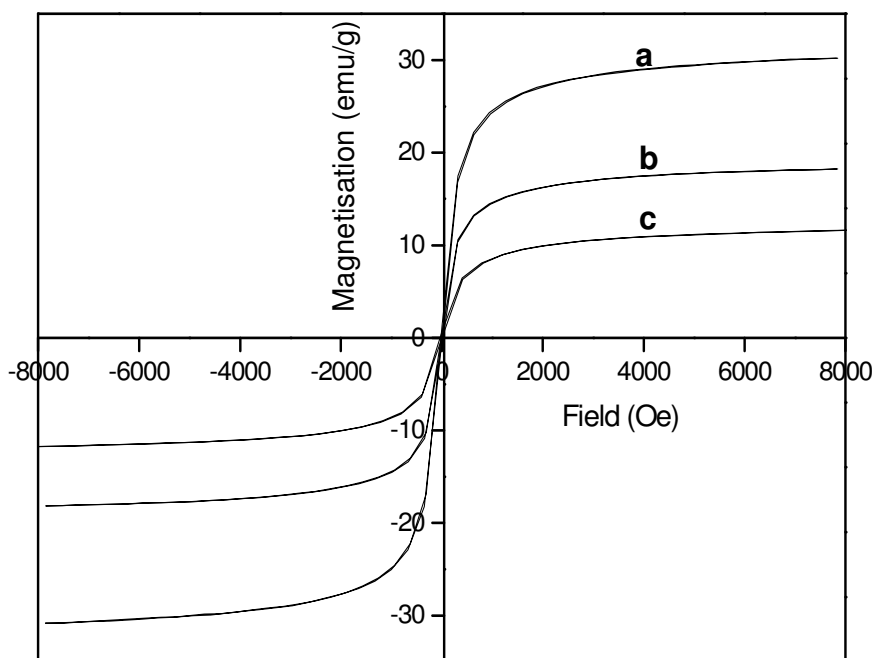


**Figure 4.7** VSM plots of magnetization vs field of (a) S-1 (uncoated), (b) S-2 (0.102 mmol gold coated iron nanoparticles) and (c) S-3 (0.204 mmol gold coated iron nanoparticles). Particles are superparamagnetic,  $M_s$  decreases with an increase in gold concentration.

Interestingly, magnetic measurements revealed that the particles were superparamagnetic as no remanence was observed. In S-1, the magnetization was due to iron oxide, while in S-2 and S-3, magnetization was due to the iron core. It was observed that with increasing gold concentration, the saturation magnetization ( $M_s$ ) of the gold coated iron nanoparticles decreased. The  $M_s$  values were 30.5 emu/g, 18.2 emu/g and 11.9 emu/g for

S-1, S-2 and S-3, respectively (Table 4.1). These magnetization results measured at room temperature agree well with previous reports [119, 229, 230].

**Table 4.1** Saturation magnetization ( $M_s$ ) of Fe@Au.

Sample set	$M_s$ (emu/g)
S-1 (uncoated)	30.5
S-2 (coated with 0.102 mmol of Au)	18.2
S-3 (coated with 0.204 mmol of Au)	11.9

The particle size ( $D$ ) was calculated by fitting the magnetization curves (Fig. 4.7) using the Langevin function [231]:  $M = M_s [\coth(\mu H / K_b T) - (K_b T / \mu H)]$ ; where,  $\mu$  ( $= M_s \pi D^3 / 6$ ) is the magnetic moment,  $K_b$  is the Boltzmann constant,  $T$  is the absolute temperature and  $M_s$  is the saturation magnetization. The size of uncoated particle was found to be 12.5 nm, that of S-2 and S-3 were 14.5 nm and 16 nm, respectively. The gold coating was 2 nm and 3.5 nm in S-2 and S-3, respectively.

The synthesis of Fe@Au nanoparticles and the study of their structural, magnetic properties have been the focus of recent experimental studies [120, 228, 232-241]. The synthesis of Fe@Au is of special interest since gold provides useful surface chemistry and biological reactivity [242-244]. Free iron nanoparticles are easily oxidized, coating the iron nanoparticles with a stable noble metal like gold results in air-stable nanoparticles, which are protected from oxidation [120]. Gold is a favoured coating material because of well known synthesis procedures as well as its chemical functionality [245, 246]. Surface derivatization with gold also helps to reduce particle agglomeration by steric or electronic repulsion and improves biocompatibility [247]. Considerable

---

interest has been directed towards the functionalization of gold nanoparticles by the use of thiol chemistry, which facilitates the attachment of biologically relevant molecules using a variety of thiol linkers [69, 248].

Gold shell magnetic core nanostructures are of special interest because of their potential application in diagnostics and therapy [249]. Gold nanostructures possess unique physical and chemical properties, one of the most fascinating aspects being their strong absorption of light in the visible and near-infrared (NIR) region. The origin of this absorption is attributed to collective conduction band electron oscillation in response to the electrical field of the electromagnetic radiation of light. Termed “surface plasmon,” this optical absorption is strongly dependent on the shape and size of the nanostructure. By coating gold on the surface of the iron core, it is possible to tune these nanoparticles to absorb light in the NIR region. The tuneable optical properties of gold nanostructures are highly desired for many applications that rely on light absorption, including imaging and therapy. Other attractive features of gold shell magnetic nanostructures include easy reductive preparation, high chemical stability, biocompatibility, and affinity for binding to amine and thiol terminal groups in organic molecules. While the gold shell offers useful optical properties, the magnetic core provides the potential for noninvasive imaging using magnetic resonance imaging (MRI), for therapeutic heating in the presence of an alternating magnetic field and for directing nanoparticles to tumors using an external magnetic field. MRI is a noninvasive technique used to obtain anatomic and functional information with high spatial and temporal resolution. Thus, by combining the magnetic property of core and the optical property of the gold shell, the multifunctional gold-shelled magnetic nanostructures can find applications in multimodal imaging, therapeutic combinations such as drug delivery, photothermal therapy and image-guided minimally invasive intervention.

---

Due to its attractive combination of optical and magnetic properties, several groups have studied the structural, optical and magnetic properties of gold coated iron (Fe@Au) nanoparticles. Gold can be coated onto magnetic nanoparticles through reactions in microemulsion, redox transmetalation, iterative hydroxylamine seeding methods [250]. Lin *et al* [119] synthesized Fe@Au nanoparticles of average size of 10 nm by the reverse micelle technique, the particles were superparamagnetic with  $M_s$  of 17 emu/g at 300 K. They reported the absorption bands of gold colloid and Fe@Au colloid at 526 nm and 555 nm, respectively. Chen *et al* reported the reverse micelle synthesis of Fe-Au core-shell nanoparticles with 8 nm diameter and the saturation magnetization ( $M_s$ ), remanent magnetization ( $M_r$ ) and coercivity ( $H_c$ ) were 48 emu/g, 13.67 emu/g and 400 Oe, respectively, at 2 K [120]. Cho *et al* also prepared Fe core/ Au shell of average size of 18 nm by inverse micelle technique and measured the magnetic properties at temperature of 5 K and 300 K [251]. They reported Fe/Au nanoparticles having coercivity ( $H_c$ ) of 400 Oe, remanent magnetization ( $M_r$ ) of 14 emu/g and saturation magnetization ( $M_s$ ) of 43 emu/g at 5 K; whereas Fe/Au nanoparticles were superparamagnetic with  $M_s$  of 17 emu/g at 300 K. The saturation magnetization ( $M_s$ ) decreases with increasing temperature since thermal energy randomizes magnetic moment in different directions.

Pana *et al* reported a saturation magnetization of 4.4 emu/g for Fe-Au core-shell nanoparticles at room temperature, the nanoparticles had a broad size distribution with an average size of 25 nm [252]. Kinoshita *et al* reported gold-iron composite particles of 5 nm, an absorption peak at 520 nm was observed in UV-Visible spectra due to surface plasmon resonance (SPR) of gold [253]. Kim *et al* synthesized nanostructures with a silica core, a gold shell, and a layer of super paramagnetic iron oxide nanoparticles (SPION) sandwiched between silica and gold [131]. Silica spheres (100 nm) were first synthesized using the Stober method [254]. They were covalently attached to SPION

nanospheres and then functionalized with amine so that the gold will attach on the surface. A complete 15-nm thick gold shell was formed in the last step. Similarly, Stoeva *et al* synthesized structured gold nanoshells embedded with silica-stabilized magnetite nanoparticles [255].

Chen *et al* reported a sandwich-like nanostructure composed of a magnetic silica core, an outer silver shell, and a thin layer of gold between the silica and the silver [256]. Nanorice is another gold coated magnetic nanoparticle, shaped like rice that absorbs in the NIR region. These nanostructures display two distinct absorptions observed coming from transverse and longitudinal plasmons. The shorter wavelength is at about 860 nm, while the longer wavelength is at 1160 nm [257]. Wang *et al* synthesized a gold-shelled  $\text{Fe}_3\text{O}_4$  nanostructure with a polymer layer, poly(allylamine hydrochloride), interfacing the  $\text{Fe}_3\text{O}_4$  nanoparticle and the gold shell [258]. Lim *et al* synthesized yolk-shell structured gold nanoparticles that contain SPION in the core and water as the dielectric interface [259].

In this work, superparamagnetic Fe@Au nanoparticles with an average size of 15 nm (SD 5) were synthesized by the reverse micelle technique. The uncoated particles were highly aggregated compared to gold coated particles. The nanoparticles have a tendency to aggregate to reduce their surface energy regardless of the magnetic properties. When the particles are coated with surfactant [260], polymer [113] and dispersed in a carrier fluid, this aggregation is reduced. The uncoated particles (S-1) were oxidized to  $\text{Fe}_3\text{O}_4$  (magnetite) due to exposure to air (Fig. 4.1) as nanoparticles have very large surface area to volume ratio, promoting oxidation to more stable state. By coating with the noble metal gold, this oxidation of iron can be prevented. The gold coating is thin (2 nm and 3.5 nm in S-2 and S-3, respectively), hence Fe as well as Au peaks were observed in XPS

spectra (Fig. 4.4). The positions of Fe and Au peaks (S-2 and S-3) in XRD pattern agree well with previous reports [119, 226, 251, 253, 261].

In this study, the saturation magnetization ( $M_s$ ) of Fe@Au nanoparticles at room temperature is comparable to previous reports [119, 120, 226, 251, 252]. However, the observed  $M_s$  of Fe@Au nanoparticles is lower than that of bulk iron (220 emu/g) [231] because of two effects: (a) gold is a diamagnetic material, interparticle coupling between iron and gold decreases the magnetic properties of the coated nanoparticles and (b)  $M_s$  generally decreases with a decreasing magnetic particle size [262]. The reduced magnetization can be attributed to spin disorder in the surface layer of magnetic nanoparticles [263], their high surface area to volume ratio magnifying this effect as the size decreases. Veranda *et al* reported a linear relationship between  $M_s$  and particle size [264]. In the context of drug delivery, the superparamagnetic nanoparticles are useful because they do not retain magnetization before and after exposure to an external magnetic field, reducing the probability of particle aggregation due to magnetic dipole interaction [265, 266]. Table 4.2 shows a comparison of the gold-shell magnetic nanoparticles synthesized in the current work with selected references.

**Table 4.2** Comparison of gold coated magnetic nanoparticles of current work with selected literature.

Structure	Characteristics	<i>In-vitro</i>	<i>In-vivo</i>	Ref.
SiO <sub>2</sub> /SPION/Au	Size: ~120 nm Surface: PEG and anti-HER2/ <i>neu</i>	T2-weighted MRI	None	[131]
SiO <sub>2</sub> /SPION/Au	Size: >200 nm Surface: thiol modified DNA	None	None	[255]
SPION/SiO <sub>2</sub> /Au	Size: >200 nm Surface: None	None	None	[267]
SPION/polymer/Au	Size: 273 ± 17.9 nm Surface: None	None	None	[258]
SPION/Au	Size: Longitudinal = 340 ± 20 nm; transverse = 54 ± 4 nm Surface: None	None	None	[257]
SPION/SiO <sub>2</sub> /Au	Size: ~80 nm Surface: PEG	Photothermal ablation using 808 nm laser	Darkening of tumor in mice in T2-weighted MRI, increase in temperature of ~60°	[268]
Hollow Au nanoshell	Size: 30.4 ± 4.4 nm Surface: C225 monoclonal antibody	Selective binding of C225-HGN with A431 cells	More C225-HGN localized into tumor	[249]
Fe/Au	Size: individual particle of 15 nm, Aggregate size: 100 nm	Dox loading/ release and targeting	None	This work

*In summary, gold coated iron (Fe@Au) individual nanoparticles of average size 15 nm (aggregate size ~ 100 nm) were synthesized by the reverse micelle technique, these nanoparticles exhibited superparamagnetic character and decreasing saturation magnetization with increasing Au coating thickness.*

## 4.2 PVA coated iron oxide (PVA-IO) MCP system

Here structural, morphological and magnetic properties of uncoated and PVA coated iron oxide nanoparticles are presented. The particles were characterized by XRD, TEM, TGA, FTIR and VSM. DOX loading and release studies of PVA-IO nanoparticles are also presented.

### 4.2.1 Physical properties

Representative powder X-ray diffraction patterns of uncoated (S-4) and PVA coated iron oxide nanoparticles (S-6 and S-8) are presented in Fig. 4.8.

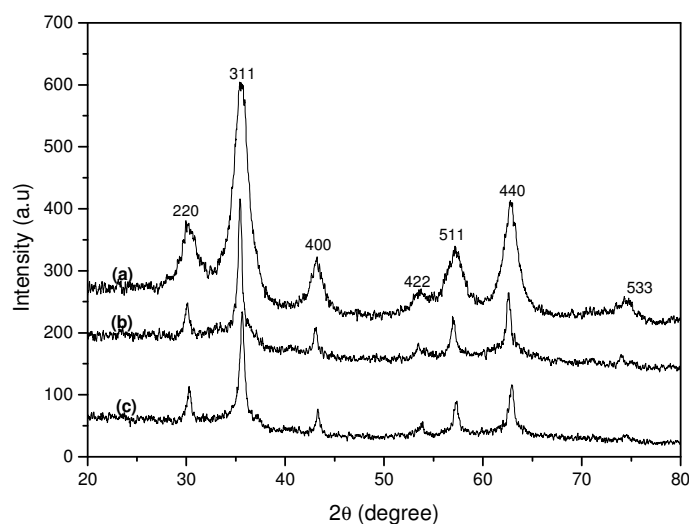


**Figure 4.8** X-ray diffraction patterns of (a) S-8 (5 wt% PVA coated iron oxide), (b) S-6 (1 wt% PVA coated iron oxide) and (c) S-4 (Uncoated iron oxide). The phase is magnetite (Fe<sub>3</sub>O<sub>4</sub>), peaks corresponding to reflection planes are indexed.

From the XRD analysis, it was found that the peaks corresponded to the spinel structure of magnetite phase ( $\text{Fe}_3\text{O}_4$ , reference JCPDS No. 82-1533). The peaks corresponding to reflection planes were indexed (Fig. 4.8). From the absence of (210) and (300) peaks in the XRD patterns, it can be concluded that separate maghemite ( $\gamma\text{-Fe}_2\text{O}_3$ ) was not present in the samples. Interestingly, there was a broadening of peaks from Fig. 4.8.b to Fig. 4.8.a with an increase in polymer concentration. The broadening of XRD peaks is predominantly attributed to the decrease in crystallite size. The mean crystallite size was calculated using Scherrer's formula. The mean crystallite size of uncoated (S-4) sample was 19.3 nm and that of S-5, S-6, S-7, S-8 was 14.6 nm, 7.9 nm, 5.6 nm and 4.5 nm, respectively. Rietveld refinement of the XRD patterns of S-4 and S-8 using TOPAZ (version 4.1) software is shown in Fig. 4.9.

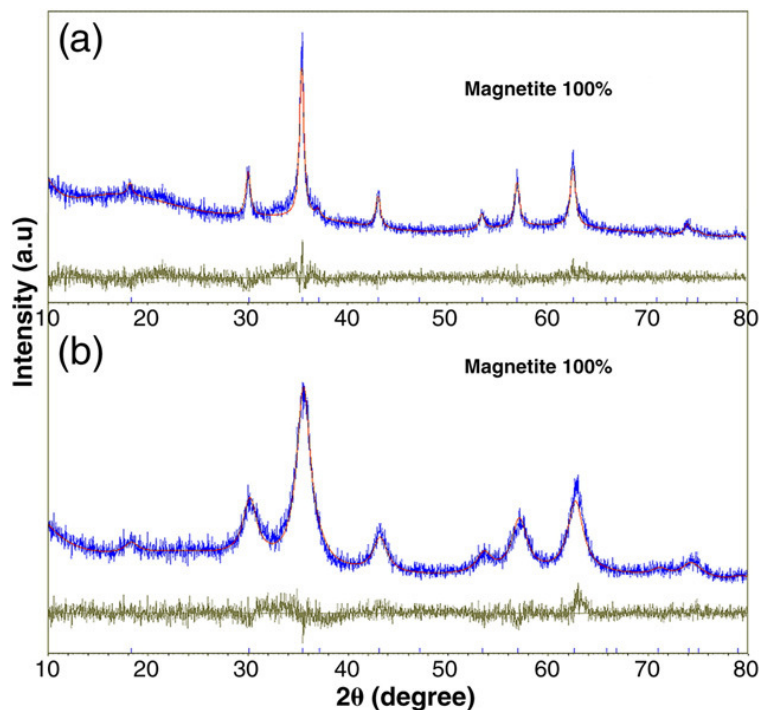


**Figure 4.9** Rietveld refinement of X-ray diffraction pattern of (a) S-4 (uncoated iron oxide) and (b) S-8 (5 wt% PVA coated iron oxide). Peak broadening occurs in PVA coated iron oxide nanoparticles due to decrease in crystallinity.

Lattice parameter calculated from Rietveld refinement ( $a = 8.39 \text{ \AA}$ ) is very close to that of magnetite ( $\text{Fe}_3\text{O}_4$ ) (lattice parameter ( $a$ ) from the literature;  $\text{Fe}_3\text{O}_4$ :  $8.396 \text{ \AA}$  and  $\gamma\text{-Fe}_2\text{O}_3$ :  $8.35 \text{ \AA}$ ) [269]. XRD results shown here agree well with previous reports [64, 150, 151, 220].

TEM micrographs of uncoated (S-4) and PVA-IO (S-8) are shown in Fig. 4.10. The average size of uncoated iron oxide particles was 12 nm (SD 4), PVA-IO had an average size of 14 nm (SD 3). The corresponding size distribution of S-4 and S-8 are shown in Fig. 4.10 c and Fig. 4.10 d, respectively.

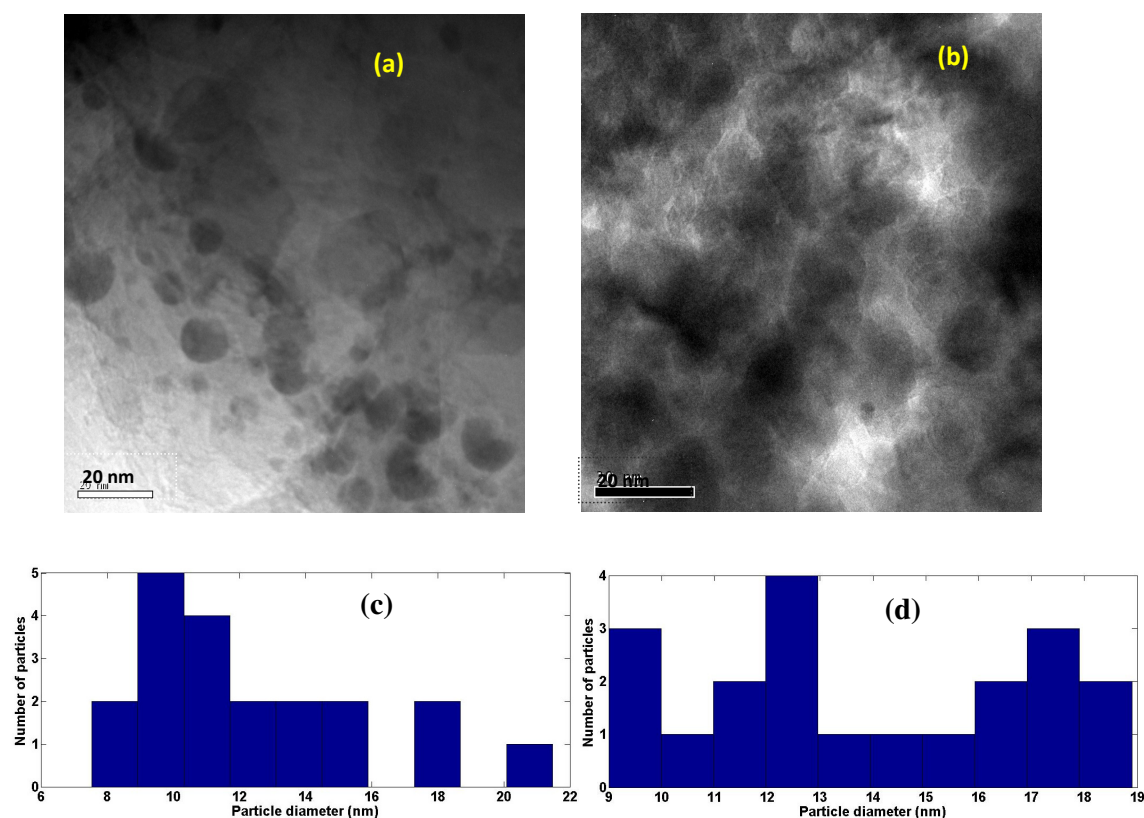


**Figure 4.10** TEM micrographs of (a) S-4, corresponding to the uncoated iron oxide nanoparticles and (b) S-8, coated with 5 wt% PVA. The corresponding size distribution of (c) S-4 (uncoated iron oxide) and (d) S-8 (5 wt% PVA coated iron oxide).

The colloidal stability of PVA-IO in PBS (pH=7.4) was determined by dynamic light scattering (DLS). Figure 4.11 shows the average hydrodynamic diameter of uncoated and PVA coated iron oxide nanoparticles as a function of time. The flocculation of uncoated iron oxide nanoparticles occurred within 1 h, whereas PVA-IO were stable up to 8 h. The stability of PVA-IO in suspension is due to steric-repulsion.

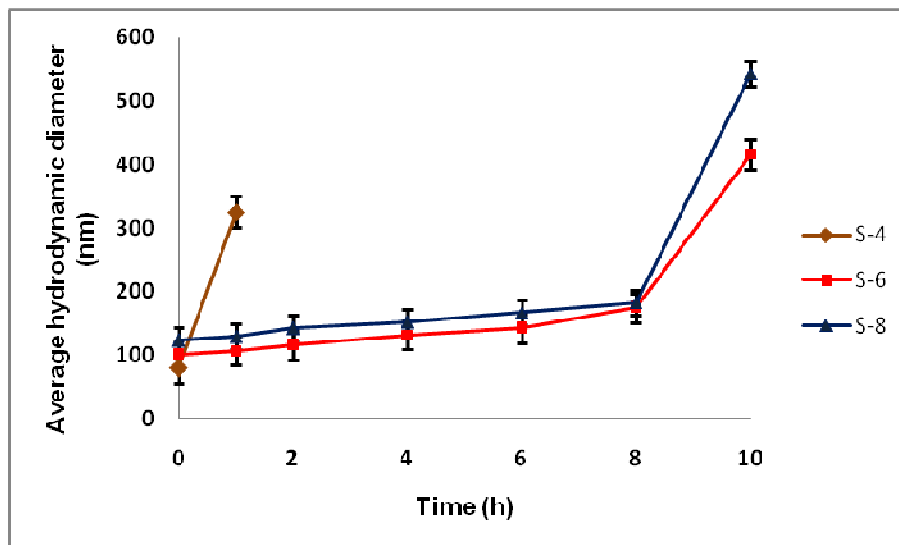


**Figure 4.11** Average hydrodynamic diameter of S-4 (uncoated iron oxide nanoparticles), S-6 (iron oxide nanoparticles coated with 1 wt% PVA) and S-8 (iron oxide nanoparticles coated with 5 wt% PVA) in PBS.

Several researchers have studied the synthesis and characterization of PVA-IO nanoparticles. Lee *et al* [150] synthesized ultrafine  $\text{Fe}_3\text{O}_4$  particles (4-7 nm) by precipitation in aqueous PVA solution and showed that relative crystallinity and saturation magnetization ( $M_s$ ) decreased with increasing PVA concentration. Chastellain *et al* reported a multistep synthesis of PVA coated  $\text{Fe}_3\text{O}_4$  nanoparticles (5-20 nm) by the co-precipitation method followed by a thermochemical treatment [151]. Mohapatra *et al* prepared polyvinyl alcohol phosphate (PVAP) coated magnetite nanoparticles having a

---

broad size distribution (13-55 nm), which were superparamagnetic at room temperature with 35 emu/g and 15 emu/g for 0.5 % and 1 % PVAP respectively [64]. Petri-Fink *et al* coated superparamagnetic iron oxide nanoparticles (9 nm) with amino functionalized PVA and demonstrated the interactions with human melanoma cells [65].

In this work, PVA-IO individual particles of average size 14 nm (SD 3) were synthesized by the co-precipitation technique. The broadening of XRD peaks with increasing PVA concentration was observed due to a decrease in crystallinity. The broadening of XRD peaks is attributed to the decrease in crystallite size, which can be explained by the Scherrer's formula i.e.,  $D = (0.9 \lambda) / (\beta \cos \theta)$ ; where  $D$  = Mean crystallite size,  $\lambda$  = X-ray wave length,  $\beta$  = broadening of diffraction line at half of its maximum intensity in radians and  $\theta$  = diffraction angle. As the crystallite size is inversely proportional to peak width, a decrease in crystallite size causes the peak to broaden.

### 4.2.2 PVA adsorption onto iron oxide nanoparticles

The amount of PVA adsorbed onto the iron oxide nanoparticles was studied by thermogravimetric analysis (TGA). Figure 4.12 shows the weight loss vs. temperature curves of pure PVA (inset), uncoated iron oxide and PVA-IO heated up to 600°C in air.

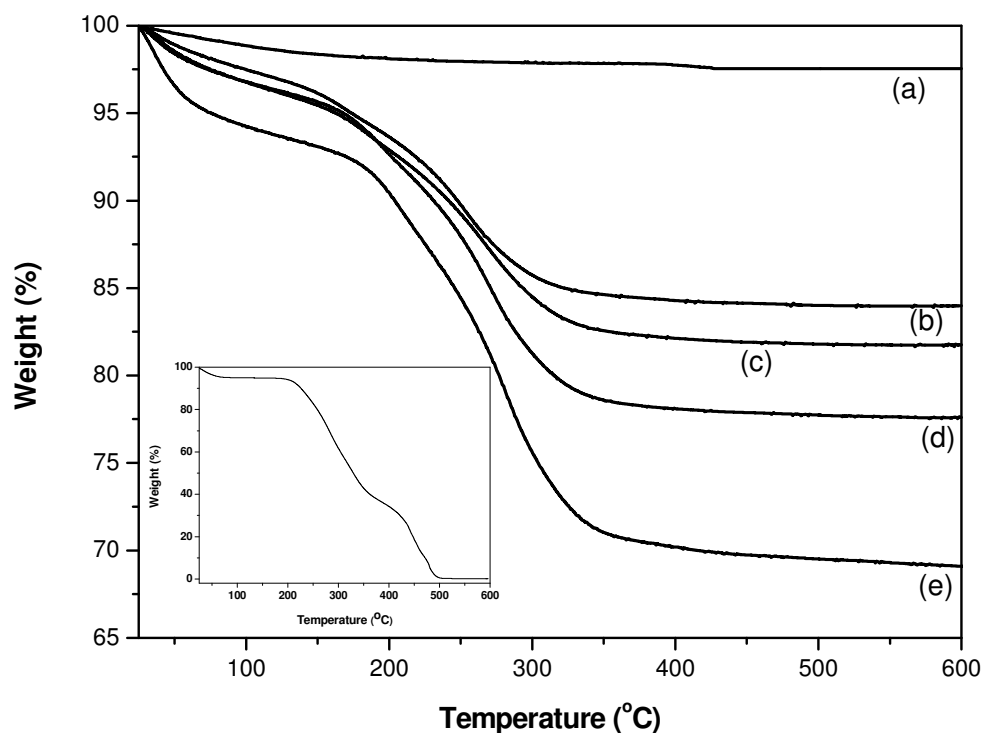


**Figure 4.12** Weight loss vs. temperature TGA curves of (a) S-4 (uncoated iron oxide), (b) S-5 (iron oxide coated with 0.5 wt% PVA), (c) S-6 (iron oxide coated with 1 wt% PVA), (d) S-7 (iron oxide coated with 2 wt% PVA) and (e) S-8 (iron oxide coated with 5 wt% PVA) heated up to 600°C in air. The inset shows the TGA curve of pure PVA indicating complete degradation of PVA when heated up to 600°C.

The inset shows that pure PVA degrades completely when heated up to 600°C. There is no significant weight loss in the TGA curve of uncoated iron oxide nanoparticles (Fig.

4.12.a), whereas there are distinct weight losses in the TGA curves of PVA-IO (Figs. 4.12.b – 4.12.e). The initial weight loss up to 100°C is due to desorption of physically adsorbed water. The weight loss from 200 to 500°C is due to the dehydration reaction of –OH groups in PVA chains and subsequent degradation of PVA releasing CO<sub>2</sub> gas. The weight loss due to PVA is presented in Table 4.3.

**Table 4.3** Weight loss due to PVA in thermogravimetric analysis (TGA) in air.

Sample set	Wt loss (%)
S-5 (0.5 wt% PVA coated)	11
S-6 (1 wt% PVA coated)	14
S-7 (2 wt% PVA coated)	18
S-8 (5 wt% PVA coated)	23

PVA coating thickness was calculated from the weight loss in TGA curves, assuming that each iron oxide core was coated with PVA shell. The PVA coating was found 1.5 nm, 2.2 nm, 3 nm and 3.7 nm in S-5, S-6, S-7 and S-8, respectively.

PVA is known to adsorb nonspecifically on oxide surfaces through hydrogen bonding arising from the polar functional groups of PVA and the hydroxylated and protonated surface of the oxide [270]. However, the actual configuration of the adsorbed PVA is difficult to determine since it is affected by concentration and molecular weight of PVA, pH, ionic strength and surface charge [151]. Chibowski *et al* showed the influence of the acetate block in the PVA chain on the adsorption behaviour of PVA on TiO<sub>2</sub> [271]. Cohen Stuart *et al* reported that the amount of adsorbed PVA on TiO<sub>2</sub> surface strongly

depends on the number of long polymer chains as they adsorb preferentially compared to smaller chains [272]. In addition to the polymer-inorganic oxide surface interactions, PVA has hydrogen bonding between polymer chains, resulting in a hydrogel structure [273] in which the magnetic particles are embedded.

FTIR was used to study the attachment of the polymer to the magnetic nanoparticles. Figure 4.13 shows the FTIR spectra of uncoated and PVA-IO. The series of characteristic IR bands are summarized in detail in Table 4.4 [274], the salient features are discussed below.

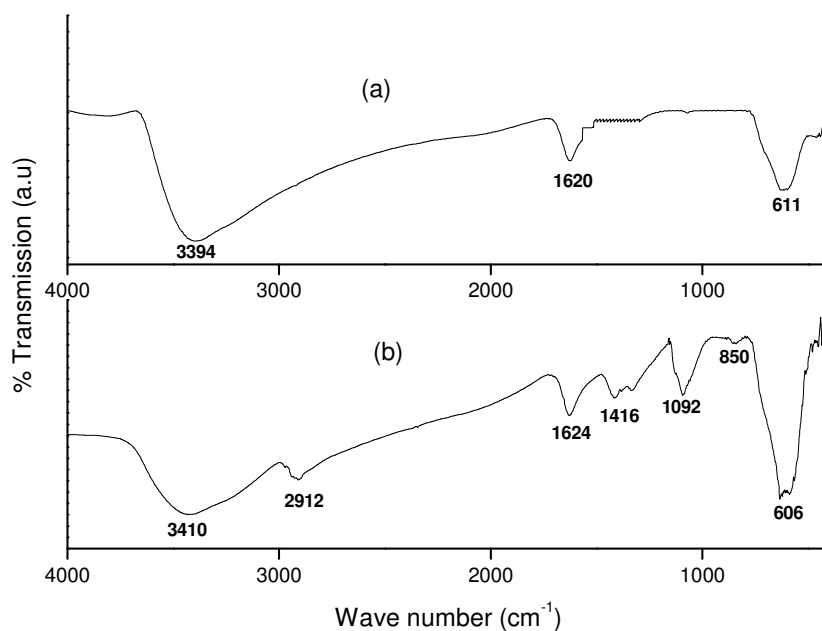


**Figure 4.13** FTIR spectra of (a) uncoated iron oxide and (b) PVA-IO nanoparticles. Bands at 2912, 1416, 1092 and 850  $\text{cm}^{-1}$  in PVA-IO nanoparticles confirm the attachment of PVA to iron oxide nanoparticles.

In the case of uncoated iron oxide, the band at  $3394\text{ cm}^{-1}$  was assigned to O-H stretching ( $\nu$ ) vibrations and the band at  $1620\text{ cm}^{-1}$  was assigned to O-H bending ( $\delta$ ) vibrations due to adsorbed water on the surface of the iron oxide nanoparticles. The band observed at  $611\text{ cm}^{-1}$  corresponded to stretching vibrations of  $M_{\text{Th}}\text{-O-M}_{\text{Oh}}$ , where  $M_{\text{Th}}$  and  $M_{\text{Oh}}$  represented the iron occupying tetrahedral and octahedral positions, respectively. In PVA-IO, the  $M_{\text{Th}}\text{-O-M}_{\text{Oh}}$  stretching band at  $606\text{ cm}^{-1}$  and the alcoholic O-H stretching band at  $3410\text{ cm}^{-1}$  were observed. The additional bands at  $2912\text{ cm}^{-1}$  corresponding to C-H stretching vibrations, at  $1416\text{ cm}^{-1}$  corresponding to C-C stretching vibrations, at  $1092\text{ cm}^{-1}$  attributable to M-O-H (M=Fe) bond and at  $850\text{ cm}^{-1}$  corresponding to  $\text{CH}_2$  rocking were observed in PVA-IO nanoparticles, confirming the attachment of PVA onto iron oxide nanoparticles, which was also supported by thermal analysis.

The interaction between polymer coating and  $\text{Fe}_3\text{O}_4$  particles was studied earlier [275-279]. Polymer interactions were studied in  $\text{Fe}_3\text{O}_4$ /polypyrrole and  $\text{Fe}_3\text{O}_4$ /polyaniline nanocomposites, where interactions exist between the lone pair electrons of the N atom in the polypyrrole chain or in the polyaniline chain with the 3d orbital of the Fe atom to form a coordinate bond [275, 276]. Li *et al* reported that oleic acid adsorption on the surface of  $\text{Fe}_3\text{O}_4$  nanoparticles could be due to hydrogen bonding or a coordination linkage [277]. Zhang *et al* reported the attachment of polymethacrylic acid to  $\text{Fe}_3\text{O}_4$  nanoparticles via coordination linkages between the carboxyl groups and iron [278]. In the present work, it is confirmed by FTIR analysis (Fig. 4.13) that the attachment of PVA to iron oxide nanoparticles occurs via hydrogen bonding between hydroxyl group of PVA and protonated surface of the oxide.

**Table 4.4** Assignment of FTIR spectra of uncoated iron oxide, PVA-IO [274].

Samples	IR region or bands (cm <sup>-1</sup> )	Description
Uncoated iron oxide	3394	$\nu$ (H-O)
	1620	$\delta$ (H-O-H) of adsorbed water
	611	$\nu$ (M <sub>Th</sub> -O-M <sub>Oh</sub> )
PVA coated iron oxide	3410	$\nu$ (H-O)
	2912	$\nu$ (C-H)
	1624	$\delta$ (H-O-H)
	1416	$\nu$ (C-C)
	1092	$\nu$ (M-O-H (M=Fe))
	850	CH <sub>2</sub> rocking
	606	$\nu$ (M <sub>Th</sub> -O-M <sub>Oh</sub> )

### 4.2.2 Magnetic properties

Figure 4.14 shows the room temperature magnetization curves of uncoated iron oxide and PVA-IO nanoparticles.

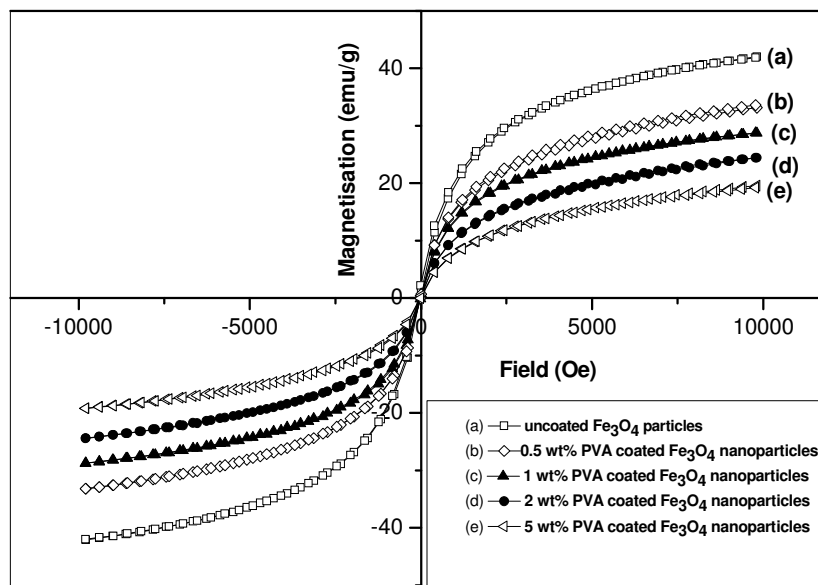


**Figure 4.14** Magnetization vs. field curves measured at room temperature of (a) S-4, corresponding to uncoated iron oxide nanoparticles, (b) S-5, iron oxide coated with 0.5 wt% PVA, (c) S-6, iron oxide coated with 1 wt% PVA, (d) S-7, iron oxide coated with 2 wt% PVA and (e) S-8, iron oxide coated with 5 wt% PVA. Particles are superparamagnetic, Saturation magnetization decreases with increase in PVA concentration.

The absence of remanence in the hysteresis curves indicates that magnetic particles are superparamagnetic. The saturation magnetization ( $M_s$ ) of uncoated sample (S-4) was 42 emu/g, less than that of bulk magnetite (88 emu/g) reported earlier [231, 280, 281]. As expected, the  $M_s$  of PVA-IO decreased with increasing PVA concentration (Table 4.5).

In this study, the observed saturation magnetization ( $M_s$ ) of PVA-IO is comparable to previous reports [64, 220].

**Table 4.5** Saturation magnetization ( $M_s$ ) of uncoated and PVA-IO nanoparticles.

Sample set	Saturation Magnetization (emu/g)
S-4 (uncoated)	42
S-5 (0.5 wt% PVA coated)	33
S-6 (1 wt% PVA coated)	28
S-7 (2 wt% PVA coated)	23
S-8 (5 wt% PVA coated)	19

Superparamagnetic PVA-IO nanoparticles are useful in drug delivery, since these particles do not retain magnetization before and after exposure to an external magnetic field, reducing the probability of particle aggregation due to magnetic dipole interaction [265, 266]. The observed  $M_s$  of uncoated  $\text{Fe}_3\text{O}_4$  nanoparticles was lower than that of bulk magnetite since  $M_s$  decreases with a decrease in magnetic particle size [262]. For PVA-IO,  $M_s$  decreases with increasing PVA concentration (Fig. 4.14). This is due to the dilution effect from adsorbed water and the hydroxyl content of PVA and the possibility of a small volume fraction of antiferromagnetic amorphous iron oxides. Reduced magnetization could also result from the small particle surface effect [282], which refers to the disordered alignment of surface atomic spins induced by reduced coordination and broken exchange between surface spins [64]. This surface effect is more prominent in

small particles as the ratio of surface atoms to the interior atoms increases with a decrease in particle size.

*In summary, PVA-IO individual particles with average size of 14 nm (SD 3) were synthesized by co-precipitation technique; these particles were superparamagnetic with decreasing  $M_s$  with increasing PVA concentration. The attachment of PVA to iron oxide nanoparticles occurred via hydrogen bonding between hydroxyl group of PVA and protonated surface of the oxide.*

### **4.3 Doxorubicin (DOX) drug loading and release**

DOX was used to study the drug loading and release behaviour of Fe@Au and PVA-IO MCP. The starting ratio by weight of MCP to DOX was 10 for drug loading. The drug loading of Fe@Au MCP was qualitatively monitored by a change in the color of DOX, which changed from deep orange (Fig. 4.15.a) to a much lighter color with increasing time as DOX was adsorbed to MCP (Fig. 4.15.c). When only uncoated iron nanoparticles were used for drug loading, no change in the color and concentration of DOX was observed (Fig. 4.15.b), which indicates that there is no drug adsorption onto the uncoated nanoparticles.

The zeta potential of Fe@Au, PVA-IO, DOX-attached Fe@Au and DOX-attached PVA-IO was determined by Malvern Zetasizer. The average values of zeta potential of Fe@Au, PVA-IO, DOX-attached Fe@Au and DOX-attached PVA-IO were -33.3 mV, -38.3 mV, -24.3 mV and -23.6 mV, respectively. Loading of DOX onto Fe@Au and PVA-IO surface increases positive potential, since DOX is a cationic drug.

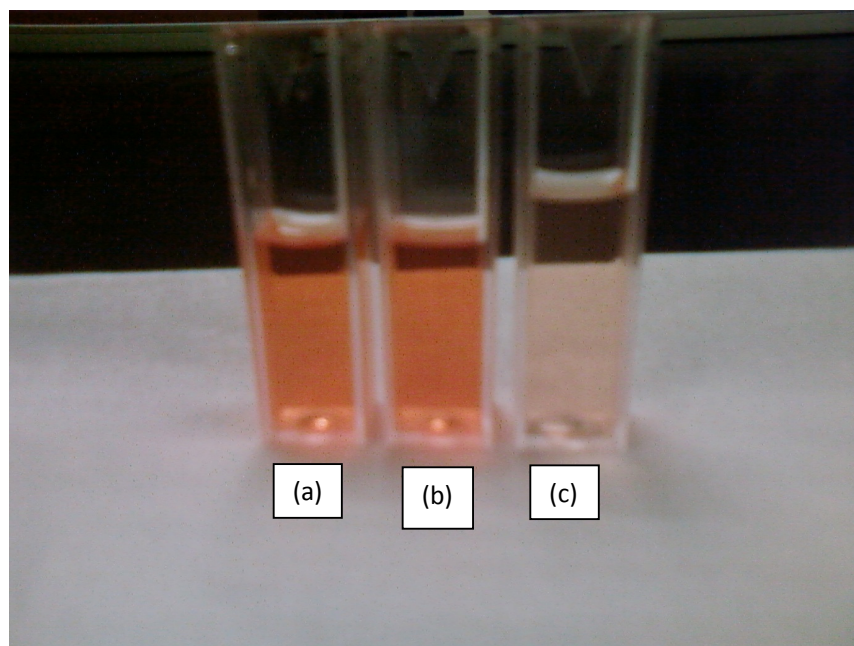


**Figure 4.15** The color of (a) pure DOX solution, (b) DOX solution after 26 h mixing with uncoated iron nanoparticles and (c) DOX solution after 26 h mixing with gold coated iron (Fe@Au) nanoparticles. The change in color of DOX indicates that the DOX is attached onto Fe@Au nanoparticles only.

#### 4.3.1 Gold coated iron (Fe@Au) MCP system

DOX loading and release profiles of Fe@Au MCP were studied. The DOX loading and release profiles of Fe@Au MCP are shown in Fig. 4.16. The DOX loading and release increased with increase in gold content in the magnetic carriers. Initially there was a rapid adsorption of DOX, then the adsorption rate slowed down and finally reached the saturation value (Fig. 4.16.a). It was found that the drug loading capacity increased with increasing gold content in the magnetic carriers. In 26 h of loading, 83  $\mu\text{g}$  and 94  $\mu\text{g}$  of DOX were loaded per mg of S-2 and S-3, respectively. The drug release behaviour of

Fe@Au MCP was investigated in PBS buffer at pH of 7.4 and temperature of 37°C to maintain the experimental conditions similar to body fluid. Figure 4.16.b shows the release profiles of DOX from the Fe@Au MCP. It is apparent from Fig. 4.16.b that there was a continuous release of drug up to 10 h beyond which it slowed down. A maximum of 18% and 25% of adsorbed drug was released in 80 h from S-2 and S-3, respectively.

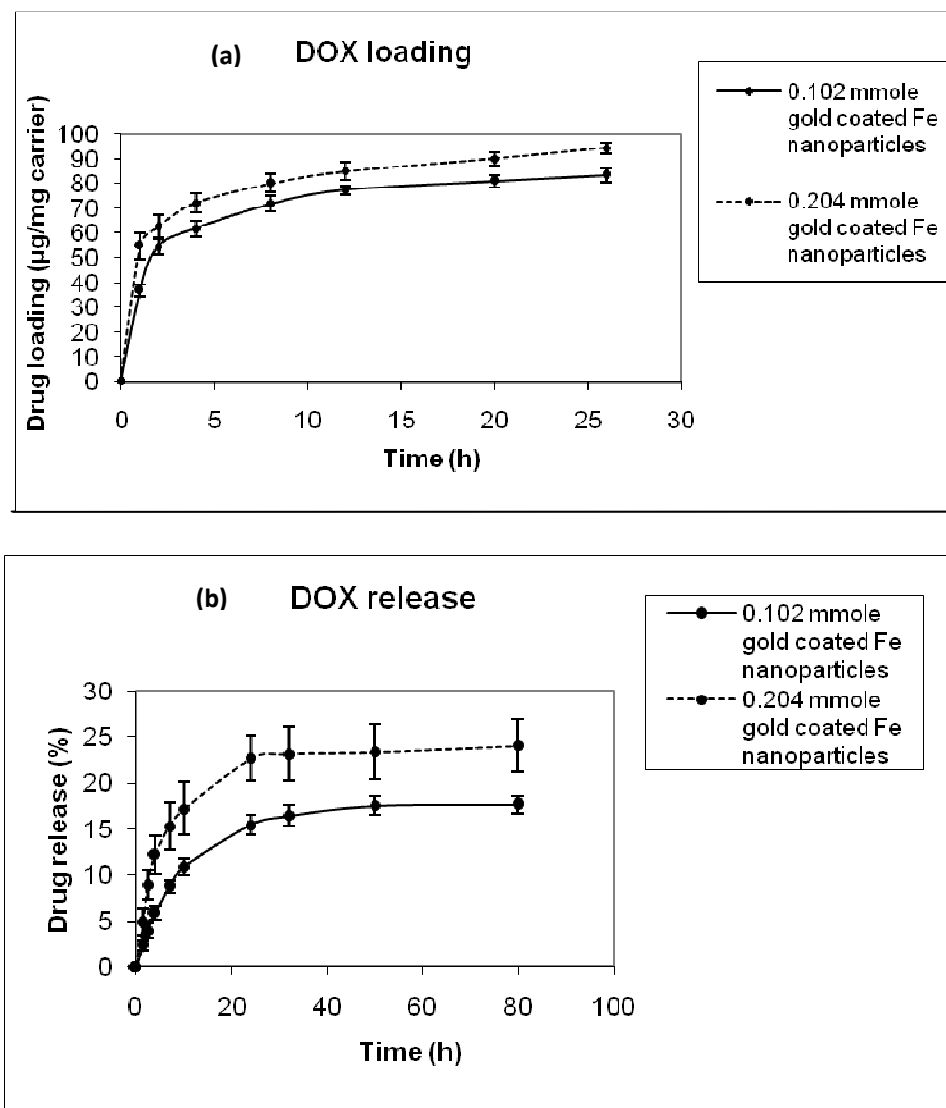


**Figure 4.16** DOX (a) loading and (b) release profiles of gold coated iron (Fe@Au) MCP.

The binding of DOX with Fe@Au nanoparticles was studied by FTIR spectroscopy.

Figure 4.17 shows FTIR spectra of Fe@Au, pure DOX and DOX-attached Fe@Au nanoparticles.

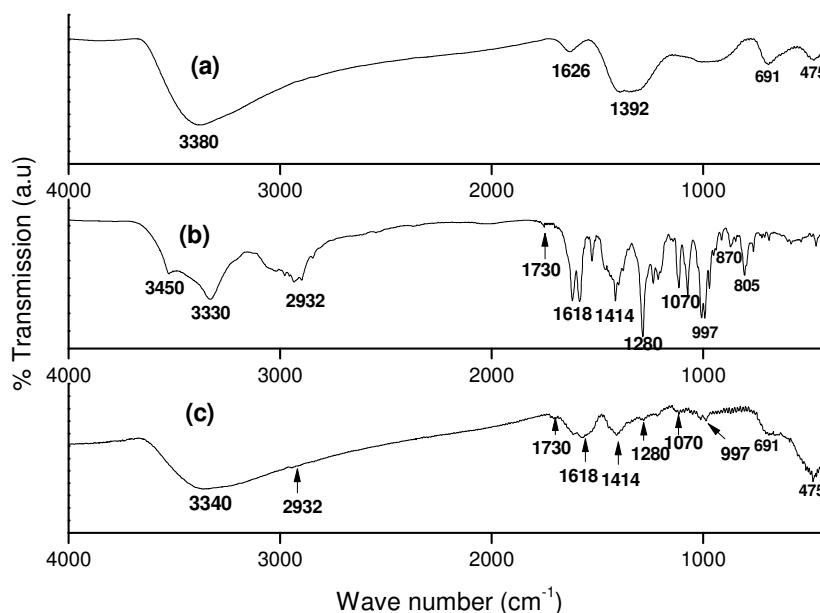


**Figure 4.17** FTIR spectra of (a) Fe@Au, (b) pure DOX and (c) DOX-attached Fe@Au nanoparticles. Amine ( $-\text{NH}_2$ ) group of DOX is involved in attachment to the Fe@Au nanoparticles.

In the case of Fe@Au nanoparticles, peaks at  $3380\text{ cm}^{-1}$  (H-O stretching),  $1626\text{ cm}^{-1}$  (H-O-H bending) were due to adsorbed water on the surface of nanoparticles and at  $1392\text{ cm}^{-1}$  (C-C stretching) from the surfactant. The FTIR spectrum of pure DOX showed multiple peaks at  $2932\text{ cm}^{-1}$  (C-H stretching),  $1730\text{ cm}^{-1}$  (C=O stretching),  $1618\text{ cm}^{-1}$  (N-H bending),  $1414\text{ cm}^{-1}$  (C-C stretching),  $1280\text{ cm}^{-1}$  (C-O-C stretching),  $1070\text{ cm}^{-1}$  (C-O stretching),  $997\text{ cm}^{-1}$  (C-O-C stretching) and peaks at  $870$  and  $805\text{ cm}^{-1}$  corresponding to amine (N-H) wag [83]. Interestingly for pure DOX, peaks at  $3450\text{ cm}^{-1}$  due to N-H

stretching vibrations for primary amine structure and at  $3330\text{ cm}^{-1}$  due to O-H stretching vibrations were observed. However, for DOX-attached Fe@Au nanoparticles, peaks due to N-H stretching vibrations and O-H stretching vibrations overlapped and were broadened ( $\sim 3340\text{ cm}^{-1}$ ). The sharp peaks at  $870$  and  $805\text{ cm}^{-1}$  observed in pure DOX due to amine (N-H) was also diminished in the FTIR spectrum of DOX-attached Fe@Au nanoparticles. From this FTIR analysis, it can be interpreted that  $\text{-NH}_2$  group of DOX is the active site for the attachment to the Fe@Au nanoparticles.

The interaction of DOX with gold was further investigated by measuring the optical properties of Fe@Au colloid, pure DOX solution and DOX-attached Fe@Au colloid (Fig. 4.18).

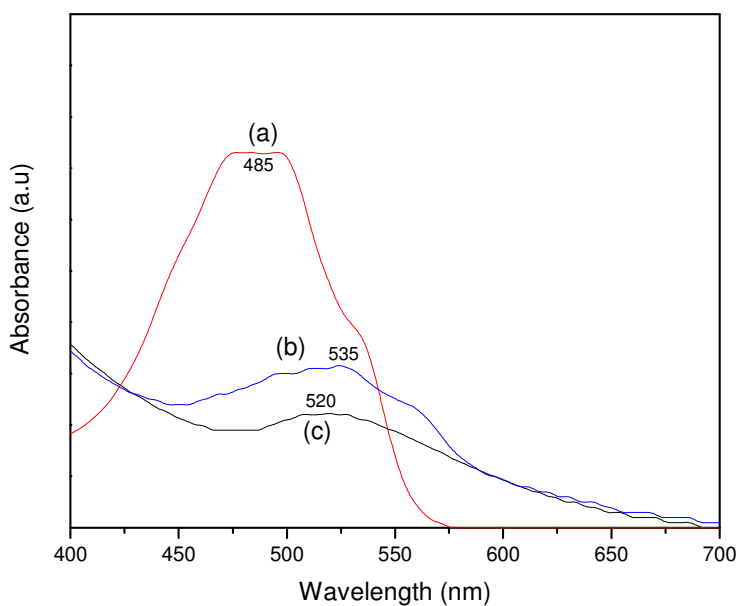


**Figure 4.18** UV-vis spectra of (a) pure DOX, (b) DOX-attached Fe@Au and (c) Fe@Au colloid. Peak is broadened and red shifted at 535 nm upon addition of colloidal Fe@Au to DOX.

The absorption band observed for Fe@Au colloid at 520 nm in the UV–visible spectrum was due to surface plasmon resonance (SPR), which is characteristic of gold nanoparticles [228]. Pure DOX showed an absorption maximum at 485 nm and it was observed that with the addition of colloidal Fe@Au to DOX, peak was broadened and red shifted at 535 nm due to interaction of DOX with the Au surface [283]. This interaction is due to the attachment of DOX with gold, arising from a large electrostatic attraction of active groups ( $-\text{NH}_2$ ) in DOX with gold.

The interaction of DOX with the Fe@Au nanoparticles is due to the attachment of  $-\text{NH}_2$  group of DOX with the gold shell, as evidenced by the peak broadening of N-H stretching vibrations of DOX-conjugated Fe@Au nanoparticles in FTIR spectra (Fig. 4.17) and red shifting of absorption band of Fe@Au colloid with addition of DOX in UV-visible spectra (Fig. 4.18). Selvaraj *et al* reported that  $-\text{NH}$  group of 5-Fluorouracil drug was involved in binding the drug onto the gold nanoparticle surface [68] and Aslam *et al* showed that gold has a strong affinity to the amino group [284]. The drug release can be explained by the covalent conjugation model postulated by Ringsdorf [285], where the cleavage of Au-DOX coordinate linkers results in the release of attached drug. The DOX loading of Fe@Au nanoparticles is comparable to that of Arruebo *et al* [222] where zeolite-magnetite nanocomposite was loaded with DOX. Kuznetsov *et al* reported that a maximum of 62  $\mu\text{g}$  of DOX was loaded per mg of ferro-carbon adsorbent and approximately 25% of adsorbed DOX was released from iron-carbon adsorbent in 24 h [221].

#### 4.3.2 PVA-IO MCP system

The DOX loading and release profiles of PVA-IO nanoparticles are shown in Figs. 4.19 and 4.20, respectively. Initially there was a rapid adsorption of DOX, then the adsorption

rate slowed down and finally reached the saturation value (Fig. 4.19). It was found that higher PVA content resulted in higher drug adsorption, 35  $\mu\text{g}$ , 41  $\mu\text{g}$ , 47  $\mu\text{g}$ , 58  $\mu\text{g}$  of DOX per mg of carrier was loaded in 26 h with 0.5 wt%, 1 wt%, 2 wt% and 5 wt% PVA respectively.

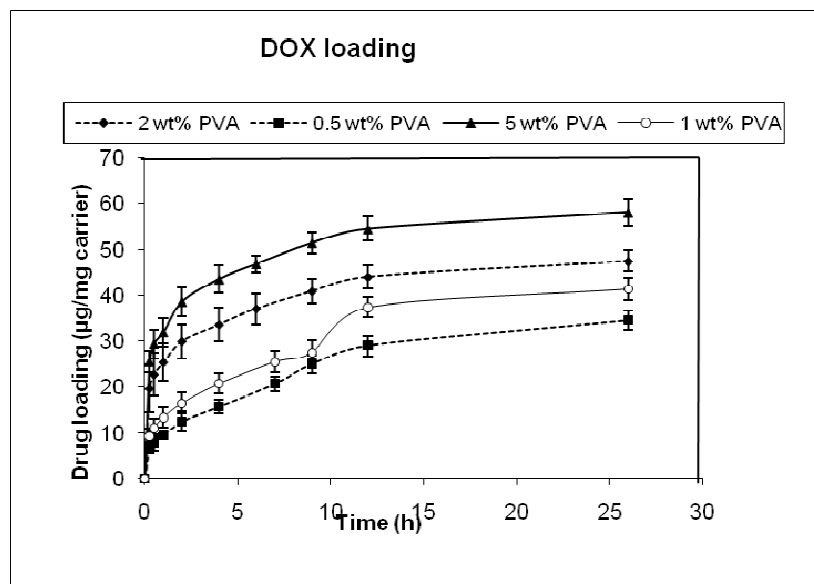


**Figure 4.19** DOX loading on to PVA-IO nanoparticles, DOX loading increases with increase in PVA concentration.

The drug release behaviour of PVA-IO MCP was investigated in PBS buffer at pH of 7 and temperature of 37°C to maintain the experimental conditions similar to body fluid. The DOX release profiles from PVA-IO MCP are presented in Fig. 4.20. The release profiles showed that initially there was a rapid release until 6 h after which release slowed down. A maximum of 45%, 33%, 25% and 17% of adsorbed drug were released in 80 h from carriers coated with 0.5 wt%, 1 wt%, 2 wt% and 5 wt% PVA, respectively.

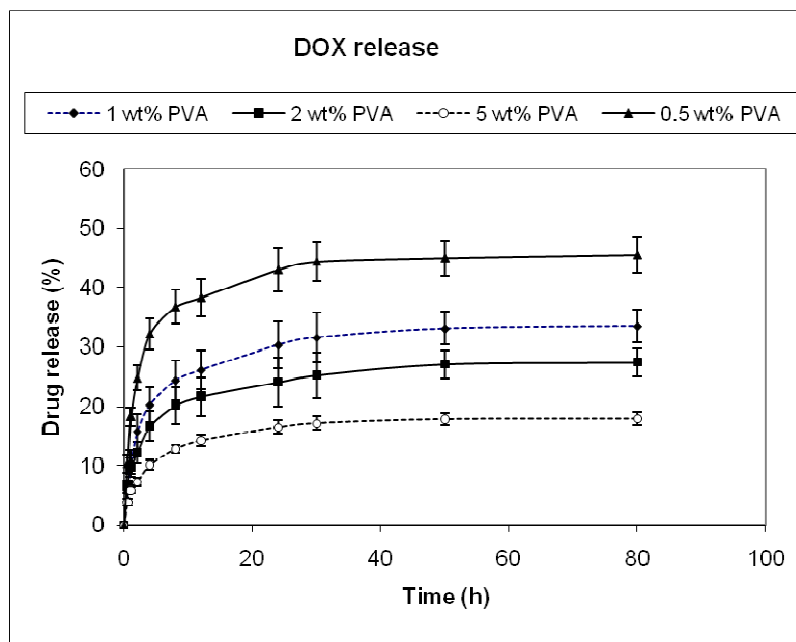


**Figure 4.20** DOX release from PVA-IO nanoparticles, DOX release follows the Fickian diffusion controlled process.

FTIR was used to study the conjugation of DOX with the PVA-IO nanoparticles. FTIR spectra of pure DOX and DOX-conjugated PVA-IO nanoparticles are presented in Fig. 4.21. It is interesting to notice that peaks at  $3450\text{ cm}^{-1}$  due to N-H stretching vibrations for the primary amine structure and at  $3330\text{ cm}^{-1}$  due to O-H stretching vibrations were observed for pure DOX. However, in the case of DOX-conjugated PVA-IO nanoparticles, peaks due to N-H stretching vibrations and O-H stretching vibrations overlapped, were broadened and shifted to the lower frequency range ( $\sim 3265\text{ cm}^{-1}$ ). The bands observed at  $870\text{ cm}^{-1}$  and  $805\text{ cm}^{-1}$  due to N-H wag in pure DOX diminished in the FTIR spectrum of DOX-conjugated PVA-IO nanoparticles. From this FTIR result, it can be interpreted that attachment of DOX to the PVA-IO nanoparticles occurs via the

interaction of  $\text{-NH}_2$  and  $\text{-OH}$  groups of DOX with  $\text{-OH}$  groups of PVA through hydrogen bonding.

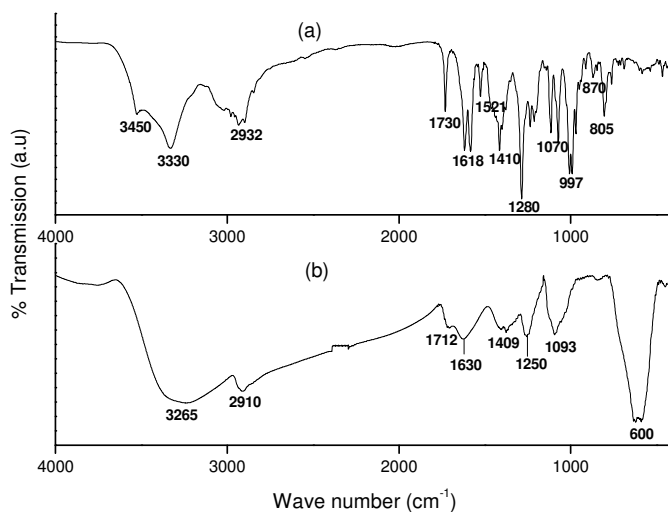


**Figure 4.21** FTIR spectra of (a) pure DOX and (b) DOX-conjugated PVA-IO nanoparticles. Conjugation of DOX to the PVA-IO nanoparticles occurs via the interaction of  $\text{-NH}_2$  and  $\text{-OH}$  groups of DOX with  $\text{-OH}$  groups of PVA.

When the PVA concentration increases (from 0.5 to 5 wt%), the number of surface active  $\text{-OH}$  group increases, which results in higher drug adsorption (Fig. 4.19). Considering the conjugation of DOX with the surface active hydroxyl group ( $\text{-OH}$ ) of PVA, there is increased binding of DOX with increasing PVA concentration, therefore, the drug is likely to be released at a slower rate from carriers with higher PVA content (Fig. 4.20). The drug release profiles follow the Fick's law of diffusion for monolithic system. In monolithic systems, the drug is uniformly dispersed in the polymer and it is released by diffusion from the polymer. In the case of monolithic system, if the drug release is

primarily controlled by diffusion through the carrier matrix, then the drug release can be calculated by following equation [286]:

$$\frac{M_t}{M_\infty} = 1 - \frac{6}{\pi^2} \sum_{n=1}^{\infty} \frac{1}{n^2} \exp\left(-\frac{Dn^2\pi^2t}{R_p^2}\right) \quad (4.1)$$

where  $M_t$  and  $M_\infty$  are the cumulative amounts of drug released at time  $t$  and infinity, respectively;  $n$  is a dummy variable,  $D$  is the diffusion coefficient of the drug and  $R_p$  is the particle size. In Eqn. 4.1, it is assumed that there is no significant change in the carrier matrix during drug release (e.g., constant porosity, no swelling, time-independent permeability of the drug) [286]. The curve fitting of DOX release profiles with Eqn. 4.1 shows that the DOX release from PVA-IO nanoparticles is a Fickian diffusion-controlled process. The diffusion coefficient ( $D$ ) of DOX ( $1.5 \times 10^{-18}$  cm<sup>2</sup>/s) is calculated from Eqn. 4.1, which is close to previous reports [287] ( $D$  of DOX for PEG-b-PCL and PEG-b-PLA is  $1.13 \times 10^{-18}$  cm<sup>2</sup>/s and  $1.82 \times 10^{-18}$  cm<sup>2</sup>/s, respectively).

Considering breast cancer, the required dosage of anti-cancer drug is calculated based on Mosteller equation [288] to find the BSA (body surface area). Mosteller equation is: BSA (m<sup>2</sup>) = [Height (cm)  $\times$  Weight (kg) / 3600]<sup>1/2</sup>. If a female patient of body weight of 55 kg and height of 165 cm, then her BSA is 1.59 m<sup>2</sup>. Generally, the treatment of DOX requires a dose of 50 mg/m<sup>2</sup> [289]. Therefore, the required dosage of DOX is (1.59 m<sup>2</sup>  $\times$  50 mg/m<sup>2</sup>) = 79.5 mg. The total body water (TBW) is calculated by Watson's formula : TBW = (-2.097) + [0.1069  $\times$  height (cm)] + [0.2466  $\times$  weight (kg)] [290]. So the total body water is 29.1 L. Therefore, the optimum DOX concentration should be 2.73  $\mu$ g /mL. In the present work, the optimum DOX concentration (2.73  $\mu$ g /mL) was released in 1 h.

Conjugation of drugs to hydrophilic polymers has been actively pursued to improve the pharmacological and pharmacokinetic properties of therapeutic drugs. In general, therapeutic drugs conjugated to polymers through cleavable covalent bonds have enhanced solubility, reduced toxicity and prolonged plasma circulation time compared to free drugs [291]. Polymers that have track records of preclinical success for conjugation of drug molecules include polyethyleneglycol (PEG) [292], N-2-hydroxypropylmethacrylamide (HPMA) copolymer [293-295], polyglutamate [296, 297], dextran [298-300]. Conjugates of various anti-cancer drugs with these polymers are currently in clinical trials [301].

PEG has been used for the conjugation and delivery of anti-cancer drugs such as paclitaxel [302], DOX [303] and camptothecin [304]. Conjugation of PEG to these drugs dramatically increases solubility and improves retention in circulation [303]. Enhanced antitumor efficacy in various preclinical studies [305, 306] and clinical studies [307] was observed with these PEG-drug conjugates. HPMA copolymers are water soluble and biocompatible [308]. HPMA-drug conjugates evaluated clinically include HPMA-paclitaxel [309], HPMA-camptothecin [310], HPMA-DOX [311] and HPMA-platinite [312]. Polyglutamates are a class of anionic polymers, which have a large number of pendant carboxylate groups to make them water soluble and high drug loading capacities [296, 313]. Rana *et al* reported the attachment of DOX with PMMA by amine ( $-NH_2$ ) group of DOX with  $-COOH$  group of PMMA in DOX-conjugated PMMA coated nickel ferrite nanoparticles [265]. Cavalieri *et al* reported hydrogel microparticles of methacrylate derivatized polyvinyl alcohol (PVA-MA) loaded with DOX and showed the cellular uptake of DOX by LoVo human colon carcinoma cells [314]. Orienti *et al* employed polymeric micelles of oleoyl conjugated polyvinyl alcohol (PVA-OL) to

encapsulate DOX and showed drug release activated by proteolytic enzyme pronase-E [315].

*In summary, Fe@Au nanoparticles attached to DOX by interaction of amine ( $-NH_2$ ) group of DOX with the Au shell, whereas the binding of DOX to the PVA-IO nanoparticles occurred via the interaction of  $-NH_2$  and  $-OH$  groups of DOX with  $-OH$  group of PVA through hydrogen bonding. Up to 25% and 45% of adsorbed drug was released from Fe@Au and PVA-IO nanoparticles, respectively.*

#### 4.4 *In-vitro* experimental targeting of MCP

An *in-vitro* apparatus simulating the human circulatory system was constructed to determine the retention of MCP under different flow rates of fluid at various distance of the magnet from the tube simulating the blood vessel. The retention of Fe@Au MCP (S-2 and S-3) at distances of 5, 10 and 15 mm away from the magnet surface with various flow rates of fluid ( $\bar{v} = 1$  to  $40 \text{ mm s}^{-1}$ ) is presented in Fig.4.22.

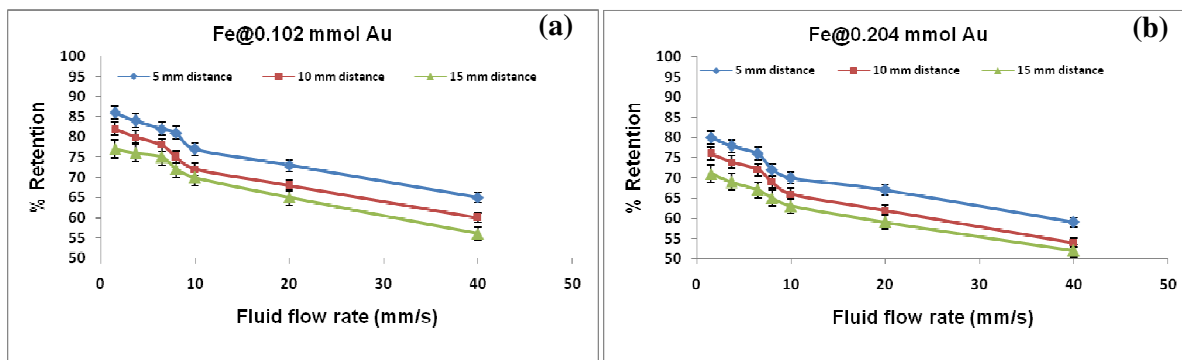


**Figure 4.22** Percent retention of (a) S-2 (0.102 mmol gold coated iron nanoparticles) and (b) S-3 (0.204 mmol gold coated iron nanoparticles) at various flow rates of fluid.

This *in-vitro* experimental study shows the capture of MCP within the fluidic system, simulating the flow regime encountered in diseased capillary blood vessels ( $\bar{v} = 1\text{-}10\text{ mm s}^{-1}$ ) [316]. The magnetic fields measured at 5, 10 and 15 mm distance from the magnet surface were 0.35, 0.22 and 0.12 T with field gradients of 25, 15 and  $8.5\text{ T m}^{-1}$ , respectively. As expected, the retention of MCP decreased with increasing flow rate of fluid and decreasing magnetic field gradients. The percentage retention of S-2 (Fe coated with  $0.102\text{ m mol Au}$ ) at field gradient of  $25\text{ T m}^{-1}$  was 86% for a flow rate of  $1\text{ mm s}^{-1}$ , the retention decreased to 65% for a flow rate of  $40\text{ mm s}^{-1}$  (Fig. 4.22.a). The maximum retention of S-2 at a flow rate of  $1\text{ mm s}^{-1}$  was found to be 82% and 77% for field gradients of 15 and  $8.5\text{ T m}^{-1}$ , respectively. Figure 4.22.b shows that the maximum retention of S-3 (Fe coated with  $0.204\text{ m mol Au}$ ) at a flow rate of  $1\text{ mm s}^{-1}$  was 80%, 76% and 71% for magnetic field gradients of 25, 15 and  $8.5\text{ T m}^{-1}$ , respectively. The difference in retention of S-2 and S-3 is due to the higher saturation magnetization of S-2 compared to S-3.

Figure 4.23 presents the percentage retention of uncoated  $\text{Fe}_3\text{O}_4$  (S-4) and PVA-IO (S-6, S-7 and S-8) at distances 5, 10 and 15 mm away from the magnet surface for various flow rates of fluid ( $\bar{v} = 1\text{ to }40\text{ mm s}^{-1}$ ).

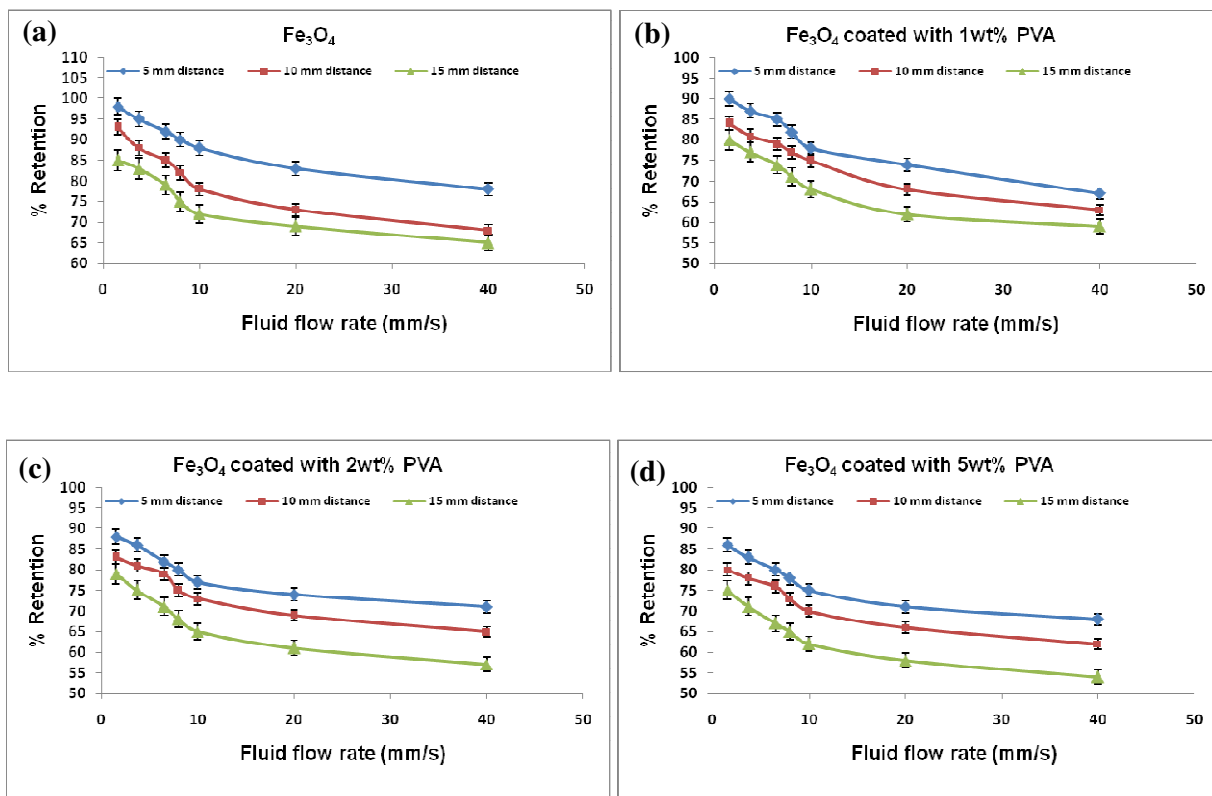


**Figure 4.23** Percent retention of (a) S-4 (uncoated  $\text{Fe}_3\text{O}_4$ ), (b) S-6 ( $\text{Fe}_3\text{O}_4$  coated with 1 wt% PVA), (c) S-7 ( $\text{Fe}_3\text{O}_4$  coated with 2 wt% PVA) and (d) S-8 ( $\text{Fe}_3\text{O}_4$  coated with 5 wt% PVA) at various flow rates of fluid.

The trend was found to be similar to the case as discussed earlier, the retention of MCP decreased with increasing flow rate of fluid and decreasing magnetic field gradients. The maximum retention at field gradient of  $25 \text{ T m}^{-1}$  and flow rate of  $1 \text{ mm s}^{-1}$  was found to be 98%, 90%, 88% and 86% for S-4, S-6, S-7 and S-8, respectively. This *in-vitro* study quantifies the extent of capture of MCP within the tumor, which is influenced by the magnetic field gradient, flow rate of fluid and magnetic properties of MCP.

There have been limited studies on the pharmacokinetic and biodistribution of gold coated magnetic nanoparticles [317]. Physicochemical properties of nanoparticles such as size, shape, morphology, charge and surface chemistry affect their pharmacokinetics and biodistribution. The size of the nanoparticles should be small enough to avoid immediate uptake by phagocytic cells of the reticulo-endothelial system (RES) and big enough to avoid rapid renal clearance. Very small particles (< 10 nm diameter) can easily pass through the capillary wall in the tumor but can easily be pushed out from the tumor by blood flow [318]. As the magnetic force acting on the magnetic particles is proportional to the volume of the particles, fluidic drag force can overcome the magnetic force experienced by the smaller particles. Therefore, small particles may have good permeability but poor retention. On the other hand, larger particles have higher magnetization and experience higher magnetic forces, which offer a higher chance of *in-vivo* trapping by an external magnetic field. This comes at the cost of circulation time since larger particles are likely to be opsonized earlier. Various particle sizes have been successfully used in clinical trials and *in-vivo* trials with animals, e.g., the average size of 100 nm for magnetic drug targeting [44], and a size range of 100-200 nm in animal trials [319-321].

In addition to size, surface charge plays a critical role in blood circulation time of nanoparticles [322, 323]. Positively charged coatings nonspecifically stick to cells [322] whereas the negatively charged particle surface is taken up by liver due to sequestration by phagocytes [67]. Therefore, nanoparticles with a neutral surface experience extended blood circulation times.

Nanoparticles accumulate in target tissues through two mechanisms: passive targeting and active targeting. Passive targeting is the nonspecific accumulation of nanoparticles in

the cells of the reticuloendothelial systems (RES) or in the tumors owing to the innate physiological properties of these tissues. Most nanoparticles are rapidly recognized as foreign and are taken up by the liver and the spleen after they are introduced into the body. On the other hand, to direct nanoparticles to organs other than the liver and the spleen, it is highly desirable that they avoid RES uptake and thus have a prolonged blood circulating time [324]. Long-circulating nanoparticles have shown increased accumulation in tumors due to an enhanced permeability and retention (EPR) effect, a phenomenon attributed to leaky tumor vasculature and impaired lymphatic drainage system in the tumors [325].

Since passive diffusion of the nanoparticle to tumors is dominated by the pore cutoff size of tumor blood vessels, smaller nanoparticles have an advantage in crossing the tumor vessel wall. This is particularly true for tumors such as glioma (brain cancer) and ovarian cancer that have a small pore cutoff size of 7–100 nm [326]. The surface coating is another factor that greatly affects the pharmacokinetics and biodistribution of nanoparticles. Plasma proteins in blood are adsorbed onto the surface of nanoparticles [327]. However, coating with hydrophilic polymers results in higher *in-vivo* circulation time upon systemic injection, e.g., gold nanostructures coated with poly(ethylene glycol) (PEG) [328]. After intravenous injection into rats, various coatings, such as PEG, are found to minimize nonspecific adsorption of plasma proteins onto nanoparticles and to reduce their uptake by the liver [329]. Qian *et al* described the use of PEGylated gold nanoparticles for *in-vivo* tumor targeting and molecular imaging based on their surface-enhanced Raman scattering effect [330].

---

*In summary, the capture efficiency of MCP within the tumor depends on the magnetic field gradient, flow rate of fluid and magnetic properties of MCP. A high percentage of MCP can be captured, e.g., 90% of PVA-IO and 86% of Fe@Au nanoparticles can be retained for a magnetic field gradient of  $25 \text{ T m}^{-1}$  and flow rate of  $1 \text{ mm s}^{-1}$ .*

#### **4.5 Modelling of targeting MCP**

A model was developed to examine the transport and capture of MCP in the tumor vasculature by an externally applied magnetic field generated by a permanent magnet. First, trajectories of MCP were calculated by solving the equations of motion (Eqn. 3.20 and 3.21) followed by the parametric analysis of distance of capture (d) for magnetic drug targeting as a function of variables such as size of MCP, magnetic properties of MCP and blood flow rate. Finally, CFD simulations were performed, which qualitatively supported the deposition efficiency trend found in the experimental results.

### 4.5.1 Model Parameters

A list of the parameters used in the 2-D model is given in Table 4.6.

**Table 4.6** Parameters used in modelling and simulations.

Properties	Symbol	Units	Value
Width of rectangular magnet	$2w$	mm	50
Height of rectangular magnet	$2h$	mm	100
Diameter of cylindrical magnet	$2R_{\text{mag}}$	mm	60
Magnetization of Nd-Fe-B magnet	$M_s$	$\text{A.m}^{-1}$	$10^6$
Length of the channel	$L$	mm	100
Height of the channel	$2R$	mm	1
Particle size	$R_p$	nm	100, 200, 500, 1000
Susceptibility of magnetic particle	$\chi$		0.4
Flow rate of fluid	$v$	$\text{mm s}^{-1}$	1, 5, 10, 40
Density of ferrofluid	$\rho$	$\text{kg m}^{-3}$	800
Viscosity of ferrofluid	$\eta$	$\text{N s m}^{-2}$	$1.2 \times 10^{-3}$
Permeability of vacuum	$\mu_0$	$\text{T m A}^{-1}$	$4\pi \times 10^{-7}$

### 4.5.2 Magnetic Field Components

Figure 4.24 shows the variation in  $\nabla H_x^2$  and  $\nabla H_y^2$  (calculated from Eqns. 3.5, 3.6, 3.7 and 3.8) across the dimensionless length ( $x/L$ ) of the vessel. The curves in Figs. 4.24.a and 4.24.b depict the profiles for rectangular and cylindrical magnet, respectively.

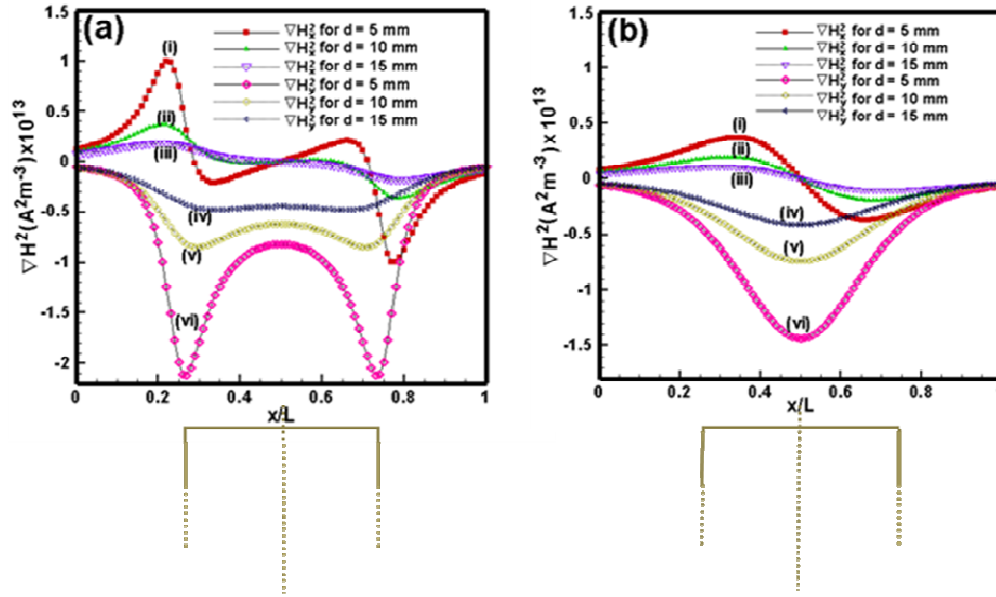


**Figure 4.24**  $\nabla H^2$  components of (a) Nd-Fe-B rectangular permanent magnet and (b) Nd-Fe-B cylindrical permanent magnet along the axis of vessel, when the vessel is at a distance of 5, 10 and 15 mm from the surface of magnet.

The  $\nabla H_x^2$  plots [curves (i) - (iii)] indicate that upstream to the magnet the magnitude of the force field ( $|\nabla H_x^2|$ ) gradually increases and downstream it progressively decreases.

The y-component gradients  $\nabla H_y^2$  [curves (iv) - (vi)] creates a gradient of magnetic force in the -y direction, which moves the MCP towards the magnet. These curves also show that  $\nabla H_y^2$  decays sharply away from the magnet towards the inlet and outlet of the

vessel. In the case of rectangular magnet [curves (iv) - (vi) in Fig. 4.24.a] the force-component is maximum near the corners of the rectangular magnet.

In contrast,  $\nabla H_y^2$  is maximum near the centre of the cylindrical magnet [curves (iv) - (vi) in Fig. 4.24.b] and it decays again sharply away from the magnet. The plots also show that the magnitude of  $\nabla H_x^2$  and  $\nabla H_y^2$  decreases if the magnet is placed away from the vessel. The results obtained from Eqns. 3.5, 3.6, 3.7 and 3.8 were verified using the components of the magnetic field intensity (**H**) of the corresponding permanent magnet, by numerically solving the magnetostatic equation employing COMSOL multiphysics™,

$$\nabla \times \left( \frac{1}{\mu_0} \nabla \times \mathbf{A} - \mathbf{M} \right) = \mathbf{J} \quad (4.2)$$

Eqn. 4.2 is obtained by combining the Maxwell-Ampere equation ( $\nabla \times \mathbf{H} = \mathbf{J}$ ), Gauss equation ( $\nabla \cdot \mathbf{B} = 0$ ), the constitutive equation ( $\mathbf{B} = \mu_0 (\mathbf{M} + \mathbf{H})$ ) and the equation for magnetic vector potential ( $\mathbf{B} = \nabla \times \mathbf{A}$  and  $\nabla \cdot \mathbf{A} = 0$ ). Here **J**, **B**, **M** and **A** denote current density, magnetic flux density, magnetization, and magnetic vector potential, respectively. The magnetic insulation condition  $A_z = 0$  is employed at the boundaries to solve Eqn. 4.2. The analytical results plotted in Fig. 4.24 were validated against the numerical results obtained from COMSOL.

### 4.5.3 MCP trajectories

The trajectories of MCP were calculated in a blood vessel under the action of magnetic and fluidic drag forces. The representative plots of trajectories of  $\text{Fe}_3\text{O}_4$  MCP are presented in Fig. 4.25, these plots were obtained by solving Eqns. 3.20 and 3.21. In this analysis, an average flow velocity of fluid ( $\bar{v}$ ) = 5 mm s<sup>-1</sup> and d = 30 mm were assumed. The rectangular magnet parameters were used (Table 4.6).

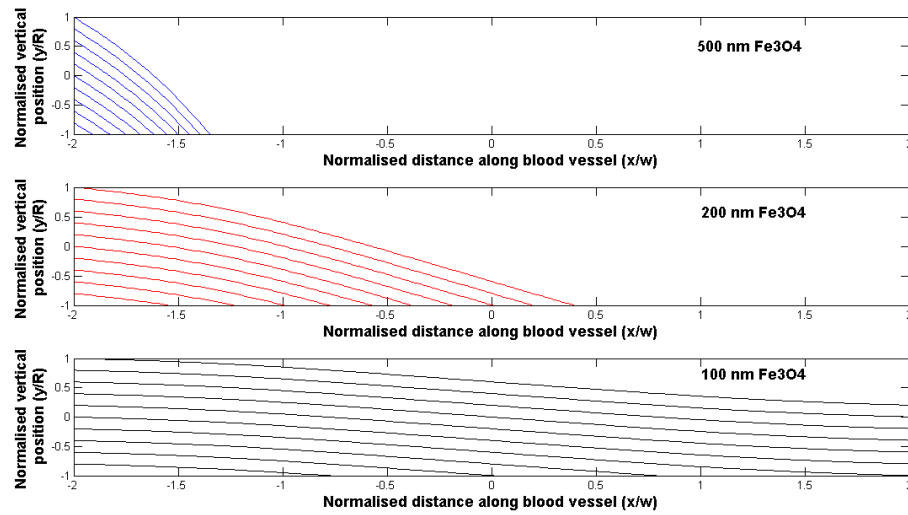


**Figure 4.25** Trajectories of  $\text{Fe}_3\text{O}_4$  MCP (particle size 100, 200 and 500 nm) in the vessel when ( $\bar{v}$ ) = 5 mm s<sup>-1</sup>, d = 30 mm.

The trajectories of  $\text{Fe}_3\text{O}_4$  MCP (100, 200 and 500 nm) were determined in the vessel. The radial position of MCP was normalised with respect to the vessel radius (R) and the axial position of MCP was normalised with respect to the width (w) of the magnet. The trajectories of  $\text{Fe}_3\text{O}_4$  MCP (500 and 200 nm) showed that all MCP were captured in the vessel. However, most of  $\text{Fe}_3\text{O}_4$  MCP of 100 nm size escaped capture (Fig. 4.25). The difference in trajectory behaviour of  $\text{Fe}_3\text{O}_4$  MCP in Fig. 4.25 is due the fact that the

magnetic force is proportional to the volume of the MCP, hence larger MCP experience a stronger capture force and can be captured easily.

The effect of magnetic properties of MCP on the trajectories is presented in Fig. 4.26.

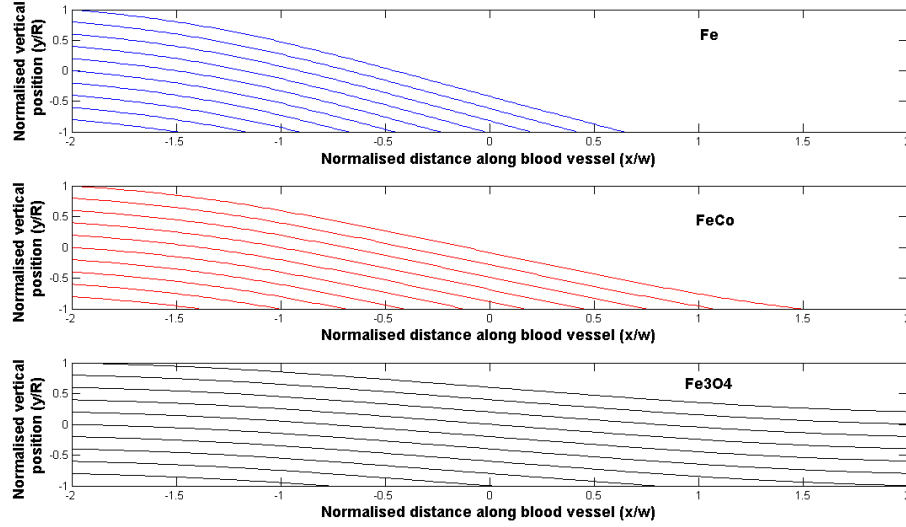


**Figure 4.26** Trajectories of different MCP of 100 nm size in the vessel when  $(\bar{v}) = 5$  mm s<sup>-1</sup>,  $d = 30$  mm.

In this calculation of the trajectories, Fe, FeCo, Fe<sub>3</sub>O<sub>4</sub> MCP with 100 nm size were considered, an average flow velocity of fluid  $(\bar{v})$  of 5 mm s<sup>-1</sup> and  $d$  of 30 mm were assumed. It was observed that all Fe and FeCo MCP were captured in the vessel, but most of Fe<sub>3</sub>O<sub>4</sub> MCP escaped capture. The difference in the trajectory behaviour of Fe, FeCo and Fe<sub>3</sub>O<sub>4</sub> MCP in Fig. 4.26 is attributed to the different magnetic properties of MCP. As the order of magnetization value is  $\text{Fe} > \text{FeCo} > \text{Fe}_3\text{O}_4$ , therefore, MCP with higher magnetization can be captured easily.

#### 4.5.4 Distance of Capture (d)

The optimum distance of magnet from the blood vessel to capture the MCP was determined from Eqn. 3.20 and 3.21. Figure 4.27 shows the representative plots of distance of capture (d) of various MCP as a function of their size for different flow rates of fluid (1, 5, 10 mm s<sup>-1</sup>).

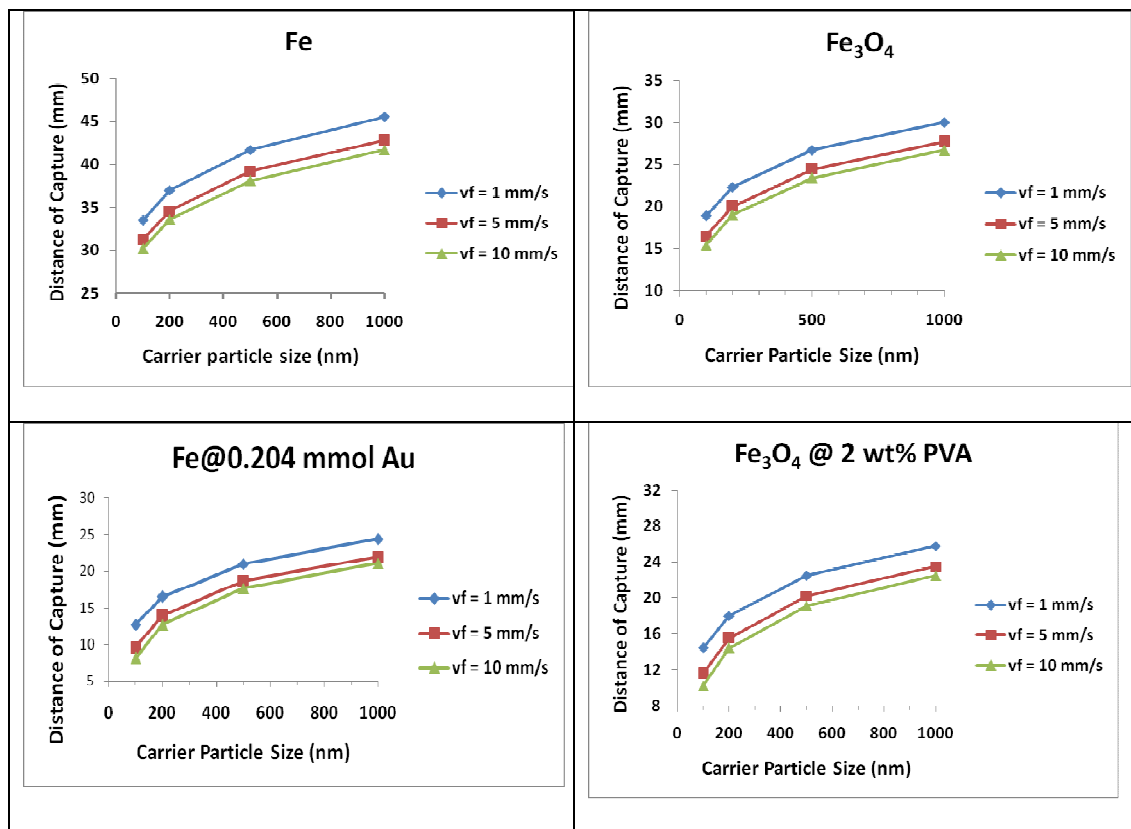


**Figure 4.27** Representative plots of distance of capture of various MCP as a function of MCP size for different flow rates of fluid.

From the Fig. 4.27, it is evident that as the MCP size increases, particles can be captured from further distance. For Fe particles at a given fluid flow rate of 5 mm s<sup>-1</sup>, the distance of capture of 100 and 1000 nm size was 31 and 43 mm, respectively. At the fluid velocity of 5 mm s<sup>-1</sup>, the distance of capture of 100 and 1000 nm size Fe@0.204 mol Au was 9.6

and 22 mm, and that of PVA-IO (2 wt% PVA coated) was 11.5 and 23.5 mm. The distance of capture decreased with increasing flow rate of fluid, e.g.,  $d$  is 34 and 30 mm at flow rates of 1 and 10 mm s<sup>-1</sup>, respectively for Fe particle (100 nm).

The distance of capture for various MCP with size of 100 nm at a given fluid flow rate (5 mm s<sup>-1</sup>) using a typical permanent magnet (field gradient of 25 T m<sup>-1</sup>) is presented in Fig. 4.28.

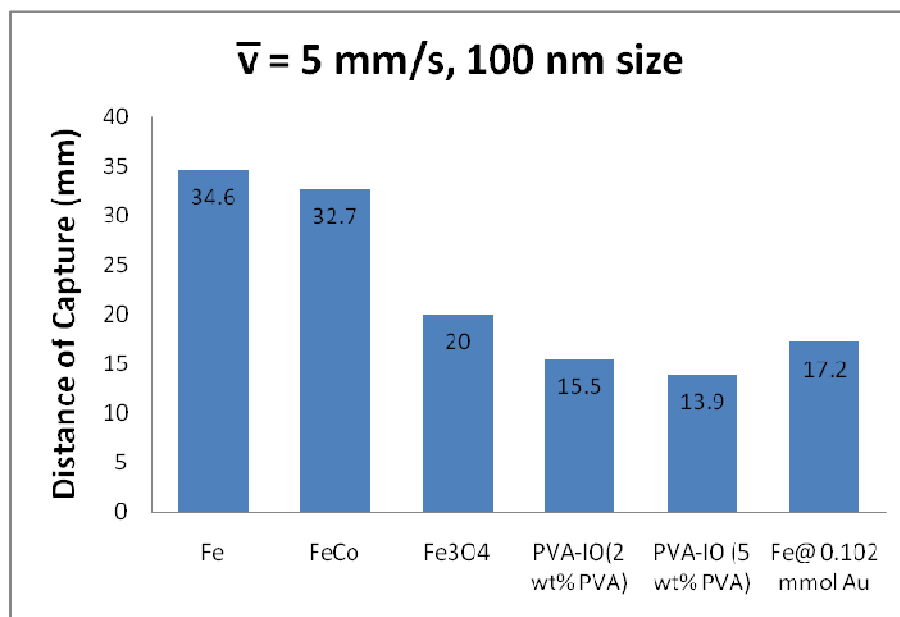


**Figure 4.28** Distance of capture for various MCP with size of 100 nm and  $\bar{v} = 5$  mm s<sup>-1</sup> using a typical permanent magnet.

From the results in Fig. 4.28, it can be concluded that in the context of drug targeting Fe<sub>3</sub>O<sub>4</sub>, Fe@Au, PVA-IO MCP (100 nm) can be targeted to the breast tumor and other skin tumors located in the hand, leg and neck by a typical permanent magnet. The average distances of internal organs such as lung, liver, kidney, pancreas from the skin are 20, 25, 30 and 32 mm, respectively [331, 332]. Therefore, Fe<sub>3</sub>O<sub>4</sub>, Fe@Au, PVA-IO MCP of 100 nm size are not suitable to be targeted to the tumors situated at lung, liver, kidney, pancreas by a typical permanent magnet. However, MCP with higher

magnetization such as Fe and FeCo (100 nm size) can be targeted to lung, liver, kidney, pancreas tumors using a typical permanent magnet.

Another approach to target MCP to the tumors situated deep inside the body is to use an external electromagnet, which can generate high magnetic field gradient. Alexiou *et al* designed an electromagnet of maximum field gradient of  $100 \text{ T m}^{-1}$  for magnetic drug targeting [333]. The distance of capture using a magnetic field gradient of  $100 \text{ T m}^{-1}$  was modelled for different sets of MCP for a particular size (100 nm) at a given fluid flow rate ( $5 \text{ mm s}^{-1}$ ), the results are shown in Fig. 4.29.

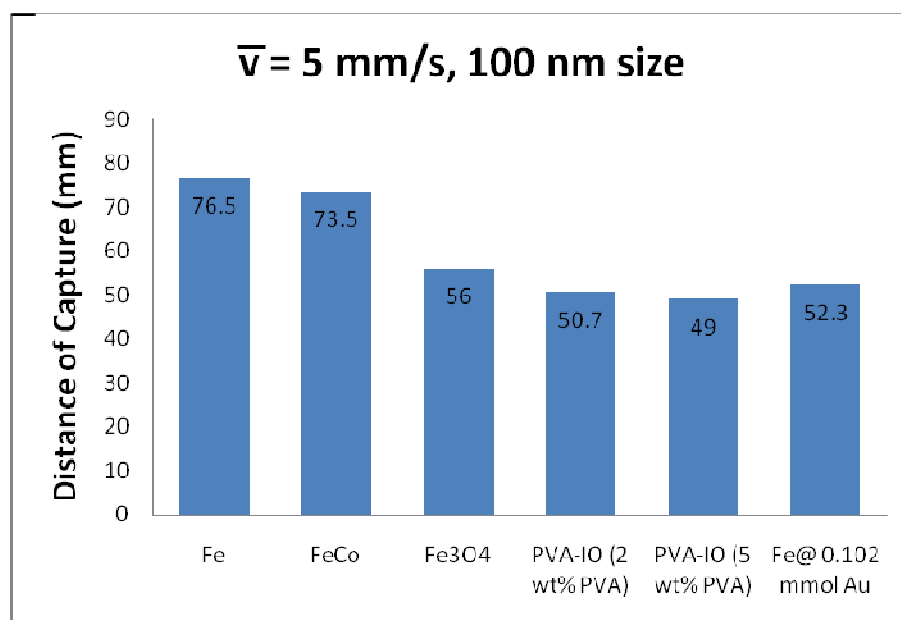


**Figure 4.29** Distance of capture for various MCP with size of 100 nm and  $\bar{v} = 5 \text{ mm.s}^{-1}$  using a higher magnetic field gradient ( $100 \text{ T m}^{-1}$ ).

From the Fig. 4.29, it can be concluded that Fe, FeCo, Fe<sub>3</sub>O<sub>4</sub>, Fe@Au, PVA-IO MCP (100 nm) can be targeted to the tumors situated at lung, liver, kidney, pancreas using a magnet of high magnetic field gradient.

---

#### 4.5.5 Numerical simulations

The success of magnetic drug targeting depends on the extent to which MCP can be deposited at the desired location. The following factors have a significant influence: (i) the distance between the injection point of MCP and the position of the tumor, (ii) size, and magnetic properties of MCP, (iii) magnetic field distribution and (iv) loss of drugs because of convective flow. The effect of convective and diffusive fluxes due to fluid flow on the deposition of MCP at the targeted location was studied. The results obtained from this study reveal the importance of optimizing the location for injection with respect to the magnetic field intensity. The study also emphasises the influence of size and magnetic properties of MCP. The trapping of MCP was studied using nonlinear CFD simulations.

Numerical simulations were performed to study the spatio-temporal evolution of the concentration profile of ferrofluid deposition in the vessel. The contours displayed in Fig. 4.30 are the spatio-temporal evolution of ferrofluid ( $R_p = 100$  nm and  $\chi = 0.4$ ) inside the vessel when  $\bar{v} = 10$  mm.s<sup>-1</sup> and  $d = 10$  mm.

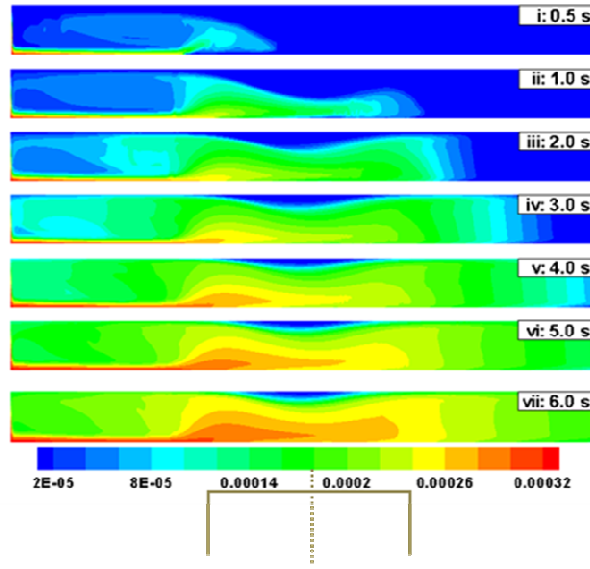


**Figure 4.30** Temporal evolution of the concentration profile when a ferrofluid ( $R_p = 100$  nm and  $\chi = 0.4$ ) is continuously injected at the inlet of a 2-D channel. Initially the vessel is assumed to be filled with a PBS buffer flowing at  $10 \text{ mm s}^{-1}$ . The centre of the magnet is placed at the mid point of the lateral coordinate. The vertical distance,  $d$  from the bottom wall of the vessel to surface of the magnet is 10 mm.

Frame (i) shows that ferrofluid enters through the inlet and moves towards the lower wall under the influence of the  $y$ -component of the applied magnetic force. In the flow domain, the magnetic field strength is weakest at the inlet and outlet because these two locations are farthest from the position of the magnet. The magnetic field gradient from the  $x$ -component of the magnetic field forces ferrofluid to creep along the bottom wall of the tube towards the centre of the tube where the magnet is placed [Frames (i) and (ii)]. As the ferrofluid reaches the place where the magnet is placed it encounters the weakest  $x$ -component force gradient and strongest  $y$ -component force gradient. Frame (iii) shows that the deposition rate of the ferrofluid near the magnet is significantly higher under such

condition. Frames (iv) to (vii) show that when ferrofluid starts deposition near the magnet, diffusive and convective forces spread the ferrofluid in the vertical and lateral direction of the vessel, respectively. The convective forces are particularly important in reducing deposition of ferrofluid near the magnet, making the ferrofluid flowing away from the targeted zone, especially in the downstream. Frames (iv) to (vii) also show that maximum deposition of particles takes place near the corners of the magnet where the y-component of the magnetic force is strongest. The contour plots confirm that there is ferrofluid deposition near the bottom wall and it is thickest in the region where the magnet is placed. This result is important for magnetic drug targeting, because it reveals that deposition is highest near the magnet and when the drug loaded MCP are injected and subjected to an external magnetic field, they creep along the wall of the blood vessels. Thus special care may be necessary to protect drugs from friction/adsorption with the wall before reaching the targeted location.

In Fig. 4.31 a comparison of the MCP deposition rate was presented when  $\bar{v}$  is varied from  $1 \text{ mm s}^{-1}$  to  $40 \text{ mm s}^{-1}$  and  $d$  is kept constant at  $10 \text{ mm}$ . Figs. 4.31.a to 4.31.c show that the mechanism of deposition remains the same as that described for Fig. 4.30, however, the time required to deposit MCP changes as  $\bar{v}$  is varied. For example, for  $d = 10 \text{ mm}$ , Fig. 4.31.a shows that when  $\bar{v} = 1 \text{ mm s}^{-1}$  deposition near the magnet at  $15 \text{ s}$  is similar to the case of (i) deposition at  $3 \text{ s}$  when  $\bar{v} = 10 \text{ mm s}^{-1}$  [Fig. 4.30, frame (iv)] or (ii) deposition at  $5 \text{ s}$  when  $\bar{v} = 5 \text{ mm s}^{-1}$  [Fig. 4.31.b, frame (vi)]. Thus, as the flow rate is reduced the rate of deposition is higher due to lower loss of ferrofluid through the outlet. This is in accordance with the experimental results presented in Fig. 4.23.

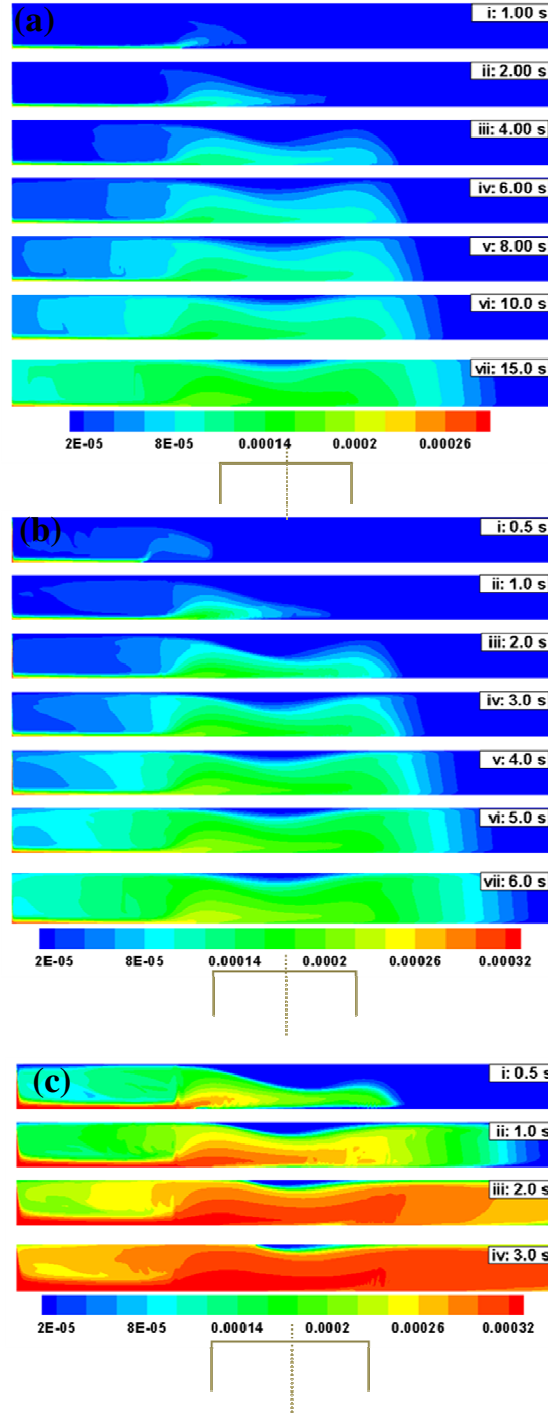


**Figure 4.31** Temporal evolution of the concentration profile when a ferrofluid ( $R_p=100$  nm and  $\chi = 0.4$ ) is continuously injected at the inlet of a 2-D channel. In this simulation  $d$  is kept constant at 10 mm. The contour plots represent: (a)  $\bar{v} = 1 \text{ mm s}^{-1}$ , (b)  $\bar{v} = 5 \text{ mm s}^{-1}$ , and (c)  $\bar{v} = 40 \text{ mm.s}^{-1}$ .

The simulations in the Figs. 4.30 and 4.31 suggest that the time of exposure of magnetic field can be optimized once the diameter of the blood vessel and blood flow rate is known. For example, Fig. 4.31.c shows that when  $\bar{v} = 40 \text{ mm s}^{-1}$  and  $d = 10 \text{ mm}$ , 0.5 to 1.0 s exposure is sufficient for significant MCP deposition. Thereafter, dispersion of MCP along and across the vessel leads to loss of MCP from the targeted location.

The magnetic field gradient is another very useful parameter, which is decreased with increasing distance of the magnet from the vessel. For example, when  $\bar{v} = 10 \text{ mm s}^{-1}$  and  $d = 5 \text{ mm}$ , the rectangular magnet ensures higher deposition near the corners (Fig. 4.32.a). However, a weaker magnetic field ( $\bar{v} = 10 \text{ mm s}^{-1}$  and  $d = 15 \text{ mm}$ ) leads to early dispersion of ferrofluid and its loss from the outlet because now convective effect dominates over the magnetic effect (Fig. 4.32.b). The effect of magnetic force can also be changed by varying the size of the MCP. Fig. 4.32.c shows that for larger MCP (200 nm), high and smooth deposition can be expected near the magnet within 1.0 s when  $\bar{v} = 10 \text{ mm s}^{-1}$  and  $d = 10 \text{ mm}$ . In Fig. 4.30, we can achieve similar deposition near the targeted zone only after 2.0 s with a particle size of 100 nm.

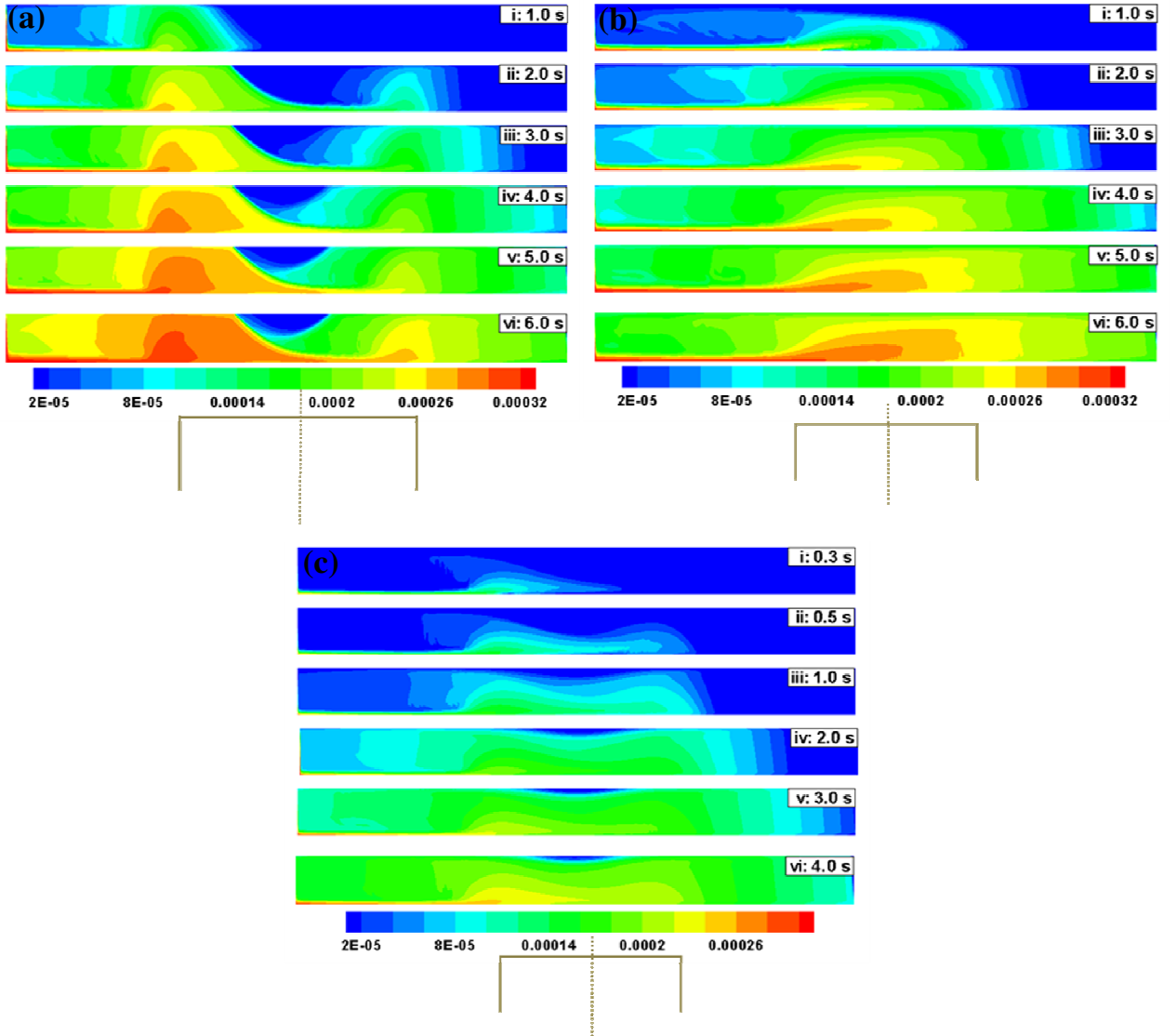


**Figure 4.32** Temporal evolution of the concentration profile when a ferrofluid ( $\bar{v} = 10 \text{ mm s}^{-1}$ ) is continuously injected at the inlet of a 2-D channel. In this contour plots: (a)  $d = 5 \text{ mm}$ ,  $R_p = 100 \text{ nm}$  and  $\chi = 0.4$ ; (b)  $d = 15 \text{ mm}$ ,  $R_p = 100 \text{ nm}$  and  $\chi = 0.4$ ; (c)  $d = 10 \text{ mm}$ ,  $R_p = 200 \text{ nm}$  and  $\chi = 0.4$ .

Interestingly, a very weak magnetic field can also lead to change in the flow mechanism (Fig. 4.33). Fig. 4.33.a shows the temporal evolution of ferrofluid ( $R_p=100$  nm and  $\chi=0.4$ ), when  $\bar{v} = 10$  mm s<sup>-1</sup> and  $d = 50$  mm.

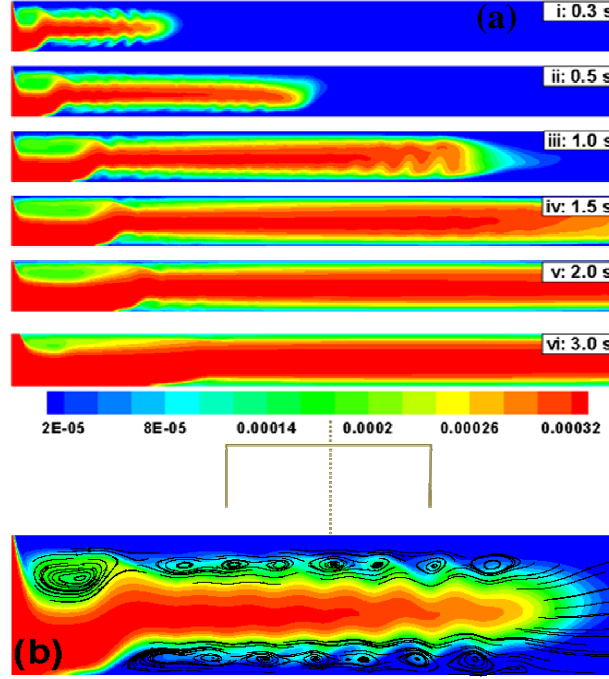


**Figure 4.33** (a) Temporal evolution of the concentration profile when a ferrofluid ( $R_p=100$  nm and  $\chi = 0.4$ ) is continuously injected at the inlet of a 2-D channel at flow rate ( $\bar{v}$ ) of 10 mm s<sup>-1</sup> under weak magnetic field ( $d = 50$  mm). (b) The streamline contour plot of frame (i) in magnified view shows the trade off between the magnetic force and the convective force leading to the formation of vortices near the wall.

Frame (i) in Fig. 4.33.a shows that the magnetic field initially directs the ferrofluid to move towards the bottom wall, however, convective force takes over quickly. Consequently, the ferrofluid dislodges from the bottom wall and flows through the central portion of the vessel. The streamlines shown in the magnified view (Fig. 4.33.b) indicate that the competition between magnetic and convective forces leads to formation

of vortices near the wall reducing the movement of ferrofluid towards the wall. Frames (ii) to (vi) in Fig. 4.33.a show that at later stages the magnetic field directs ferrofluid to touch the lower wall near the inlet but most of the ferrofluid passes through the central part of the tube to the downstream. The flow in the downstream is similar to the flow in a 2-D channel in the absence of a magnetic field. Hence the magnetic field strength and respective convective forces due to flow of the fluid has to be optimized to maximize MCP deposition.

Figure 4.34 shows the effect of magnet shape in magnetic drug targeting. A cylindrical magnet shows that deposition of MCP is maximum near the centre of the magnet. Figures 4.34.a, 4.34.b and 4.34.c show the spatio-temporal evolution of ferrofluid in the vessel when  $d = 10$  mm and flow rate is varied ( $\bar{v} = 1 \text{ mm s}^{-1}$ ,  $10 \text{ mm s}^{-1}$ , and  $40 \text{ mm s}^{-1}$ , respectively). Deposition is maximum near the centre of the magnet (Fig. 4.34.a) because the magnetic force is maximum at the centre of the cylindrical magnet (Fig. 4.24.b). This is in contrast to the case of a rectangular magnet where the magnetic force is maximum at the corners. However, the change of deposition with the change in flow rate is similar to the case of a rectangular magnet.

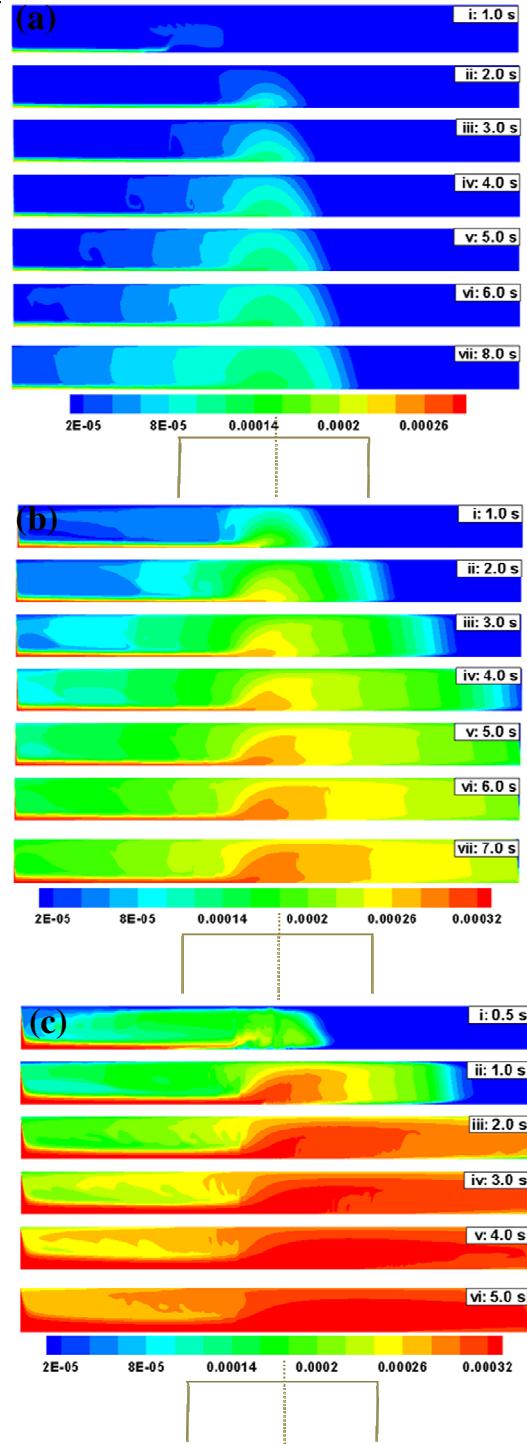


**Figure 4.34** Temporal evolution of the concentration profile of a ferrofluid ( $R_p = 100$  nm and  $\chi = 0.4$ ) in a 2-D channel under the influence of a cylindrical magnet ( $d = 10$  mm). The contour plots represent: (a)  $\bar{v} = 1 \text{ mm.s}^{-1}$ , (b)  $\bar{v} = 10 \text{ mm.s}^{-1}$ , and (c)  $\bar{v} = 40 \text{ mm.s}^{-1}$ .

Several researchers have studied the magnetic drug targeting. In previous studies, it was reported that a magnetic field of 0.8 T is sufficient to exceed linear blood flow in the intratumoral vasculature to localize magnetic carriers [22]. Lubbe *et al* studied the targeting of ferrofluid containing starch coated iron oxide nanoparticles (100 nm) loaded with mitoxantrone anti-cancer drug using a permanent magnet (0.5 T) in animal model [60]. Clinical trials in human patients using magnetic drug targeting (0.8 T) were conducted by Lubbe *et al* using anti-cancer drug epirubicin attached to starch coated iron oxide nanoparticles in form of ferrofluid (100 nm) and demonstrated that the infusion of ferrofluid was well tolerated by patients [44, 45]. Goodwin *et al* used magnetic carriers (0.5-5  $\mu\text{m}$ ) for drug targeting at the liver and lungs (8-12 cm) in the swine model using a permanent magnet (0.1 T) [94]. Preliminary investigations of the hydrodynamics of drug targeting suggest that a magnetic field of 0.2 T with field gradient of  $8 \text{ T m}^{-1}$  is sufficient to target magnetic nanoparticle carriers in femoral arteries [95].

In this work, a Nd-Fe-B permanent magnet was used for targeting of MCP, magnetic field generated by this magnet was 0.45 T with field gradient of  $25 \text{ T m}^{-1}$ , which is comparable to previous reports [44, 45, 60]. A high percentage of MCP could be captured (90% of PVA-IO and 86% of Fe@Au) by this magnet for fluid flow rate of  $1 \text{ mm s}^{-1}$ .

In previous modelling of magnetic drug targeting, Furlani *et al* derived an analytical expression of a cylindrical magnet to calculate the trajectories of magnetic particles and proposed a parametric analysis of magnetic targeting as a function of parameters such as the carrier particle size, properties and volume fraction of the embedded magnetic nanoparticles, properties of the magnet and blood flow rate [97, 98]. Rotariu *et al* used computer simulation of magnetic field of different magnetic configurations such as cylindrical magnet, magnetic circuit with parabolic shape confocal poles and needle

magnet to determine the trajectories of magnetic particles within tumor microvasculature [99]. Another model has been reported to optimize the necessary magnetic field by simulating the magnetic particle's trajectory [100]. A CFD analysis was used for Y-shaped model flow system of blood vessel and the capture efficiency of magnetic particles was determined [101]. Analysis of magnetically induced localization of the ferrofluid at a targeted region was also reported, it was shown that ferrofluid accumulation behaved as a solid obstacle in the flow [102]. Li *et al* simulated the streamlines and contours of concentration of a ferrofluid in a vessel and showed that particle accumulation was affected by the magnetic property of the particles, magnetic field strength and gradient as well as fluid flow rate [103].

In this work, the modelling of MCP targeting was performed by solving the equation of motion considering magnetic and fluidic forces. The trajectories of MCP as a function of flow rate of fluid, magnetic property of MCP and size of MCP were determined; the results are consistent with previous reports [97, 98]. Further, the optimum distance of capture of various MCP as a function of flow rate of fluid, magnetic property of MCP and size of MCP were determined in this work to establish the parameters for effective magnetic drug targeting, which was not reported earlier. The finer features of MCP deposition as well as the factors influencing capture efficiency of MCP using CFD simulations were studied, which is comparable to previous report [103]. The simulations show that the capture efficiency is dependent on the magnetic properties and size of MCP and that creep of MCP, convection and diffusion effects influence the efficacy of magnetic drug targeting. CFD simulations qualitatively support the deposition efficiency trend found in the experiments.

*In summary,  $Fe_3O_4$ ,  $Fe@Au$ , PVA-IO MCP (100 nm) are best suitable for targeting to the breast tumor and other skin tumor by a typical permanent magnet. Fe and FeCo*

---

*MCP or higher magnetic field gradient ( $100 \text{ T m}^{-1}$ ) are useful for targeting tumors situated deep inside the body. The creeping of ferrofluid along the wall of blood vessel suggests that drug injection should be as close as possible to the tumor.*

## Chapter 5

### Conclusions and Future Work

This chapter lists the significant findings of the present work and the scope of future work which could be made by utilizing the results obtained in this work.

#### 5.1 Conclusions

The delivery of anti-cancer drugs to specific target sites with minimum side effects is a challenge in conventional cancer treatments. Magnetically targeted drug delivery system using MCP targeted by an external magnetic field is a promising alternative to avoid several issues associated with conventional cancer therapies. In the present work, the synthesis, characterization and property evaluation of coated MCP with an experimental and modelling study of the efficacy with which these particles can be retained in the tumor were investigated. These MCP were extensively characterized using TEM, VSM, XRD, TGA, XPS, FTIR and DLS. MCP were loaded with anti-cancer drug DOX, drug loading and release properties were studied. An *in-vitro* apparatus simulating the human circulatory system was constructed and used to determine the retention of MCP under various flow rates of fluid and varying the magnetic field gradients. A time dependent CFD modelling of MCP deposition was carried out by Ansys-Fluent. The conclusions of this work are summarized:

- Gold coated iron (Fe@Au) nanoparticles (15 nm) were synthesized by the reverse micelle technique with sodium borohydride reduction of ferrous sulphate and

---

HAuCl<sub>4</sub> using CTAB as surfactant, n-butanol as co-surfactant and octane as oil phase.

- Pure iron (Fe) nanoparticles are oxidized to iron oxide. This oxidation of Fe can be minimized by coating with gold (Au), which also provides biocompatibility, useful surface chemistry and biological reactivity. Fe@Au nanoparticles exhibited superparamagnetic character having decreasing saturation magnetization with increasing Au coating. Since gold is a diamagnetic material, interparticle coupling between iron and gold decreases the magnetic properties of the coated nanoparticles.
- Fe@Au nanoparticles attached to DOX by the interaction of amine (–NH<sub>2</sub>) group of DOX with Au, as evidenced by the peak broadening of N-H stretching vibrations of DOX-conjugated Fe@Au nanoparticles in FTIR spectra and red shifting of absorption band of gold colloid with addition of DOX in UV-visible spectra. A significant quantity of DOX was loaded (94%) by the Fe@Au nanoparticles and up to 25% of adsorbed DOX was released.
- PVA-IO nanoparticles of average size 14 nm (SD 3) were synthesized by the co-precipitation of iron oxide followed by coating with different weight percentage of PVA solution. Up to 23% of PVA was attached to iron oxide nanoparticles as determined by TGA. This attachment of PVA to iron oxide nanoparticles occurred via hydrogen bonding between hydroxyl group of PVA and protonated surface of the oxide.
- The crystal structure of the magnetic core in PVA-IO was magnetite. There was a broadening of XRD peaks with an increase in PVA concentration, due to decrease in crystallite size.

- 
- PVA-IO nanoparticles were superparamagnetic with decreasing  $M_s$  with increasing PVA concentration. This is due to the dilution effect from adsorbed water and the hydroxyl content of PVA.
  - In the context of drug delivery, superparamagnetic nanoparticles (both Fe@Au and PVA-IO) are useful as they do not retain magnetization before and after exposure to an external magnetic field, reducing the probability of particle aggregation due to magnetic dipole interaction.
  - The attachment of DOX to the PVA-IO nanoparticles occurred via the interaction of  $-NH_2$  and  $-OH$  groups of DOX with  $-OH$  group of PVA through hydrogen bonding as evidenced by FTIR spectra. Up to 60% of DOX was loaded with PVA-IO nanoparticles and 45% of adsorbed drug was released. The drug release profiles followed the Fick's law of diffusion with diffusion coefficient (D) of  $1.5 \times 10^{-18} \text{ cm}^2 \cdot \text{s}^{-1}$ .
  - The *in-vitro* experimental targeting of MCP shows that a high percentage of MCP could be captured. e.g., 90% of PVA-IO and 86% of Fe@Au MCP were captured at a field gradient of  $25 \text{ T m}^{-1}$  and flow rate of  $1 \text{ mm s}^{-1}$ .
  - The modelling results of trajectories of MCP show that it is easier to capture particles with higher saturation magnetization and larger size at low flow rate of fluid. The calculation of distance of capture from the modelling predicts that  $Fe_3O_4$ , Fe@Au, PVA-IO MCP (100 nm) are best suitable for targeting to the breast tumor and other skin tumor located in hand, leg, neck by a typical permanent magnet. In order to target tumors situated deep inside the body, MCP with higher saturation magnetization such as Fe and FeCo or an external magnet with higher magnetic field gradient must be chosen.
-

- 
- The simulations of CFD model show that for a given magnetic field strength, the time of exposure to the magnetic field can be optimized once the diameter of the blood vessel and blood flow rate are known. Lower flow rate increases the time required for magnetic field exposure, higher flow rate leads to larger loss of MCP due to dispersion of particles.
  - The magnetic field strength, the magnet shape, magnetic properties and size of the MCP significantly influence deposition rate. A weaker magnetic field leads to early dispersion of ferrofluid and its loss from the outlet since convective effect dominates over the magnetic effect. High and smooth deposition is found near the magnet within short time for larger MCP. Deposition is maximum near the centre of the cylindrical magnet and corners of the rectangular magnet.
  - CFD simulations show that the ferrofluid creeps along the bottom wall of the vessel under the influence of a magnetic field, this may cause friction leading to loss of coating and drug prior to reaching the tumor, hence drug injection should be as close as possible to the tumor.
  - In a very weak magnetic field, creep flow is absent and ferrofluid flows along the centre of the vessel, recirculation zones near the wall boundary hinder the movement of MCP back to the targeted region.

In summary, this work shows that Fe@Au and PVA-IO MCP have excellent potential for tumor targeted magnetic drug delivery, that the capture efficiency is dependent on the magnetic properties and size of MCP, blood flow rate, time of capture, and that convection and diffusion effects can significantly influence the capture efficiency of MCP for magnetically targeted drug delivery.

---

## 5.2 Future scope of work

This section presents the scope of future work which can be extended from this work. This present work provides a platform to further research in the area of magnetically targeted drug delivery.

- In this work, it was shown that Fe@Au nanoparticles are potential magnetic drug carriers for tumor targeted drug delivery in terms of drug loading (94%), drug release (25%) and drug targeting (86%). This work can be extended to study the photothermal therapy of Fe@Au nanoparticles. As gold can be heated by near infrared (NIR) light irradiation; the resulting heat can destroy tumor cells, this modality of treatment is known as hyperthermia resulting from this photothermal effect [217-219]. Therefore, Fe@Au nanoparticles with different gold coating thickness can be synthesized, targeted to the tumor and then exposed to deep penetrating near infrared (NIR) laser to study the heating and therapeutic efficacy.
- In this work, the functionalization of magnetic iron oxide nanoparticles by PVA to conjugate with DOX was studied which shows that PVA coated iron oxide nanoparticles have great potential to be used in magnetically targeted drug delivery. This work can be extended by derivatization of PVA by phosphate group which improves stability and dispersability of magnetic nanoparticles [334]. Therefore, iron oxide can be coated with different polyvinyl alcohol phosphate (PVAP) and interaction of DOX with PVAP coated iron oxide MCP, DOX loading and release kinetics can be studied.
- In case of CFD simulations, a two-dimensional (2-D) model was employed, which helps in quick implementation of the magnetohydrodynamic formulation and provides results on the mechanism of deposition in the initial stages. The

---

experimental capture efficiency was compared to the results of this 2D model.

This work can be extended by considering a 3-D model, CFD simulations can be performed using this 3-D model to determine the deposition efficiency and compare these results quantitatively with the experimental observations.

---

## References

- [1] B. W. Stewart and P. Kleihues, World Cancer Report, (2003).
- [2] International Agency for Research on Cancer, <http://www-dep.iarc.fr/>.
- [3] D. M. Parkin, F. Bray, J. Ferlay and P. Pisani, Global cancer statistics 2002, *CA: Cancer Journal for Clinicians* 55 (2005), 74-108.
- [4] D. Hanahan and R. A. Weinberg, The hallmarks of cancer, *Cell* 100 (2000), 57-70.
- [5] R. J. Narayan, S. P. Adiga, M. J. Pellin, L. A. Curtiss, A. J. Hryn, S. Stafslie, B. Chisholm, C. C. Shih, C. M. Shih, S. J. Lin, Y. Y. Su, C. Jin, J. Zhang, N. A. Monteiro-Riviere and J. W. Elam, Atomic layer deposition-based functionalization of materials for medical and environmental health applications, *Philosophical Transactions of the Royal Society A: Mathematical, Physical and Engineering Sciences* 368 (2010), 2033-2064.
- [6] R. J. Narayan and R. Roeder, The development of novel materials for medical devices, *JOM Journal of the Minerals, Metals and Materials Society* 61 (2009), 13-13.
- [7] J. M. Wilkinson, Nanotechnology applications in medicine, *Medical Device Technology* 14 (2003), 29-31.
- [8] J. Panyam and V. Labhasetwar, Biodegradable nanoparticles for drug and gene delivery to cells and tissue, *Advanced Drug Delivery Review* 55 (2003), 329-347.
- [9] F. X. Gu, R. Karnik, A. Z. Wang, F. Alexis, E. Levy-Nissenbaum, S. Hong, R. S. Langer and O. C. Farokhzad, Targeted nanoparticles for cancer therapy, *Nano Today* 2 (2007), 14-21.
- [10] R. Singh and J. W. Lillard Jr, Nanoparticle-based targeted drug delivery, *Experimental and Molecular Pathology* 86 (2009), 215-223.

- 
- [11] D. Peer, J. M. Karp, S. Hong, O. C. Farokhzad, R. Margalit and R. Langer, Nanocarriers as an emerging platform for cancer therapy, *Nature Nanotechnology* 2 (2007), 751-760.
- [12] T. Lammers, W. E. Hennink and G. Storm, Tumour-targeted nanomedicines: principles and practice, *British Journal of Cancer* 99 (2008), 392-407.
- [13] O. C. Farokhzad and R. Langer, Impact of nanotechnology on drug delivery, *ACS Nano* 3 (2009), 16-20.
- [14] R. Jurgons, C. Seliger, A. Hilpert, L. Trahms, S. Odenbach and C. Alexiou, Drug loaded magnetic nanoparticles for cancer therapy, *Journal of Physics : Condensed Matter* 18 (2006), S2893-S2902.
- [15] M. Johannsen, U. Gneveckow, L. Eckelt, A. Feussner, N. Waldofner, R. Scholz, S. Deger, P. Wust, S. A. Loening and A. Jordan, Clinical hyperthermia of prostate cancer using magnetic nanoparticles: Presentation of a new interstitial technique, *International Journal of Hyperthermia* 21 (2005), 637-647.
- [16] C. H. Cunningham, T. Arai, P. C. Yang, M. V. McConnell, J. M. Pauly and S. M. Conolly, Positive Contrast Magnetic Resonance Imaging of Cells Labeled with Magnetic Nanoparticles, *Magnetic Resonance in Medicine* 53 (2005), 999-1005.
- [17] P. Tartaj, M. Del Puerto Morales, S. Veintemillas-Verdaguer, T. Gonzalez-Carreno and C. J. Serna, The preparation of magnetic nanoparticles for applications in biomedicine, *Journal of Physics D: Applied Physics* 36 (2003), R182-R197.
- [18] A. K. Gupta and M. Gupta, Synthesis and surface engineering of iron oxide nanoparticles for biomedical applications, *Biomaterials* 26 (2005), 3995-4021.
- [19] M. W. Freeman, A. Arrott and J. H. L. Watson, Magnetism in medicine, *Journal of Applied Physics* 31 (1960), S404-S405.
-

- 
- [20] S. Goodwin, C. Peterson, C. Hoh and C. Bittner, Targeting and retention of magnetic targeted carriers (MTCs) enhancing intra-arterial chemotherapy, *Journal of Magnetism and Magnetic Materials* 194 (1999), 132-139.
- [21] T. Neuberger, B. Schöpf, H. Hofmann, M. Hofmann and B. von Rechenberg, Superparamagnetic nanoparticles for biomedical applications: Possibilities and limitations of a new drug delivery system, *Journal of Magnetism and Magnetic Materials* 293 (2005), 483-496.
- [22] A. Senyei, K. Widder and G. Czerlinski, Magnetic guidance of drug-carrying microspheres, *Journal of Applied Physics* 49 (1978), 3578-3583.
- [23] Y. Zhang, N. Kohler and M. Zhang, Surface modification of superparamagnetic magnetite nanoparticles and their intracellular uptake, *Biomaterials* 23 (2002), 1553-1561.
- [24] P. Wust, B. Hildebrandt, G. Sreenivasa, B. Rau, J. Gellermann, H. Riess, R. Felix and P. M. Schlag, Hyperthermia in combined treatment of cancer, *The Lancet Oncology* 3 (2002), 487-497.
- [25] W. Andra, C. G. d'Ambly, R. Hergt, I. Hilger and W. A. Kaiser, Temperature distribution as function of time around a small spherical heat source of local magnetic hyperthermia, *Journal of Magnetism and Magnetic Materials* 194 (1999), 197-203.
- [26] A. Jordan, R. Scholz, P. Wust, H. Fahling and F. Roland, Magnetic fluid hyperthermia (MFH): Cancer treatment with AC magnetic field induced excitation of biocompatible superparamagnetic nanoparticles, *Journal of Magnetism and Magnetic Materials* 201 (1999), 413-419.
- [27] I. Hilger, R. Hergt and W. A. Kaiser, Effects of magnetic thermoablation in muscle tissue using iron oxide particles: An in vitro study, *Investigative Radiology* 35 (2000), 170-179.
-

- 
- [28] I. Coroiu, Relaxivities of different superparamagnetic particles for application in NMR tomography, *Journal of Magnetism and Magnetic Materials* 201 (1999), 449-452.
- [29] A. E. Merbach and E. Toth, *The chemistry of contrast agents in medical magnetic resonance imaging*, (2001), Wiley, Chichester.
- [30] D. K. Kim, Y. Zhang, J. Kehr, T. Klason, B. Bjelke and M. Muhammed, Characterisation and MRI study of surfactant coated superparamagnetic nanoparticles administered into the rat brain, *Journal of Magnetism and Magnetic Materials* 225 (2001), 256-261.
- [31] P. A. Liberti, C. G. Rao and L. W. M. M. Terstappen, Optimization of ferrofluids and protocols for the enrichment of breast tumor cells in blood, *Journal of Magnetism and Magnetic Materials* 225 (2001), 301-307.
- [32] F. Paul, D. Melville, S. Roath and D. Warhurst, A bench top magnetic separator for malarial parasite concentration, *IEEE Transactions on Magnetics* 17 (1981), 2822–2824.
- [33] N. Seesod, P. Nopparat, A. Hedrum, A. Holder, S. Thaithong, M. Uhlen and J. Lundeberg, An integrated system using immunomagnetic separation, polymerase chain reaction, and colorimetric detection for diagnosis of *Plasmodium Falciparum* *American Journal of Tropical Medicine and Hygiene* 56 (1997), 322-328.
- [34] S. Mornet, S. Vasseur, F. Grasset and E. Duguet, Magnetic nanoparticle design for medical diagnosis and therapy *Journal of Materials Chemistry* 14 (2004), 2161-2175.
- [35] G. P. Yan, L. Robinson and P. Hogg, Magnetic resonance imaging contrast agents: Overview and perspectives, *Radiography* 13 (2007), e5-e19.
- [36] C. Corot, P. Robert, J.-M. Idée and M. Port, Recent advances in iron oxide nanocrystal technology for medical imaging, *Advanced Drug Delivery Reviews* 58 (2006), 1471-1504.
-

- 
- [37] C. Alexiou, W. Arnold, R. J. Klein, F. G. Parak, P. Hulin, C. Bergemann, W. Erhardt, S. Wagenpfeil and A. S. Lubbe, Locoregional cancer treatment with magnetic drug targeting, *Cancer Research* 60 (2000), 6641-6648
- [38] C. Alexiou, R. Schmid, R. Jurgons, M. Kremer, G. Wanner, C. Bergemann, E. Huenges, T. Nawroth, W. Arnold and F. Parak, Targeting cancer cells: magnetic nanoparticles as drug carriers, *European Biophysics Journal* 35 (2006), 446-450.
- [39] R. V. Ramanujan, Magnetic particles for biomedical applications, In *Biomedical Materials*, R. Narayanan, ed., (2009), Springer.
- [40] American Cancer Society, [http://www.cancer.org/docroot/ETO/ETO\\_1.asp](http://www.cancer.org/docroot/ETO/ETO_1.asp).
- [41] P. Moroz, S. K. Jones and B. N. Gray, Magnetically mediated hyperthermia: current status and future directions, *International Journal of Hyperthermia* 18 (2002), 267-284.
- [42] C. L. Oudeck, A. H. Habib, P. Ohodnicki, K. Miller, C. A. Sawyer, P. Chaudhary, M. E. McHenry, Theory of magnetic fluid heating with an alternating magnetic field with temperature dependent materials properties for self-regulated heating, *Journal of Applied Physics* 105 (2009) 07B324.
- [43] J. A. Ritter, A. D. Ebner, K. D. Daniel and K. L. Stewart, Application of high gradient magnetic separation principles to magnetic drug targeting, *Journal of Magnetism and Magnetic Materials* 280 (2004), 184-201.
- [44] A. S. Lubbe, C. Bergemann, H. Riess, F. Schriever, P. Reichardt, K. Possinger, M. Matthias, B. Dorken, F. Herrmann, R. Gurtler, P. Hohenberger, N. Haas, R. Sohr, B. Sander, A.-J. Lemke, D. Ohlendorf, W. Huhnt and D. Huhn, Clinical Experiences with Magnetic Drug Targeting: A Phase I Study with 4'-Epidoxorubicin in 14 Patients with Advanced Solid Tumors, *Cancer Research* 56 (1996), 4686-4693.
-

- 
- [45] A. S. Lubbe, C. Alexiou and C. Bergemann, Clinical Applications of Magnetic Drug Targeting, *Journal of Surgical Research* 95 (2001), 200-206.
- [46] Q. A. Pankhurst, J. Connolly, S. K. Jones and J. Dobson, Applications of magnetic nanoparticles in biomedicine *Journal of Physics D: Applied Physics* 36 (2003), R167-181.
- [47] C. Alexiou, W. Arnold, R. J. Klein, F. G. Parak, P. Hulin, C. Bergemann, W. Erhardt, S. Wagenpfeil and A. S. Lubbe, Locoregional cancer treatment with magnetic drug targeting, *Cancer Research* 60 (2000), 6641-6648.
- [48] A. H. Habib, C. L. Oudeck, P. Chaudhary, M. R. Bockstaller and M. E. McHenry, Evaluation of iron-cobalt/ferrite core-shell nanoparticles for cancer thermotherapy, *Journal of Applied Physics*, 103 (2008) 07A307.
- [49] C. A. Sawyer, A. H. Habib, K. Miller, K. N. Collier, C. L. Oudeck and M. E. McHenry, Modeling of temperature profile during magnetic thermotherapy for cancer treatment, *Journal of Applied Physics*, 105 (2009) 07B320.
- [50] S. Purushotham, P. E. J. Chang, H. Rumpel, I. H. C. Kee, R. T. H. Ng, P. K. H. Chow, C. K. Tan and R. V. Ramanujan, Thermoresponsive core-shell magnetic nanoparticles for combined modalities of cancer therapy, *Nanotechnology* 20 (2009), 305101-305111.
- [51] S. Purushotham and R. V. Ramanujan, Thermoresponsive magnetic composite nanomaterials for multimodal cancer therapy, *Acta Biomaterialia* 6 (2010), 502-510.
- [52] T. F. Greten, F. Korangy, M. P. Manns and N. P. Malek, Molecular therapy for the treatment of hepatocellular carcinoma, *British Journal of Cancer* 100 (2009), 19-23.
- [53] S. Tanaka and S. Arai, Molecularly targeted therapy for hepatocellular carcinoma, *Cancer Science* 100 (2009), 1-8.
-

- 
- [54] S. Faivre, C. Dreyer, G. El Maalouf, M. P. Sablin and E. Raymond, Rationale for targeted therapies in hepatocellular carcinoma, *Targeted Oncology* 3 (2008), 81-85.
- [55] [www.biomagres.com](http://www.biomagres.com).
- [56] Y. X. J. Wang, S. M. Hussain and G. P. Krestin, Superparamagnetic iron oxide contrast agents: Physicochemical characteristics and applications in MR imaging, *European Radiology* 11 (2001), 2319-2331.
- [57] Y. Wang, Y. W. Ng, Y. Chen, B. Shuter, J. Yi, J. Ding, S. C. Wang and S. S. Feng, Formulation of superparamagnetic iron oxides by nanoparticles of biodegradable polymers for magnetic resonance Imaging, *Advanced Functional Materials* 18 (2008), 308-318.
- [58] M. G. Harisinghani, J. Barentsz, P. F. Hahn, W. M. Deserno, S. Tabatabaei, C. H. Van de Kaa, J. De la Rosette and R. Weissleder, Noninvasive detection of clinically occult lymph-node metastases in prostate cancer, *New England Journal of Medicine* 348 (2003), 2491-2499.
- [59] R. Weissleder, D. D. Stark, B. L. Engelstad, B. R. Bacon, C. C. Compton, D. L. White, P. Jacobs and J. Lewis, Superparamagnetic iron oxide: Pharmacokinetics and toxicity, *American Journal of Roentgenology* 152 (1989), 167-173.
- [60] A. S. Lubbe, C. Bergemann, W. Huhnt, T. Fricke, H. Riess, J. W. Brock and D. Huhn, Preclinical experiences with magnetic drug targeting: Tolerance and efficacy, *Cancer Research* 56 (1996), 4694-4701.
- [61] C. C. Berry and A. S. G. Curtis, Functionalization of magnetic nanoparticles for application in biomedicine, *Journal of Physics D: Applied Physics* 36 (2003), R198-R206.
- [62] S. M. Moghimi, A. C. Hunter and J. C. Murray, Long-circulating and target-specific nanoparticles: Theory to practice, *Pharmacological Reviews* 53 (2001), 283.
-

- 
- [63] U. Gaur, S. K. Sahoo, T. K. De, P. C. Ghosh, A. Maitra and P. K. Ghosh, Biodistribution of fluoresceinated dextran using novel nanoparticles evading reticuloendothelial system, *International Journal of Pharmaceutics* 202 (2000), 1-10.
- [64] S. Mohapatra, N. Pramanik, S. K. Ghosh and P. Pramanik, Synthesis and characterisation of ultrafine polyvinyl alcohol phosphate coated magnetic nanoparticles *Journal of Nanoscience and Nanotechnology* 6 (2006), 823-829.
- [65] A. Petri-Fink, M. Chastellain, L. Juillerat-Jeanneret, A. Ferrari and H. Hofmann, Development of functionalized superparamagnetic iron oxide nanoparticles for interaction with human cancer cells, *Biomaterials* 26 (2005), 2685-2694.
- [66] F. Cavalieri, E. Chiessi, R. Villa, L. Vigano, N. Zaffaroni, M. F. Telling and G. Paradossi, Novel PVA based hydrogel microparticles for doxorubicin delivery, *Biomacromolecules* 9 (2008), 1967-1973.
- [67] R. Shukla, V. Bansal, M. Chaudhary, A. Basu, R. R. Bhonde and M. Sastry, Biocompatibility of gold nanoparticles and their endocytotic fate inside the cellular compartment: A microscopic overview, *Langmuir* 21 (2005), 10644-10654.
- [68] V. Selvaraj and A. Muthukaruppan, Analytical detection and biological assay of antileukemic drug 5-fluorouracil using gold nanoparticles as probe, *International Journal of Pharmaceutics* 337 (2007), 275-281.
- [69] L. M. Demers, C. A. Mirkin, R. C. Mucic, R. A. Reynolds, R. L. Leitsinger and G. Viswanadham, A fluorescence-based method for determining the surface coverage and hybridization efficiency of thiol-capped oligonucleotides bound to gold thin films and nanoparticles, *Analytical Chemistry* 72 (2000), 5535-5541.
- [70] F. A. Fornari, J. K. Randolph, J. C. Yalowich, M. K. Ritke and D. A. Gewirtz, Interference by doxorubicin with DNA unwinding in MCF-7 breast tumor cells, *Molecular Pharmacology* 45 (1994), 649-656.
-

- 
- [71] K. M. Laginha, S. Verwoert, G. J. R. Charrois and T. M. Allen, Determination of doxorubicin levels in whole tumor and tumor nuclei in murine breast cancer tumors, *Clinical Cancer Research* 11 (2005), 6944-6949.
- [72] A. Gupta and S. Wells, Surface modified superparamagnetic nanoparticles for drug delivery: preparation, characterization and cytotoxicity studies, *IEEE Transaction on Nanobioscience* 3 (2004), 66-73.
- [73] A. K. Gupta and A. S. G. Curtis, Lactoferrin and ceruloplasmin derivatized superparamagnetic iron oxide nanoparticles for targeting cell surface receptors, *Biomaterials* 25 (2004), 3029-3040.
- [74] D. Jiles, *Introduction to Magnetism and Magnetic Materials*, (1991), Chapman and Hall, London.
- [75] A. H. Morrish, *The Physical Principles of Magnetism* (2001), IEEE Press, New York.
- [76] Q. A. Pankhurst, J. Connolly, S. K. Jones and J. Dobson, Applications of magnetic nanoparticles in biomedicine *Journal of Physics D: Applied Physics* 36 (2003), R167-R181.
- [77] C. Kittel, *Introduction to Solid State Physics*, no. 7th (1996), Wiley, New York.
- [78] D. Givord, Q. Lu and M. F. Rosignol, *Science and Technology of Nanostructured Materials*, (1991), Plenum Press, New York.
- [79] W. F. Brown, Thermal fluctuations of a single-domain particle, *Physical Review* 130 (1963), 1677–1686.
- [80] U. Zimmermann and G. Pilwat, Organ specific application of drugs by means of cellular capsule systems, *Journal of Bioscience* 31 c (1976), 732-736.
- [81] K. J. Widder, R. M. Morris, G. A. Poore, D. P. Howard and A. E. Senyei, Selective targeting of magnetic albumin microspheres containing low-dose
-

---

doxorubicin—total remission in Yoshida sarcoma-bearing rats, *European Journal of Cancer and Clinical Oncology* 19 (1983), 135–139.

[82] S. C. Goodwin, B. C. A, P. C. L and W. G, Single-dose toxicity study of hepatic intra-arterial infusion of doxorubicin coupled to a novel magnetically targeted drug carrier *Toxicological Sciences* 60 (2001), 177–183.

[83] A. S. Lubbe, C. Bergemann, J. Brock and D. G. McClure, Physiological aspects in magnetic drug-targeting, *Journal of Magnetism and Magnetic Materials* 194 (1999), 149-155.

[84] S. K. Pulfer and J. M. Gallo, Enhanced brain tumor selectivity of cationic magnetic polysaccharide microspheres *Journal of Drug Targeting* 6 (1999), 215–228.

[85] S. K. Pulfer, S. L. Ciccotto and J. M. Gallo, Distribution of small magnetic particles in brain tumor-bearing rats, *Journal of Neuro-Oncology* 41 (1999), 99–105.

[86] U. O. Hafeli, S. M. Sweeney, B. A. Beresford, E. H. Sim and R. M. Macklis, Magnetically directed poly(lactic acid) Y-microspheres: Novel agents for targeted intracavitary radiotherapy, *Journal of Biomedical Materials Research* 28 (1994), 901-908.

[87] U. O. Hafeli, S. M. Sweeney, B. A. Beresford, J. L. Humm and R. M. Macklis, Effective targeting of magnetic radioactive Y-microspheres to tumor cells by an externally applied magnetic field: Preliminary in vitro and in vivo results, *Nuclear Medicine and Biology* 22 (1995), 147-155.

[88] T. Kubo, T. Sugita, S. Shimose, Y. Nitta, Y. Ikuta and T. Murakami, Targeted delivery of anticancer drugs with intravenously administered magnetic liposomes in osteosarcoma-bearing hamsters *International Journal of Oncology* 17 (2000), 309–316.

- 
- [89] T. Kubo, T. Sugita, S. Shimose, Y. Nitta, Y. Ikuta and T. Murakami, Targeted systemic chemotherapy using magnetic liposomes with incorporated adriamycin for osteosarcoma in hamsters, *International Journal of Oncology* 18 (2001), 121–126.
- [90] O. Mykhaylyk, A. Cherchenko, A. Ilkin, N. Dudchenko, V. Ruditsa, M. Novoseletz and Y. Zozulya, Glial brain tumor targeting of magnetite nanoparticles in rats, *Journal of Magnetism and Magnetic Materials* 225 (2001), 241–247.
- [91] M. G. James, C. T. Hung, P. K. Gupta and G. P. Donald, Physiological pharmacokinetic model of adriamycin delivered via magnetic albumin microspheres in the rat, *Journal of Pharmacokinetics and Pharmacodynamics* V17 (1989), 305–326.
- [92] A. S. Lubbe, C. Bergemann, W. Huhnt, T. Fricke, H. Riess, J. W. Brock and D. Huhn, Preclinical experiences with magnetic drug targeting: Tolerance and efficacy, *Cancer Research* 56 (1996), 4694–4701.
- [93] M. W. Wilson, R. K. Kerlan, N. A. Fidelman, A. P. Venook, J. M. LaBerge, J. Koda and R. L. Gordon, Hepatocellular Carcinoma: Regional therapy with a magnetic targeted carrier bound to doxorubicin in a dual MR Imaging/ conventional angiography :initial experience with four patients, *Radiology* 230 (2004), 287–293.
- [94] S. Goodwin, C. Peterson, C. Hoh and C. Bittner, Targeting and retention of magnetic targeted carriers (MTCs) enhancing intra-arterial chemotherapy, *Journal of Magnetism and Magnetic Materials* 194 (1999), 132–139.
- [95] P. A. Voltairas, D. I. Fotiadis and L. K. Michalis, Hydrodynamics of magnetic drug targeting, *Journal of Biomechanics* 35 (2002), 813–821.
- [96] A. Grief and G. Richardson, Mathematical modelling of magnetically targeted drug delivery, *Journal of Magnetism and Magnetic Materials* 293 (2005), 455–463.
-

- 
- [97] E. J. Furlani and E. P. Furlani, A model for predicting magnetic targeting of multifunctional particles in the microvasculature, *Journal of Magnetism and Magnetic Materials* 312 (2007), 187-193.
- [98] E. P. Furlani and K. C. Ng, Analytical model of magnetic nanoparticle transport and capture in the microvasculature, *Physical Review E* 73 (2006), 061919.
- [99] O. Rotariu and N. J. C. Strachan, Modelling magnetic carrier particle targeting in the tumor microvasculature for cancer treatment, *Journal of Magnetism and Magnetic Materials* 293 (2005), 639-646.
- [100] B. Gleich, N. Hellwig, H. Bridell, R. Jurgons, C. Seliger, C. Alexiou, B. Wolf and T. Weyh, Design and evaluation of magnetic fields for nanoparticle drug targeting in cancer, *IEEE Transactions on Nanotechnology* 6 (2007), 164-170.
- [101] F. Mishima, S. Fujimoto, S. Takeda, Y. Izumi and S. Nishijima, Development of control system for magnetically targeted drug delivery, *Journal of Magnetism and Magnetic Materials* 310 (2007), 2883-2885.
- [102] R. Ganguly, A. P. Gaind, S. Sen and I. K. Puri, Analyzing ferrofluid transport for magnetic drug targeting, *Journal of Magnetism and Magnetic Materials* 289 (2005), 331-334.
- [103] X. L. Li, K. L. Yao and Z. L. Liu, CFD study on the magnetic fluid delivering in the vessel in high-gradient magnetic field, *Journal of Magnetism and Magnetic Materials* 320 (2008), 1753-1758.
- [104] J. W. M. Bulte and D. L. Kraitchman, Iron oxide MR contrast agents for molecular and cellular imaging, *NMR in Biomedicine* 17 (2004), 484-499.
- [105] B. Vincent, J. Edwards, S. Emmett and A. Jones, Depletion flocculation in dispersions of sterically-stabilised particles (soft spheres), *Colloids and Surfaces* 18 (1986), 261-281.
-

- 
- [106] B. V. Derjaguin and L. Landau, Theory of the stability of strongly charged lyophobic sols and of the adhesion of strongly charged particles in solutions of electrolytes, *Acta Physicochimica URSS* 14 (1941), 633-662.
- [107] E. J. W. Verwey and J. T. G. Overbeek, *Theory of the Stability of Lyophobic Colloids*, (1948) Elsevier Inc., Amsterdam.
- [108] R. M. Cornell and U. Schertmann, *Iron Oxides in the Laboratory: Preparation and Characterization*, (1991), WILEY-VCH, Weinheim.
- [109] Y. Sahoo, H. Pizem, T. Fried, D. Golodnitsky, L. Burstein, C. N. Sukenik and G. Markovich, Alkyl phosphonate/phosphate coating on magnetite nanoparticles: a comparison with fatty acids *Langmuir* 17 (2001), 7907-7911.
- [110] Y. Sahoo, A. Goodarzi, M. T. Swihart, T. Y. Ohulchanskyy, N. Kaur, E. P. Furlani and P. N. Prasad, Aqueous ferrofluid of magnetite nanoparticles: Fluorescence labeling and magnetophoretic control, *Journal of Physical Chemistry B* 109 (2005), 3879-3885.
- [111] M. Taupitz, S. Wagner, J. Schnorr, I. Kravec, H. Pilgrimm, H. Bergmann-Fritsch and B. Hamm, Phase I clinical evaluation of citrate-coated monocrystalline very small superparamagnetic iron oxide particles as a new contrast medium for magnetic resonance imaging, *Investigative Radiology* 39 (2004), 394-405.
- [112] N. Fauconnier, A. Bee, J. Roger and J. N. Pons, Adsorption of gluconic and citric acids on maghemite particles in aqueous medium, *Progress in Colloid and Polymer Science* 100 (1996), 212-216.
- [113] N. Fauconnier, J. N. Pons, J. Roger and A. Bee, Thiolation of maghemite nanoparticles by dimercaptosuccinic acid, *Journal of Colloid and Interface Science* 194 (1997), 427-433.
-

- 
- [114] D. Portet, B. Denizot, E. Rump, J. J. LeJeune and P. Jallet, Nonpolymeric coatings of iron oxide colloids for biological use as magnetic resonance imaging contrast agents, *Journal of Colloid and Interface Science* 238 (2001), 37-42.
- [115] P. H. Mutin, G. Guerrero and A. Vioux, Organic-inorganic hybrid materials based on organophosphorus coupling molecules: from metal phosphonates to surface modification of oxides, *Comptes Rendus Chimie* 6 (2003), 1153-1164.
- [116] D. I. Kreller, G. Gibson, W. Novak, G. W. Van Loon and J. Hugh Horton, Competitive adsorption of phosphate and carboxylate with natural organic matter on hydrous iron oxides as investigated by chemical force microscopy, *Colloids and Surfaces A* 212 (2003), 249-264.
- [117] C. Zhang, B. Wangler, B. Morgenstern, H. Zentgraf, M. Eisenhut, H. Untenecker, R. Kruger, R. Huss, C. Seliger, W. Semmler and F. Kiessling, Silica- and alkoxyisilane-coated ultrasmall superparamagnetic iron oxide particles: A promising tool to label cells for magnetic resonance imaging, *Langmuir* 23 (2007), 1427-1434.
- [118] P. Tartaj, T. Gonzalez-Carreno and C. J. Serna, Synthesis of nanomagnets dispersed in colloidal silica cages with applications in chemical separation, *Langmuir* 18 (2002), 4556-4558.
- [119] J. Lin, W. Zhou, A. Kumbhar, J. Wiemann, J. Fang, E. E. Carpenter and C. J. O'Connor, Gold-coated Iron (Fe@Au) nanoparticles: synthesis, characterization, and magnetic field-induced self-assembly, *Journal of Solid State Chemistry* 159 (2001), 26-31.
- [120] M. Chen, S. Yamamuro, D. Farrell and S. Majetich, Gold-coated magnetic nanoparticles for biomedical applications, *Journal of Applied Physics*, 93 (2003), 7551-7553.
-

- 
- [121] A. M. Morawski, P. M. Winter, K. C. Crowder, S. D. Caruthers, R. W. Fuhrlop, M. J. Scott, J. D. Robertson, D. R. Abendschein, G. M. Lanza and S. A. Wickline, Targeted nanoparticles for quantitative imaging of sparse molecular epitopes with MRI, *Magnetic Resonance in Medicine* 51 (2004), 480-486.
- [122] A. E. Lesnikovich, T. M. Shunkevich, V. N. Naumenko, S. A. Vorobyova and M. W. Baykov, Dispersity of magnetite in magnetic liquids and the interaction with a surfactant, *Journal of Magnetism and Magnetic Materials* 85 (1990), 14-16.
- [123] Y. Sun, L. Duan, Z. Guo, Y. DuanMu, M. Ma, L. Xu, Y. Zhang and N. Gu, An improved way to prepare superparamagnetic magnetite-silica core-shell nanoparticles for possible biological application, *Journal of Magnetism and Magnetic Materials* 285 (2005), 65-70.
- [124] W. K. Johnson, C. Stoupis, G. M. Torres, E. B. Rosenberg and R. R. Ros, Superparamagnetic iron oxide (SPIO) as an oral contrast agent in gastrointestinal (GI) magnetic resonance imaging (MRI): Comparison with state-of-the-art computed tomography (CT), *Magnetic Resonance Imaging* 14 (1996), 43-49.
- [125] S. H. Im, T. Herricks, Y. T. Lee and Y. Xia, Synthesis and characterization of monodisperse silica colloids loaded with superparamagnetic iron oxide nanoparticles, *Chemical Physics Letters* 40 (2005), 19-23.
- [126] M. D. Butterworth, S. A. Bell, S. P. Armes and A. W. Simpson, Synthesis and characterization of polypyrrole– magnetite–silica particles, *Journal of Colloid and Interface Science* 183 (1996), 91-99.
- [127] H. H. Yang, S. Q. Zhang, X. L. Chen, Z. X. Zhuang, J. G. Xu and X. R. Wang, Magnetite-containing spherical silica nanoparticles for biocatalysis and bioseparations, *Analytical Chemistry* 76 (2004), 1316-1321.
-

- 
- [128] S. Mornet, J. Portier and E. Duguet, A method for synthesis and functionalization of ultrasmall superparamagnetic covalent carriers based on maghemite and dextran, *Journal of Magnetism and Magnetic Materials* 293 (2005), 127-134.
- [129] M. Hu, J. Chen, Z. Y. Li, L. Au, G. V. Hartland, X. Li, M. Marquez and Y. Xia, Gold nanostructures: engineering their plasmonic properties for biomedical applications, *Chemical Society Reviews* 35 (2006), 1084-1094.
- [130] J. L. Lyon, D. A. Fleming, B. Stone, P. Schiffer and M. E. Williams, Synthesis of Fe oxide core/Au shell nanoparticles by iterative hydroxylamine seeding, *Nano Letters* 4 (2004), 719.
- [131] J. Kim, S. Park, J. E. Lee, S. M. Jin, J. H. Lee, I. S. Lee, I. Yang, J. S. Kim, S. K. Kim, M. H. Cho and T. Hyeon, Designed fabrication of multifunctional magnetic gold nanoshells and their application to magnetic resonance imaging and photothermal therapy, *Angewandte Chemie International Edition* 45 (2006), 7754-7758.
- [132] S. Susmel, C. K. O'Sullivan and G. G. Guilbault, Human cytomegalovirus detection by a quartz crystal microbalance immunosensor *Enzyme and Microbial Technology* 27 (2000), 639-645.
- [133] M. Michael Alexander and L. W. Kenneth, Investigations into the physicochemical properties of dextran small particulate gadolinium oxide nanoparticles, *Academic Radiology* 13 (2006), 421-427.
- [134] J. M. de la Fuente and S. Penades, Glyconanoparticles: Types, synthesis and applications in glycoscience, biomedicine and material science, *Biochimica et Biophysica Acta (BBA)* 1760 (2006), 636-651.
- [135] A. Ito, K. Ino, T. Kobayashi and H. Honda, The effect of RGD peptide-conjugated magnetite cationic liposomes on cell growth and cell sheet harvesting, *Biomaterials* 26 (2005), 6185-6193.
-

- 
- [136] N. Nitin, L. E. W. LaConte, O. Zurkiya, X. Hu and G. Bao, Functionalization and peptide-based delivery of magnetic nanoparticles as an intracellular MRI contrast agent, *Journal of Biological Inorganic Chemistry* 9 (2004), 706-712.
- [137] C. C. Berry, S. Wells, S. Charles and A. S. G. Curtis, Dextran and albumin derivatised iron oxide nanoparticles: influence on fibroblasts in vitro, *Biomaterials* 24 (2003), 4551-4557.
- [138] L. F. Gamarra, G. E. S. Brito, W. M. Pontuschka, E. Amaro, A. H. C. Parma and G. F. Goya, Biocompatible superparamagnetic iron oxide nanoparticles used for contrast agents: a structural and magnetic study, *Journal of Magnetism and Magnetic Materials* 289 (2005), 439-441.
- [139] R. S. Molday and D. MacKenzie, Immunospecific ferromagnetic iron-dextran reagents for the labeling and magnetic separation of cells, *Journal of Immunological Methods* 52 (1982), 353-367.
- [140] P. Tartaj, M. P. Morales, S. Veintemillas-Verdaguer, T. Gonzalez-Carreno and C. J. Serna, *Handbook of Magnetic Materials*, (2006) Elsevier, Buschow.
- [141] M. C. Bautista, O. Bomati-Miguel, M. P. Morales, C. J. Serna and S. Veintemillas-Verdaguer, Surface characterisation of dextran-coated iron oxide nanoparticles prepared by laser pyrolysis and coprecipitation, *Journal of Magnetism and Magnetic Materials* 293 (2005), 20-27.
- [142] D. K. Kim, Y. Zhang, J. Kehr, T. Klason, B. Bjelke and M. Muhammed, Characterization and MRI study of surfactant-coated superparamagnetic nanoparticles administered into the rat brain, *Journal of Magnetism and Magnetic Materials* 225 (2001), 256-261.
-

- 
- [143] M. D. Shultz, S. Calvin, P. P. Fatouros, S. A. Morrison and E. E. Carpenter, Enhanced ferrite nanoparticles as MRI contrast agents, *Journal of Magnetism and Magnetic Materials* 311 (2007), 464-468.
- [144] N. Kohler, G. E. Fryxell and M. Zhang, A bifunctional poly(ethylene glycol) silane immobilized on metallic oxide-based nanoparticles for conjugation with cell targeting agents, *Journal of the American Chemical Society* 126 (2004), 7206-7211.
- [145] S. M. Moghimi, A. C. H. Hunter and J. C. Murray, Long-circulating and target-specific nanoparticles: theory to practice, *Pharmacological Reviews* 53 (2001), 283-318.
- [146] H. Ya ci Acar, R. S. Garaas, F. Syud, P. Bonitatebus and A. M. Kulkarni, Superparamagnetic nanoparticles stabilized by polymerized PEGylated coatings, *Journal of Magnetism and Magnetic Materials* 293 (2005), 1-7.
- [147] M. Kumagai, Y. Imai, T. Nakamura, Y. Yamasaki, M. Sekino, S. Ueno, K. Hanaoka, K. Kikuchi, T. Nagano, E. Kaneko, K. Shimokado and K. Kataoka, Iron hydroxide nanoparticles coated with poly(ethylene glycol)-poly(aspartic acid) block copolymer as novel magnetic resonance contrast agents for in vivo cancer imaging, *Colloids and Surfaces B: Biointerfaces* 56 (2007), 174-181.
- [148] M. Sairam, B. V. K. Naidu, S. K. Nataraj, B. Sreedhar and T. M. Aminabhavi, Poly(vinyl alcohol)-iron oxide nanocomposite membranes for pervaporation dehydration of isopropanol, 1,4-dioxane and tetrahydrofuran, *Journal of Membrane Science* 283 (2006), 65-73.
- [149] B. Schopf, T. Neuberger, K. Schulze, A. Petri, M. Chastellain, M. Hofmann, H. Hofmann and B. von Rechenberg, Methodology description for detection of cellular uptake of PVA coated superparamagnetic iron oxide nanoparticles (SPION) in synovial cells of sheep, *Journal of Magnetism and Magnetic Materials* 293 (2005), 411-418.
-

- [150] J. Lee, T. Isobe and M. Senna, Preparation of ultrafine  $\text{Fe}_3\text{O}_4$  particles by precipitation in the presence of PVA at high pH, *Journal of Colloid and Interface Science* 177 (1996), 490-494.
- [151] M. Chastellain, A. Petri and H. Hofmann, Particle size investigations of a multistep synthesis of PVA coated superparamagnetic nanoparticles, *Journal of Colloid and Interface Science* 278 (2004), 353-360.
- [152] Y. Osada and J. Gong, Soft and wet materials: Polymer gels, *Advanced Materials* 10 (1998), 827-837.
- [153] Y. Nishio, A. Yamada, K. Ezaki, Y. Miyashita, H. Furukawa and K. Horie, Preparation and magnetometric characterization of iron oxide-containing alginate/poly(vinyl alcohol) networks, *Polymer* 45 (2004), 7129-7136.
- [154] F. Llanes, D. H. Ryan and R. H. Marchessault, Magnetic nanostructured composites using alginates of different M/G ratios as polymeric matrix, *International Journal of Biological Macromolecules* 27 (2000), 35-40.
- [155] P. V. Finotelli, M. A. Morales, M. H. Rocha-Leao, E. M. Baggio-Saitovitch and A. M. Rossi, Magnetic studies of iron(III) nanoparticles in alginate polymer for drug delivery applications, *Materials Science and Engineering* 24 (2004), 625-629.
- [156] M. A. Morales, P. V. Finotelli, J. A. H. Coaquira, M. H. M. Rocha-Leao, C. Diaz-Aguila, E. M. Baggio-Saitovitch and A. M. Rossi, In situ synthesis and magnetic studies of iron oxide nanoparticles in calcium-alginate matrix for biomedical applications, *Materials Science and Engineering: C* 28 (2008), 253-257.
- [157] Z. Jia, W. Yujun, L. Yangcheng, M. Jingyu and L. Guangsheng, In situ preparation of magnetic chitosan/ $\text{Fe}_3\text{O}_4$  composite nanoparticles in tiny pools of water-in-oil microemulsion, *Reactive and Functional Polymers* 66 (2006), 1552-1558.

- 
- [158] S. R. Bhattarai, K. C. Bahadur, S. Aryal, M. S. Khill and H. Y. Kim, N-Acylated chitosan stabilized iron oxide nanoparticles as a novel nano-matrix and ceramic modification, *Carbohydrate Polymers* 69 (2007), 467-477.
- [159] E. H. Kim, H. S. Lee, B. K. Kwak and B. K. Kim, Synthesis of ferrofluid with magnetic nanoparticles by sonochemical method for MRI contrast agent, *Journal of Magnetism and Magnetic Materials* 289 (2005), 328-330.
- [160] H. S. Lee, E. H. Kim, H. Shao and B. K. Kwak, Synthesis of SPIO-chitosan microspheres for MRI-detectable embolotherapy, *Journal of Magnetism and Magnetic Materials* 293 (2005), 102-105.
- [161] M. Mikhaylova, Y. S. Jo and D. K. Kim, The effect of biocompatible coating layers on magnetic properties of superparamagnetic iron oxide nanoparticles, *Hyperfine interactions* 156 (2004), 257-263.
- [162] G. D. Mendenhall, Y. Geng and J. Hwang, Optimization of Long-Term Stability of Magnetic Fluids from Magnetite and Synthetic Polyelectrolytes, *Journal of Colloid and Interface Science* 184 (1996), 519-526.
- [163] H. L. Liu, S. P. Ko, J. H. Wu, M. H. Jung, J. H. Min, J. H. Lee, B. H. An and Y. K. Kim, One-pot polyol synthesis of monosize PVP-coated 5 nm  $\text{Fe}_3\text{O}_4$  nanoparticles for biomedical applications, *Journal of Magnetism and Magnetic Materials* 310 (2007), e815-e817.
- [164] M. Iijima, Y. Yonemochi, M. Tsukada and H. Kamiya, Microstructure control of iron hydroxide nanoparticles using surfactants with different molecular structures, *Journal of Colloid and Interface Science* 298 (2006), 202-208.
- [165] T. Sugimoto, *Fine Particles: Synthesis, Characterisation and Mechanism of Growth*, (2000), Marcel Dekker, New York.
-

- 
- [166] V. K. LaMer and R. H. Dinegar, Theory, production and mechanism of formation of monodispersed hydrosols, *Journal of American Chemical Society* 72 (1950), 4847-4854.
- [167] C. J. Den Ouden and R. W. Thompson, Analysis of the formation of monodisperse populations by homogeneous nucleation, *Journal of Colloid and Interface Science* 143 (1991), 77-84.
- [168] M. Ocana, R. Rodriguez-Clemente and C. J. Serna, Uniform colloidal particles in solution: Formation mechanisms, *Advanced Materials* 7 (1995), 212-216.
- [169] D. Farrell, S. Majetich and J. P. Wilcoxon, Preparation and characterization of monodisperse Fe nanoparticles, *Journal of Physical Chemistry B*, 107 (2003), 11022-11030.
- [170] H. Shang, W. S. Chang, S. Kan, S. A. Majetich and G. U. Lee, Synthesis and characterization of paramagnetic microparticles through emulsion-templated free radical polymerization, *Langmuir*, 22 (2006), 2516-2522.
- [171] P. Tartaj, M. P. Morales, S. Veintemillas-Verdaguer, T. Gonzalez-Carreno and C. Serna, The preparation of magnetic nanoparticles for applications in biomedicine, *Journal of Physics D: Applied Physics* 36 (2003), R182–197.
- [172] R. Massart and V. Cabuil, Effect of some parameters on the formation of colloidal magnetite in alkaline medium: yield and particle size control, *Journal of Chemical Physics* 84 (1987), 967-973.
- [173] J. P. Jolivet, *Metal Oxide Chemistry and Synthesis: From Solutions to Solid State* (2000), Wiley-VCH, Weinheim.
- [174] R. Hergt, R. Hiergeist, I. Hilger, W. A. Kaiser, Y. Lapatnikov, S. Margel and U. Richter, Maghemite nanoparticles with very high AC-losses for application in RF-
-

- 
- magnetic hyperthermia, *Journal of Magnetism and Magnetic Materials* 270 (2004), 345-357.
- [175] D. Myers, *Surfactant Science and Technology*, (2005) John Wiley and Sons Inc., Chichester.
- [176] M. P. Pileni, Reverse micelles as microreactors, *The Journal of Physical Chemistry* 97 (1993), 6961-6973.
- [177] I. Lisiecki and M. P. Pileni, Synthesis of copper metallic clusters using reverse micelles as microreactors, *Journal of the American Chemical Society* 115 (1993), 3887-3896.
- [178] K. Zhang, C. H. Chew, G. Q. Xu, J. Wang and L. M. Gan, Synthesis and characterization of silica-copper oxide composite derived from microemulsion processing, *Langmuir* 15 (1999), 3056-3061.
- [179] A. J. Zarur and J. Y. Ying, Reverse microemulsion synthesis of nanostructured complex oxides for catalytic combustion, *Nature* 403 (2000), 65-67.
- [180] P. Tartaj and DeJonghe, Preparation of nanospherical amorphous zircon powders by a microemulsion-mediated process, *Journal of Materials Chemistry* 10 (2000), 2786-2790.
- [181] P. Tartaj and C. J. Serna, Microemulsion-assisted synthesis of tunable superparamagnetic composites, *Chemistry of Materials* 14 (2002), 4396-4402.
- [182] M. P. Pileni, The role of soft colloidal templates in controlling the size and shape of inorganic nanocrystals, *Nature Materials* 2 (2003), 145-150.
- [183] N. Feltin and M. P. Pileni, New technique for synthesizing iron ferrite magnetic nanosized particles, *Langmuir* 13 (1997), 3927-3933.
-

- 
- [184] M. A. Lopez-Quintela and J. Rivas, Chemical reactions in microemulsions: A powerful method to obtain ultrafine particles, *Journal of Colloid and Interface Science* 158 (1993), 446-451.
- [185] E. E. Carpenter, Iron nanoparticles as potential magnetic carriers, *Journal of Magnetism and Magnetic Materials* 225 (2001), 17-20.
- [186] G. Viau, F. Ravel, O. Acher, F. Fievet-Vincent and F. Fievet, Preparation and microwave characterization of spherical and monodisperse  $\text{Co}_{20}\text{Ni}_{80}$  particles, *The 6th Joint Magnetism and Magnetic Materials (MMM)-Intermag Conference*, (1994), New Mexico, USA.
- [187] F. Fievet, J. P. Lagier, B. Blin, B. Beaudoin and M. Figlarz, Homogeneous and heterogeneous nucleations in the polyol process for the preparation of micron and submicron size metal particles, *Solid State Ionics* 32-33 (1989), 198-205.
- [188] G. Viau, F. Fievet-Vincent and F. Fievet, Nucleation and growth of bimetallic CoNi and FeNi monodisperse particles prepared in polyols, *Solid State Ionics* 84 (1996), 259-270.
- [189] G. Viau, F. Fievet-Vincent and F. Fievet, Monodisperse iron-based particles: precipitation in liquid polyols, *Journal of Materials Chemistry* 6 (1996), 1047-1053.
- [190] J. Rockenberger, E. C. Scher and A. P. Alivisatos, A new nonhydrolytic single-precursor approach to surfactant-capped nanocrystals of transition metal oxides, *Journal of the American Chemical Society* 121 (1999), 11595-11596.
- [191] T. Hyeon, S. S. Lee, J. Park, Y. Chung and H. B. Na, Synthesis of highly crystalline and monodisperse maghemite nanocrystallites without a size-selection process, *Journal of the American Chemical Society* 123 (2001), 12798-12801.
- [192] S. Sun and H. Zeng, Size-controlled synthesis of magnetite nanoparticles, *Journal of the American Chemical Society* 124 (2002), 8204-8205.
-

- 
- [193] N. D. Chasteen and P. M. Harrison, Mineralization in ferritin: An efficient means of iron storage, *Journal of Structural Biology* 126 (1999), 182-194.
- [194] K. K. W. Wong, T. Douglas, S. Gider, D. D. Awschalom and S. Mann, Biomimetic synthesis and characterization of magnetic proteins (magnetoferritin), *Chemistry of Materials* 10 (1998), 279-285.
- [195] E. Strable, J. W. M. Bulte, B. Moskowitz, K. Vivekanandan, M. Allen and T. Douglas, Synthesis and characterization of soluble iron oxide-dendrimer composites, *Chemistry of Materials* 13 (2001), 2201-2209.
- [196] X. Cao, R. Prozorov, Y. Koltypin, G. Kataby, I. Felner and A. Gedanken, Synthesis of pure amorphous  $\text{Fe}_2\text{O}_3$  *Journal of Materials Research* 12 (1997), 402-406
- [197] K. V. P. M. Shafi, A. Ulman, A. Dyal, X. Yan, N. L. Yang, C. Estournes, L. Fournes, A. Wattiaux, H. White and M. Rafailovich, Magnetic enhancement of gamma -  $\text{Fe}_2\text{O}_3$  nanoparticles by sonochemical coating, *Chemistry of Materials* 14 (2002), 1778-1787.
- [198] K. V. P. M. Shafi, A. Ulman, A. Dyal, X. Yan, N. L. Yang, C. Estournes, L. Fournes, A. Wattiaux, H. White and M. Rafailovich, Sonochemical synthesis of functionalized amorphous iron oxide nanoparticles, *Langmuir* 17 (2001), 5093-5097.
- [199] C. Pascal, J. L. Pascal, F. Favier, M. L. Elidrissi Moubtassim and C. Payen, Electrochemical synthesis for the control of gamma  $\text{Fe}_2\text{O}_3$  nanoparticle size: Morphology, microstructure, and magnetic behavior, *Chemistry of Materials* 11 (1999), 141-147.
- [200] G. L. Messing, S. C. Zhang and G. V. Jayanthi, Ceramic powder synthesis by spray pyrolysis, *Journal of the American Ceramic Society* 76 (1993), 2707-2726.
-

- 
- [201] P. Carlos, T. Gonzalez-Carreno and E. I. Juan, The infrared dielectric properties of maghemite,  $\gamma\text{-Fe}_2\text{O}_3$ , from reflectance measurement on pressed powders, *Physics and Chemistry of Minerals* V22 (1995), 21-29.
- [202] S. Veintemillas-Verdaguer, M. P. Morales and C. J. Serna, Continuous production of gamma  $\text{Fe}_2\text{O}_3$  ultrafine powders by laser pyrolysis, *Materials Letters* 35 (1998), 227-231.
- [203] R. F. Ziolo, E. P. Giannelis, B. A. Weinstein, M. P. O'Horo, B. N. Ganguly, V. Mehrotra, M. W. Russell and D. R. Huffman, Matrix-mediated synthesis of nanocrystalline gamma  $\text{Fe}_2\text{O}_3$ : A new optically transparent magnetic material, *Science* 257 (1992), 219-223.
- [204] E. Bourgeat-Lami and J. Lang, Encapsulation of inorganic particles by dispersion polymerization in polar media: Silica nanoparticles encapsulated by polystyrene, *Journal of Colloid and Interface Science* 197 (1998), 293-308.
- [205] V. S. Zaitsev, D. S. Filimonov, I. A. Presnyakov, R. J. Gambino and B. Chu, Physical and chemical properties of magnetite and magnetite-polymer nanoparticles and their colloidal dispersions, *Journal of Colloid and Interface Science* 212 (1999), 49-57.
- [206] P. K. Gupta, C. T. Hung, F. C. Lam and D. G. Perrier, Albumin microspheres. III. Synthesis and characterization of microspheres containing adriamycin and magnetite, *International Journal of Pharmaceutics* 43 (1988), 167-177.
- [207] H. Emad Eldin, C. P. Roy and M. G. James, Optimized formulation of magnetic chitosan microspheres containing the anticancer agent, oxantrazole, *Pharmaceutical Research* V9 (1992), 390-397.
- [208] D. Muller-Schulte and H. Brunner, Novel magnetic microspheres on the basis of poly(vinyl alcohol) as affinity medium for quantitative detection of glycated haemoglobin, *Journal of Chromatography A* 711 (1995), 53-60.
-

- 
- [209] K. Wormuth, Superparamagnetic latex via inverse emulsion polymerization, *Journal of Colloid and Interface Science* 241 (2001), 366-377.
- [210] P. A. Dresco, V. S. Zaitsev, R. J. Gambino and B. Chu, Preparation and properties of magnetite and polymer magnetite nanoparticles, *Langmuir* 15 (1999), 1945-1951.
- [211] F. del Monte, M. P. Morales, D. Levy, A. Fernandez, M. Ocana, A. Roig, E. Molins, K. O'Grady and C. J. Serna, Formation of gamma-Fe<sub>2</sub>O<sub>3</sub> isolated nanoparticles in a silica matrix, *Langmuir* 13 (1997), 3627-3634.
- [212] G. Ennas, A. Musinu, G. Piccaluga, D. Zedda, D. Gatteschi, C. Sangregorio, J. L. Stanger, G. Concas and G. Spano, Characterization of iron oxide nanoparticles in an Fe<sub>2</sub>O<sub>3</sub>-SiO<sub>2</sub> composite prepared by a sol-gel method, *Chemistry of Materials* 10 (1998), 495-502.
- [213] A. Ulman, Formation and structure of self-assembled monolayers, *Chemical Reviews* 96 (1996), 1533-1554.
- [214] P. Mulvaney, L. M. Liz-Marzán, M. Giersig and T. Ung, Silica encapsulation of quantum dots and metal clusters, *Journal of Materials Chemistry* 10 (2000), 1259 - 1270.
- [215] P. Tartaj, T. Gonzalez-Carreño and C. J. Serna, Single-step nanoengineering of silica coated maghemite hollow spheres with tunable magnetic properties, *Advanced Materials* 13 (2001), 1620-1624.
- [216] S. Santra, R. Tapeç, N. Theodoropoulou, J. Dobson, A. Hebard and W. Tan, Synthesis and characterization of silica-coated iron oxide nanoparticles in microemulsion: The effect of nonionic surfactants, *Langmuir* 17 (2001), 2900-2906.
- [217] R. K. Visaria, R. J. Griffin, B. W. Williams, E. S. Ebbini, G. F. Paciotti, C. W. Song and J. C. Bischof, Enhancement of tumor thermal therapy using gold nanoparticle-
-

- 
- assisted tumor necrosis factor-alpha delivery, *Molecular Cancer Therapeutics* 5 (2006), 1014-1020.
- [218] D. P. O'Neal, L. R. Hirsch, N. J. Halas, J. D. Payne and J. L. West, Photo-thermal tumor ablation in mice using near infrared-absorbing nanoparticles, *Cancer Letters* 209 (2004), 171-176.
- [219] T. B. Huff, L. Tong, Y. Zhao, M. N. Hansen, J. X. Cheng and A. Wei, Hyperthermic effects of gold nanorods on tumor cells, *Nanomedicine* 2 (2007), 125-132.
- [220] M. Mahmoudi, A. Simchi, M. Imani, A. S. Milani and P. Stroeve, Optimal design and characterization of superparamagnetic iron oxide nanoparticles coated with polyvinyl alcohol for targeted delivery and imaging, *The Journal of Physical Chemistry B* 112 (2008), 14470-14481.
- [221] A. A. Kuznetsov, V. I. Filippov, O. A. Kuznetsov, V. G. Gerlivanov, E. K. Dobrinsky and S. I. Malashin, New ferro-carbon adsorbents for magnetically guided transport of anti-cancer drugs, *Journal of Magnetism and Magnetic Materials* 194 (1999), 22-30.
- [222] M. Arruebo, R. Fernández-Pacheco, S. Irusta, J. Arbiol, M. R. Ibarra and J. Santamaría, Sustained release of doxorubicin from zeolite–magnetite nanocomposites prepared by mechanical activation *Nanotechnology* 17 (2006), 4057-4064.
- [223] G. K. Batchelor, *An Introduction to Fluid Dynamics*, (1970) Cambridge University Press, U.K.
- [224] E. P. Furlani, *Permanent Magnet and Electromechanical Device: Materials, Analysis and Applications*, (2001) Academic Press, New York.
- [225] A. R. Pries, T. W. Secomb and P. Gaehtgens, Biophysical aspects of blood flow in the microvasculature, *Cardiovascular Research* 32 (1996), 654-667.
-

- 
- [226] S. J. Cho, S. M. Kauzlarich, J. Olamit, K. Liu, F. Grandjean, L. Rebbouh and G. J. Long, Characterization and magnetic properties of core/shell structured Fe/Au nanoparticles, *Journal of Applied Physics* 95 (2004), 6804-6806.
- [227] V. Crist, *Handbook of Monochromatic XPS Spectra*, (2004) XPS International LLC, Mountain View.
- [228] I. Y. Goon, L. M. H. Lai, M. Lim, P. Munroe, J. J. Gooding and R. Amal, Fabrication and dispersion of gold-shell protected magnetite nanoparticles: Systematic control using polyethyleneimine, *Chemistry of Materials* 21 (2009), 673-681.
- [229] S. J. Cho, J. C. Idrobo, J. Olamit, K. Liu, N. D. Browning and S. M. Kauzlarich, Growth mechanisms and oxidation resistance of Gold-coated Iron nanoparticles, *Chemistry of Materials* 17 (2005), 3181-3186.
- [230] C. T. Seip and C. J. O'Connor, The fabrication and organization of self-assembled metallic nanoparticles formed in reverse micelles, *Nanostructured Materials* 12 (1999), 183-186.
- [231] B. D. Cullity, *Introduction to Magnetic Materials*, (1972) Addition Wesley, Reading.
- [232] J. Zhang, M. Post, T. Veres, Z. J. Jakubek, J. Guan, D. Wang, F. Normandin, Y. Deslandes and B. Simard, Laser-assisted synthesis of superparamagnetic Fe@Au core-shell nanoparticles, *The Journal of Physical Chemistry B* 110 (2006), 7122-7128.
- [233] Y. P. Bao, H. Calderon and K. M. Krishnan, Synthesis and characterization of magnetic-optical Co-Au core-shell nanoparticles, *Journal of Physical Chemistry C* 111 (2007), 1941-1944.
- [234] S. Pal, M. Morales, P. Mukherjee and H. Srikanth, Synthesis and magnetic properties of gold coated iron oxide nanoparticles, *Journal of Applied Physics* 105 (2009), 07B504.
-

- [235] J. Lim, A. Eggeman, F. Lanni, R. D. Tilton and S. A. Majetich, Synthesis and single-particle optical detection of low-polydispersity plasmonic-superparamagnetic nanoparticles, *Advanced Materials* 20 (2008), 1721-1726.
- [236] I. C. Chiang and D. H. Chen, Synthesis of monodisperse Fe-Au nanoparticles with tunable magnetic and optical properties, *Advanced Functional Materials* 17 (2007), 1311-1316.
- [237] Y. H. Wei, R. Klajn, A. O. Pinchuk and B. A. Grzybowski, Synthesis, shape control, and optical properties of hybrid Au/Fe<sub>3</sub>O<sub>4</sub> "nanoflowers", *Small* 4 (2008), 1635-1639.
- [238] E. E. Carpenter, Iron nanoparticles as potential magnetic carriers, *Journal of Magnetism and Magnetic Materials* 225 (2001), 17-20.
- [239] Q. Sun, A. K. Kandalam, Q. Wang, P. Jena, Y. Kawazoe and M. Marquez, Effect of Au coating on the magnetic and structural properties of Fe nanoclusters for use in biomedical applications: A density-functional theory study, *Physical Review B (Condensed Matter and Materials Physics)* 73 (2006), 134409-134406.
- [240] A. Gole, J. W. Stone, W. R. Gemmill, H. C. zur Loye and C. J. Murphy, Iron oxide coated gold nanorods: Synthesis, characterization and magnetic manipulation, *Langmuir* 24 (2008), 6232-6237.
- [241] I. C. Chiang and D. H. Chen, Structural characterization and self-assembly into superlattices of iron oxide-gold core-shell nanoparticles synthesized via a high-temperature organometallic route, *Nanotechnology* 20 (2009), 015602.
- [242] M. C. Daniel and D. Astruc, Gold nanoparticles: Assembly, supramolecular chemistry, quantum size related properties, and applications toward biology, catalysis, and nanotechnology, *Chemical Reviews* 104 (2004), 293-346.

- 
- [243] Y. Xia, B. Gates, Y. Yin and Y. Lu, Monodispersed colloidal spheres: Old materials with new applications, *Advanced Materials* 12 (2000), 693-713.
- [244] D. S. Grubisha, R. J. Lipert, H. Y. Park, J. Driskell and M. D. Porter, Femtomolar detection of prostate-specific antigen: An immunoassay based on surface-enhanced Raman scattering and immunogold labels, *Analytical Chemistry* 75 (2003), 5936-5943.
- [245] M. Brust, D. J. Schiffrin, D. Bethell and C. J. Kiely, Novel gold-dithiol nano-networks with non-metallic electronic properties, *Advanced Materials* 7 (1995), 795-797.
- [246] H. Y. Park, M. J. Schadt, Wang, I. I. S. Lim, P. N. Njoki, S. H. Kim, M. Y. Jang, J. Luo and C. J. Zhong, Fabrication of magnetic core@shell Fe Oxide@Au nanoparticles for interfacial bioactivity and bio-separation, *Langmuir* 23 (2007), 9050-9056.
- [247] D. Gerion, F. Pinaud, S. C. Williams, W. J. Parak, D. Zanchet, S. Weiss and A. P. Alivisatos, Synthesis and properties of biocompatible water-soluble silica-coated CdSe/ZnS semiconductor quantum dots, *The Journal of Physical Chemistry B* 105 (2001), 8861-8871.
- [248] C. M. Basquin, R. K  gler, N. N. Matsuzawa and A. Yasuda, Gold-nanoparticles-assisted oligonucleotides immobilization for improved DNA detection, *IEEE Proc-Nanobiotechnology* 152 (2005), 97-103.
- [249] M. P. Melancon, W. Lu, Z. Yang, Z. Cheng, R. Zhang, A. M. Elliot, J. Stafford, T. Olson, J. Z. Zhang and C. Li, In vitro and in vivo targeting of hollow gold nanoshells directed at epidermal growth factor receptor for photothermal ablation therapy, *Molecular Cancer Therapeutics* 7 (2008), 1730-1739.
- [250] S. Laurent, D. Forge, M. Port, A. Roch, C. Robic, L. Vander Elst and R. N. Muller, Magnetic iron oxide nanoparticles: Synthesis, stabilization, vectorization, physicochemical characterizations and biological applications, *Chemical Reviews* 108 (2008), 2064-2110.
-

- 
- [251] S. J. Cho, J. C. Idrobo, J. Olamit, K. Liu, N. D. Browning and S. M. Kauzlarich, Growth mechanisms and oxidation resistance of gold-coated iron nanoparticles, *Chemistry of Materials* 17 (2005), 3181-3186.
- [252] O. Pana, C. M. Teodorescu, O. Chauvet, C. Payen, D. Macovei, R. Turcu, M. L. Soran, N. Aldea and L. Barbu, Structure, morphology and magnetic properties of Fe-Au core-shell nanoparticles, *Surface Science* 601 (2007), 4352-4357.
- [253] T. Kinoshita, S. Seino, K. Okitsu, T. Nakayama, T. Nakagawa and T. A. Yamamoto, Magnetic evaluation of nanostructure of gold-iron composite particles synthesized by a reverse micelle method, *Journal of Alloys and Compounds* 359 (2003), 46-50.
- [254] W. Stober, A. Fink and E. Bohn, Controlled growth of monodisperse silica spheres in micron size range, *Journal of Colloid and Interface Science* 26 (1968), 62-63.
- [255] S. I. Stoeva, F. Huo, J. S. Lee and C. A. Mirkin, Three-layer composite magnetic nanoparticle probes for DNA, *Journal of American Chemical Society* 127 (2005), 15362-15363.
- [256] M. Chen, Y. N. Kim, H. M. Lee, C. Li and S. O. Cho, Multifunctional magnetic silver nanoshells with sandwichlike nanostructures, *Journal of Physical Chemistry B* 112 (2008), 8870-8874.
- [257] H. Wang, D. W. Brandl, F. Le, P. Nordlander and N. J. Halas, Nanorice: A hybrid plasmonic nanostructures, *Nano Letters* 6 (2006), 827-832.
- [258] L. Wang, J. Bai, Y. Li and Y. Huang, Multifunctional nanoparticles displaying magnetization and near-IR absorption, *Angewandte Chemie International Edition* 47 (2008), 2439-2442.
-

- 
- [259] I. S. Lim, P. N. Njoki, H. Y. Park, X. Wang, L. Wang, D. Mott and C. J. Zhong, Gold and magnetic oxide/gold core/shell nanoparticles as bio-functional nanoprobe, *Nanotechnology* 19 (2008), 305102(1-11).
- [260] N. S. Kommareddi, M. Tata, V. T. John, G. L. McPherson, M. F. Herman, Y. S. Lee, C. J. O'Connor, J. A. Akkara and D. L. Kaplan, Synthesis of superparamagnetic polymer-ferrite composites using surfactant microstructures, *Chemistry of Materials* 8 (1996), 801-809.
- [261] E. E. Carpenter, C. Sangregorio and C. J. O'Connor, Effects of shell thickness on blocking temperature of nanocomposites of metal particles with gold shells, *IEEE Transactions on Magnetics* 35 (1999), 3496-3498.
- [262] S. J. Cho, B. R. Jarrett, A. Y. Louie and S. M. Kauzlarich, Gold coated iron nanoparticles: A novel magnetic resonance agent for  $T_1$  and  $T_2$  weighted imaging, *Nanotechnology* 17 (2006), 640-644.
- [263] T. Kim and M. Shima, Reduced magnetization in magnetic oxide nanoparticles, *Journal of Applied Physics* 101 (2007), 513-516.
- [264] L. C. Varanda, J. M. Jafelicci, P. Tartaj, K. O. Grady, T. Gonzalez-Carreño, M. P. Morales, T. Munoz and C. J. Serna, Structural and magnetic transformation of monodispersed iron oxide particles in a reducing atmosphere, *Journal of Applied Physics* 92 (2002), 2079-2085.
- [265] S. Rana, A. Gallo, R. S. Srivastava and R. D. K. Misra, The suitability of nanocrystalline ferrites as a magnetic carrier for drug delivery: Functionalization, conjugation and drug release kinetics, *Acta Biomaterialia* 3 (2007), 233-242.
- [266] P. Tartaj, M. P. Morales, T. Gonzalez-Carreño, S. Veintemillas-Verdaguer and C. J. Serna, Advances in magnetic nanoparticles for biotechnology applications, *Journal of Magnetism and Magnetic Materials* 290-291 (2005), 28-34.
-

- 
- [267] V. Salgueirino-Maceira, M. A. Correa-Duarte, M. Farle, A. Lopez-Quintela, K. Sieradzki and R. Diaz, Bifunctional gold-coated magnetic silica spheres, *Chemistry of Materials* 18 (2006), 2701-2706.
- [268] M. P. Melancon, W. Lu, Z. Yang, Z. Cheng, R. Zhang, A. M. Elliot, J. Stafford, T. Olson, J. Z. Zhang and C. Li, *World Molecular Imaging Congress*, (2008), Kyoto, Japan.
- [269] R. M. Cornell and U. Schwertmann, *The Iron Oxides*, (1996), Wiley-VCH, Weinheim.
- [270] L. T. Lee and P. Somasundaran, Adsorption of polyacrylamide on oxide minerals, *Langmuir* 5 (2002), 854-860.
- [271] P. Chibowski and M. Paszkiewicz, Studies of the influence of acetate groups from polyvinyl alcohol on adsorption and electrochemical properties of the  $\text{TiO}_2$  - polymer solution interface, *Journal of Dispersion Science and Technology* 22 (2001), 281-289.
- [272] M. A. Cohen Stuart, J. M. H. M. Scheutjens and G. J. Fleer, Polidispersity effects and the interpretation of polymer adsorption isotherms, *Journal of Polymer Science. Part A-2, Polymer Physics* 18 (1980), 559-573.
- [273] T. F. Tadros, The interaction of cetyltrimethylammonium bromide and sodium dodecylbenzene sulfonate with polyvinyl alcohol. adsorption of the polymer-surfactant complexes on silica, *Journal of Colloid and Interface Science* 46 (1974), 528-540.
- [274] A. Lee Smith, *Applied Infrared Spectroscopy*, (1979), John Wiley & Sons, New York.
- [275] J. G. Deng, Y. X. Peng, C. L. He, X. P. Long, P. Li and A. S. C. Chan, Magnetic and conducting  $\text{Fe}_3\text{O}_4$ -polypyrrole nanoparticles with core-shell structure, *Polymer International* 52 (2003), 1182-1187.
-

- 
- [276] J. Deng, X. Ding, W. Zhang, Y. Peng, J. Wang, X. Long, P. Li and A. S. C. Chan, Magnetic and conducting Fe<sub>3</sub>O<sub>4</sub> cross-linked polyaniline nanoparticles with core-shell structure *Polymer* 43 (2002), 2179-2184.
- [277] P. Li, B. Yu and X. Wei, Synthesis and characterization of a high oil-absorbing magnetic composite material, *Journal of Applied Polymer Science* 93 (2004), 894-900.
- [278] H. Zhang, R. Wang, G. Zhang and B. Yang, A covalently attached film based on poly(methacrylic acid)-capped Fe<sub>3</sub>O<sub>4</sub> nanoparticles, *Journal of Applied Polymer Science* 429 (2003), 167-173.
- [279] H. L. Ma and X. R. Qia, Preparation and characterization of superparamagnetic iron oxide nanoparticles stabilized alginate, *International Journal of Pharmacology* 333 (2007), 177-186.
- [280] W. Jiang, H. C. Yang, S. Y. Yang, H. E. Horng, J. C. Hung, Y. C. Chen and C. Y. Hong, Preparation and properties of superparamagnetic nanoparticles with narrow size distribution and biocompatible, *Journal of Magnetism and Magnetic Materials* 283 (2004), 210-214.
- [281] S. A. Gomez-Lopera, R. C. Plaza and A. V. Delgado, Synthesis and characterization of spherical magnetite/biodegradable polymer composite particles, *Journal of Colloid and Interface Science* 240 (2001), 40-47.
- [282] B. Martínez, X. Obradors, L. Balcells, A. Rouanet and C. Monty, Low temperature surface spin-glass transition in gamma-Fe<sub>2</sub>O<sub>3</sub> nanoparticles, *Physical Review Letters* 80 (1998), 181-184.
- [283] K. Yokoyama and D. R. Welchons, The conjugation of amyloid beta protein on the gold colloidal nanoparticles surfaces, *Nanotechnology* 18 (2007), 105101-105107.
-

- 
- [284] M. Aslam, L. Fu, M. Su, K. Vijayamohan and V. P. Dravid, Novel one-step synthesis of amine-stabilized aqueous colloidal gold nanoparticles, *Journal of Materials Chemistry* 14 (2004), 1795-1797.
- [285] H. Ringsdorf, Structure and properties of pharmacologically active polymers, *Journal of Polymer Science* 51 (1975), 135-153.
- [286] J. Siepmann and F. Siepmann, Mathematical modeling of drug delivery, *International Journal of Pharmaceutics* 364 (2008), 328-343.
- [287] D. Sutton, S. Wang, N. Nasongkla, J. Gao and E. E. Dormidontova, Doxorubicin and beta-lapachone release and interaction with micellar core materials: Experiment and modeling, *Experimental Biology and Medicine* 232 (2007), 1090-1099.
- [288] D. S. Fischer, M. T. Knobf, H. Durivage and N. Beaulieu, *The Cancer Chemotherapy Handbook*, (1997), Mosby, St.Louis.
- [289] C. F. Lacy, L. L. Armstrong, M. P. Goldman and L. L. Lance, *Drug Information Handbook*, (2005), Lexi-Comp, Hudson.
- [290] P. E. Watson, I. D. Watson and R. D. Batt, Total body water volumes for adult males and females estimated from simple anthropometric measurements, *American Journal of Clinical Nutrition* 33 (1980), 27-39.
- [291] R. Tong, D. A. Christian, L. Tang, H. Cabral, J. R. Baker, Jr. K. Kataoka, D. E. Discher and J. Cheng, Nanopolymeric therapeutics, *MRS Bulletin* 34 (2009), 422-431.
- [292] R. B. Greenwald, C. D. Conover and Y. H. Choe, Poly(ethylene glycol) conjugated drugs and prodrugs: A comprehensive review, *Critical Reviews in Therapeutic Drug Carrier Systems* 17 (2000), 101-161.
- [293] T. Minko, P. Kopeckova and J. Kopecek, Comparison of the anticancer effect of free and HPMA copolymer-bound adriamycin in human ovarian carcinoma cells, *Pharmaceutical Research* 16 (1999), 986-996.
-

- 
- [294] M. Jelinkova, B. Rihova, T. Etrych, J. Strohalm, K. Ulbrich, K. Kubackova and L. Rozprimova, Antitumor activity of antibody-targeted HPMA copolymers of doxorubicin in experiment and clinical practice, *Clinical Cancer Research* 7 (2001), 3677s–3678s.
- [295] V. R. Calolfa, M. Zamai, A. Ghiglieri, M. Farao, M. vandeVen, E. Gratton, M. G. Castelli, A. Suarato and A. C. Geroni, In vivo biodistribution and antitumor activity of novel HPMAcopolymers of camptothecin, *Clinical Cancer Research* 6 (2000), 4490s–4491s.
- [296] R. Bhatt, P. D. Vries, J. Tulinsky, G. Bellamy, B. Baker, J. W. Singer and P. Klein, Synthesis and in vivo antitumor activity of poly(L-glutamic acid) conjugates of 20(S)-camptothecin, *Journal of Medicinal Chemistry* 46 (2003), 190–193.
- [297] C. Li, D. F. Yu, R. A. Newman, F. Cabral, L. C. Stephens, N. Hunter, L. Milas and S. Wallace, Complete regression of well-established tumors using a novel water-soluble poly(L-glutamic acid)-paclitaxel conjugate, *Cancer Research* 58 (1998), 2404–2409.
- [298] I. Mitsui, E. Kumazawa, Y. Hirota, M. Aonuma, M. Sugimori, S. Ohsuki, K. Uoto, A. Ejima, H. Terasawa and K. Sato, A new water-soluble camptothecin derivative, Dx-8951f, exhibits potent antitumor-activity against human tumors in-vitro and in-vivo, *Japanese Journal of Cancer Research* 86 (1995), 776–782.
- [299] Y. Ochi, Y. Shiose, H. Kuga and E. Kumazawa, A possible mechanism for the long-lasting antitumor effect of the macromolecular conjugate DE-310: mediation by cellular uptake and drug release of its active camptothecin analog DX-8951, *Cancer Chemotherapy and Pharmacology* 55 (2005), 323–332.
-

- 
- [300] M. Harada, H. Sakakibara, T. Yano, T. Suzuki and S. Okuno, Determinants for the drug release from T-0128, camptothecin analogue-carboxymethyl dextran conjugate, *Journal of Controlled Release* 69 (2000), 399-412.
- [301] R. Haag and F. Kratz, Polymer therapeutics: Concepts and applications, *Angewandte Chemie International Edition* 45 (2006), 1198-1215.
- [302] A. Pendri, C. D. Conover and R. B. Greenwald, Antitumor activity of paclitaxel-20-glycinate conjugated to poly(ethylene glycol): a water-soluble prodrug, *Anti-Cancer Drug Design* 13 (1998), 387-395.
- [303] F. M. Veronese, O. Schiavon, G. Pasut, R. Mendichi, L. Andersson, A. Tsirk, J. Ford, G. F. Wu, S. Kneller, J. Davies and R. Duncan, PEG-doxorubicin conjugates: Influence of polymer structure on drug release, in vitro cytotoxicity, biodistribution, and antitumor activity, *Bioconjugate Chemistry* 16 (2005), 775-784.
- [304] R. B. Greenwald, A. Pendri, C. D. Conover, C. W. Gilbert, R. Yang and J. Xia, Drug delivery systems. 2. Camptothecin 20-O-poly(ethylene glycol) ester transport forms, *Journal of Medicinal Chemistry* 39 (1996), 1938-1940.
- [305] T. Minko, P. V. Paranjpe, B. Qiu, A. Lalloo, R. Won, S. Stein and P. J. Sinko, Enhancing the anticancer efficacy of camptothecin using biotinylated poly(ethylene glycol) conjugates in sensitive and multidrug-resistant human ovarian carcinoma cells, *Cancer Chemotherapy and Pharmacology* 50 (2002), 143-150.
- [306] C. D. Conover, R. B. Greenwald, A. Pendri, C. W. Gilbert and K. L. Shum, Camptothecin delivery systems: Enhanced efficacy and tumor accumulation of camptothecin following its conjugation to polyethylene glycol via a glycine linker, *Cancer Chemotherapy and Pharmacology* 42 (1998), 407-414.
- [307] E. K. Rowinsky, J. Rizzo, L. Ochoa, C. H. Takimoto, B. Forouzes, G. Schwartz, L. A. Hammond, A. Patnaik, J. Kwiatek, A. Goetz, L. Denis, J. McGuire and A. W.
-

- Tolcher, A phase I and pharmacokinetic study of pegylated camptothecin as a 1-hour infusion every 3 weeks in patients with advanced solid malignancies, *Journal of Clinical Oncology* 21 (2003), 148-157.
- [308] L. Seymour, R. Duncan, J. Strohm and J. Kopecek, Effect of molecular weight (MW) of N-(2-hydroxypropyl) methacrylamide copolymers on body distribution and rate of excretion after subcutaneous, intraperitoneal, and intravenous administration to rats, *Journal of Biomedical Materials Research* 21 (1987), 1341-1358.
- [309] J. M. M. Terwogt, W. W. T. Huinink, J. H. M. Schellens, M. Schot, I. A. M. Mandjes, M. G. Zurlo, M. Rocchetti, H. Rosing, F. J. Koopman and J. H. Beijnen, Phase I clinical and pharmacokinetic study of PNU166945, a novel water-soluble polymer-conjugated prodrug of paclitaxel, *Anticancer Drugs* 12 (2001), 315-323.
- [310] D. Bissett, J. Cassidy, J. S. de Bono, F. Muirhead, M. Main, L. Robson, D. Fraier, M. L. Magne, C. Pellizzoni, M. G. Porro, R. Spinelli, W. Speed and C. Twelves, Phase I and pharmacokinetic (PK) study of MAG-CPT (PNU 166148): a polymeric derivative of camptothecin (CPT), *British Journal of Cancer* 91 (2004), 50-55.
- [311] P. A. Vasey, S. B. Kaye, R. Morrison, C. Twelves, P. Wilson, R. Duncan, A. H. Thomson, L. S. Murray, T. E. Hilditch, T. Murray, S. Burtles, D. Fraier, E. Frigerio and J. Cassidy, Phase I clinical and pharmacokinetic study of PK1 [N-(2-hydroxypropyl)methacrylamide copolymer doxorubicin]: first member of a new class of chemotherapeutic agents-drugpolymer conjugates, *Clinical Cancer Research* 5 (1999), 83-94.
- [312] M. Bouma, B. Nuijen, D. R. Stewart, J. R. Rice, B. A. J. Jansen, J. Reedijk, A. Bult and J. H. Beijnen, Stability and compatibility of the investigational polymer-conjugated platinum anticancer agent AP 5280 in infusion systems and its hemolytic potential, *Anticancer Drugs* 13 (2002), 915-924.

- 
- [313] J. W. Singer, S. Shaffer, B. Baker, A. Bernareggi, S. Stromatt, D. Nienstedt and M. Besman, Paclitaxel poliglumex (XYOTAX; CT-2103): an intracellularly targeted taxane, *Anticancer Drugs* 16 (2005), 243-254.
- [314] F. Cavalieri, E. Chiessi, R. Villa, L. Viganò, N. Zaffaroni, M. F. Telling and G. Paradossi, Novel PVA-based hydrogel microparticles for doxorubicin delivery, *Biomacromolecules* 9 (2008), 1967-1973.
- [315] I. Orienti, G. Zuccari, A. Fini, A. M. Rabasco, P. Montaldo, L. Raffaghello and R. Carosio, Modified doxorubicin for improved encapsulation in PVA polymeric micelles, *Drug Delivery* 12 (2005), 15-20.
- [316] L. E. Udrea, N. J. C. Strachan, V. Bădescu and O. Rotariu, An in vitro study of magnetic particle targeting in small blood vessels, *Physics in Medicine and Biology* 51 (2006), 4869-4881.
- [317] M. P. Melancon, W. Lu and C. Li, Gold based magneto/optical nanostructures: challenges for *in vivo* applications in cancer diagnostics and therapy, *MRS Bulletin* 34 (2009), 415-421.
- [318] H.S. Choi, W. Liu, P. Misra, E. Tanaka, J. P. Zimmer, B. I. Ipe, M. G. Bawendi and J. V. Frangioni, Renal clearance of quantum dots, *Nature Biotechnology* 25 (2007), 1165-1170.
- [319] C. Alexiou, W. Arnold, R. J. Klein, F. G. Parak, P. Hulin, C. Bergemann, W. Erhardt, S. Wagenpfeil and A. S. Lübke, Locoregional cancer treatment with magnetic drug targeting, *Cancer Research* 60 (2000), 6641-6648.
- [320] P. Moroz, S. K. Jones and B. N. Gray, Tumor response to arterial embolization hyperthermia and direct injection hyperthermia in a rabbit liver tumor model, *Journal of Surgical Oncology* 80 (2002), 149-156.
-

- 
- [321] P. Moroz, S. K. Jones and B. N. Gray, The effect of tumour size on ferromagnetic embolization hyperthermia in a rabbit liver tumour model, *International Journal of Hyperthermia* 18 (2002), 129-140.
- [322] T. Fujita, M. Nishikawa, Y. Ohtsubo, J. Ohno, Y. Takakura, H. Sezaki and M. Hashida, Control of In Vivo Fate of albumin derivatives utilizing combined chemical modification, *Journal of Drug Targeting* 2 (1994), 157-165.
- [323] M. I. Papisov, A. Bogdanov Jr, B. Schaffer, N. Nossiff, T. Shen, R. Weissleder and T. J. Brady, Colloidal magnetic resonance contrast agents: effect of particle surface on biodistribution, *Journal of Magnetism and Magnetic Materials* 122 (1993), 383-386.
- [324] S. D. Li and L. Huang, Pharmacokinetics and biodistribution of nanoparticles, *Molecular Pharmaceutics* 5 (2008), 496-504.
- [325] H. Maeda, J. Wu, T. Sawa, Y. Matsumura and K. Hori, Tumor vascular permeability and the EPR effect in macromolecular therapeutics: a review, *Journal of Controlled Release* 65 (2000), 271-284.
- [326] G. Kong, R. D. Braun and M. W. Dewhirst, Hyperthermia enables tumor-specific nanoparticle delivery: Effect of particle size, *Cancer Research* 60 (2000), 4440-4445.
- [327] F. Zhang, M. W. Skoda, R. M. Jacobs, S. Zorn, R. A. Martin, C. M. Martin, G. F. Clark, G. Goerigk and F. Schreiber, Gold nanoparticles decorated with oligo(ethylene glycol) thiols: protein resistance and colloidal stability, *The Journal of Physical Chemistry A* 111 (2007), 12229-12237.
- [328] T. Niidome, M. Yamagata, Y. Okamoto, Y. Akiyama, H. Takahashi, T. Kawano, Y. Katayama and Y. Niidome, PEG-modified gold nanorods with a stealth character for in vivo applications, *Journal of Controlled Release* 114 (2006), 343-347.
- [329] H. Otsuka, Y. Nagasaki and K. Kataoka, PEGylated nanoparticles for biological and pharmaceutical applications, *Advanced Drug Delivery Reviews* 55 (2003), 403-419.
-

- 
- [330] X. Qian, X. H. Peng, D. O. Ansari, Q. Yin-Goen, G. Z. Chen, D. M. Shin, L. Yang, A. N. Young, M. D. Wang and S. Nie, In vivo tumor targeting and spectroscopic detection with surface-enhanced Raman nanoparticle tags, *Nature Biotechnology* 26 (2008), 83-90.
- [331] A. Bleetman and J. Dyer, Ultrasound assessment of the vulnerability of the internal organs to stabbing: determining safety standards for stab-resistant body armour, *Injury* 31 (2000), 609-612.
- [332] S. M. Rahman, Personal Communication, (All India Institute of Medical Sciences, Delhi, India, 2010).
- [333] C. Alexiou, D. Diehl, P. Henninger, H. Iro, R. Rockelein, W. Schmidt and H. Weber, A high field gradient magnet for magnetic drug targeting, *IEEE Transactions on Applied Superconductivity* 16 (2006), 1527-1530.
- [334] S. Mohapatra, N. Pramanik, S. K. Ghosh and P. Pramanik, Synthesis and characterisation of ultrafine polyvinyl alcohol phosphate coated magnetic nanoparticles *Journal of Nanoscience and Nanotechnology* 6 (2006), 823-829.
- [335] R. Baker, *Controlled Release of Biologically Active Agents*, (1987), John Wiley & Sons, New York.
- [336] J. M. Vergnaud, *Controlled Drug Release of Oral Dosage Forms*, (1993), Ellis Horwood, New York.
- [337] M. Hombreiro-Perez, J. Siepmann, C. Zinutti, A. Lamprecht, N. Ubrich, M. Hoffman, R. Bodmeier and P. Maincent, Non-degradable microparticles containing a hydrophilic and/or a lipophilic drug: Preparation, characterization and drug release modeling, *Journal of Controlled Release* 88 (2003), 413-428.
-

- 
- [338] S. Herrmann, G. Winter, S. Mohl, F. Siepmann and J. Siepmann, Mechanisms controlling protein release from lipidic implants: Effects of PEG addition, *Journal of Controlled Release* 118 (2007), 161–168.

---

## Appendix-A

### Diffusion controlled drug delivery systems

There are two basic drug delivery systems that are driven by diffusion. In (i) reservoir systems, the drug is contained in a depot, which is surrounded by a release rate controlling barrier membrane (often polymer-based). In (ii) monolithic systems, the drug is uniformly dissolved or dispersed in the polymer and it is released by diffusion from the polymer.

In the case of a reservoir device with non-constant activity source, i.e., the drug concentration at the membrane's surface continuously decreases with time; the drug release follows first order release kinetics [335]:

$$\frac{dM_t}{dt} = \frac{ADKc_t}{l} = \frac{ADK}{l} \frac{M_0 - M_t}{V} \quad \text{A.1}$$

However, in the case of a reservoir device with constant activity source, i.e., the drug concentration at the membrane's surface remains constant; the drug release follows zero order release kinetics [335]:

$$\frac{dM_t}{dt} = \frac{ADKc_s}{l} \quad \text{A.2}$$

where  $M_t$  represents the absolute cumulative amount of drug released at time  $t$ ,  $c_t$  denotes the concentration of the drug at time  $t$ ,  $c_s$  is the solubility of drug in the reservoir,  $M_0$  is the initial amount of drug;  $V$  is the volume of the drug reservoir,  $A$  is the total surface area of the device,  $l$  is the thickness of the membrane,  $K$  is the partition coefficient of the drug between the membrane and the reservoir, and  $D$  is the diffusion coefficient of the drug within the membrane.

In the case of monolithic systems, the system geometry significantly affects the drug release kinetics. In the absence of significant changes in the carrier matrix during drug

release (e.g., constant porosity, no swelling, time-independent permeability for the drug) and if perfect sink conditions are maintained throughout the release period and if the drug release is primarily controlled by diffusion through the carrier matrix, the drug release can be calculated as follows, depending on the geometry of monolithic system:

(i) In the case of spherical dosage forms [286]:

$$\frac{M_t}{M_\infty} = 1 - \frac{6}{\pi^2} \sum_{n=1}^{\infty} \frac{1}{n^2} \exp\left(-\frac{Dn^2\pi^2t}{R_p^2}\right) \quad \text{A.3}$$

and

(ii) In the case of cylinders (considering axial as well as radial mass transport) [336]:

$$\frac{M_t}{M_\infty} = 1 - \frac{32}{\pi^2} \sum_{n=1}^{\infty} \frac{1}{q_n^2} \exp\left(-\frac{q_n^2 Dt}{R^2}\right) \times \sum_{p=0}^{\infty} \frac{1}{(2p+1)^2} \exp\left(-\frac{(2p+1)^2 \pi^2 Dt}{H^2}\right) \quad \text{A.4}$$

where  $M_t$  and  $M_\infty$  are the cumulative amounts of drug released at time  $t$  and infinity, respectively;  $n$  and  $p$  denote dummy variables,  $q_n$  is the roots of the Bessel functions,  $D$  is the diffusion coefficient of the drug,  $R$  and  $H$  denote the radius and height of the cylinder,  $D$  is the diffusion coefficient of the drug and  $R_p$  is the radius of the sphere.

Eqn. A.3 was used to quantify drug release from ammonio methacrylate copolymer-based microparticles [337] and Eqn. A.4 was used to describe the release of the drug from tristearin-based cylinders [338].

In the present work, it is assumed that the drug DOX is uniformly dispersed in PVA and it is released by diffusion from the polymer. The curve fitting of DOX release profiles (Fig. 4.20) with Eqn. A.3 shows that this DOX release follows the Fick's law of diffusion for monolithic systems.

---

## PUBLICATIONS AND CONFERENCES

### Journals:

1. **S. Kayal** and R. V. Ramanujan, "Anti cancer drug loaded iron core / gold shell (Fe@Au) nanoparticles for magnetic drug targeting", *Journal of Nanoscience and Nanotechnology* **10**, (2010) 5527-5539.
2. **S. Kayal** and R. V. Ramanujan, "Doxorubicin loaded superparamagnetic PVA coated iron oxide nanoparticles for targeted drug delivery", *Materials science and Engineering: C* **30**, (2010) 484-490.
3. D. Ang, Q. V. Nguyen, **S. Kayal**, P. R. Preiser, R. S. Rawat and R. V. Ramanujan, "Insights into the mechanism of magnetic particle assisted gene delivery", *Acta Biomaterialia*, **7**, (2011) 1319-1326.
4. **S. Kayal**, D. Bandyopadhyay, T. Mandal and R. V. Ramanujan, "Flow of magnetic nanoparticles in magnetic drug targeting", *accepted in RSC Advances*, (2011).

### Conference Presentations:

1. **S. Kayal** and R. V. Ramanujan, "Magnetic nanoparticle carriers for drug targeting in cancer treatment" Advanced delivery of therapeutics symposium in International Conference on Materials for Advanced Technologies (ICMAT), 2009, Singapore.
2. R. V. Ramanujan, **S. Kayal**, S. Purushotham, "Targeted dual therapy for disease treatment by multifunctional coated magnetic nanoparticles" TMS 2008, 137 annual meeting & exhibition, 2008, New Orleans, Louisiana, USA.
3. **S. Kayal** and R. V. Ramanujan, "PVA coated magnetic nanoparticle carriers for delivery of anticancer drug" International Conference on Cellular and Molecular Bioengineering (ICCMB), 2007, Singapore.
4. R. V. Ramanujan, S. Purushotham and **S. Kayal**, "Multifunctional coated magnetic nanoparticles for disease treatment" Advanced functional biomaterials symposium in International Conference on Materials for Advanced Technologies (ICMAT), 2007, Singapore.
5. R. V. Ramanujan, S. Purushotham and **S. Kayal**, "Multimodal cancer therapy using coated magnetic nanoparticles" TMS 2007, 136 annual meeting & exhibition, 2007, Orlando, Florida, USA.
6. **S. Kayal** and R. V. Ramanujan, "PVA coated iron oxide nanoparticle carriers for magnetic drug targeting" The 5<sup>th</sup> International Conference on Materials Processing for Properties and Performance (MP<sup>3</sup>), 2006, Institute of Materials (East Asia), Singapore.